FINAL REPORT

U.S. DOT
Pipeline and Hazardous
Materials Safety Administration

Competitive Academic
Agreement Program (CAAP)

contract #: DTPH5615HCAP02L

Understanding and Mitigating the Threat of AC Induced Corrosion on Buried Pipelines

Dept. of Chemical. Biomolecular and Corrosion Engineering
University of Akron, Akron Ohio 44325

Technical Information Page

Organization Name:	*Dept. of Chemical, Biomolecular and, Corrosion Engineering* *University of Akron* *Akron Ohio 44325* https://www.uakron.edu/corrosion/
Contact Information:	*PI: R. Scott Lillard, PhD* *Professor and Carboline Endowed Chair in Corrosion* 330-972-7463 lillard@uakron.edu *Co-PIs*: H. Cong (UA), K. Garrity (Mears), D. Wagner (Marathon)
Program Area:	*Threat Prevention*
Title:	*Understanding and Mitigating the Threat of AC Induced Corrosion on Buried Pipelines*
Contract #:	*DTPH5615HCAP02L*
Main Objective:	*Mitigation of AC induced corrosion*
Original Proposal Abstract:	In this project we will explore new methods for assessing the threat of AC corrosion on buried pipelines. The results from this project will improve indirect inspection methods for assessing the impact of induced AC currents on pipeline corrosion rates and could be used for national and international standards. To accomplish this goal the project has three thrust areas: laboratory studies, industrial test facility benchmarking and in-service pipeline validation. Previous work in our lab has shown that the magnitude of interfacial capacitance of the corroding metal is a key parameter in determining AC corrosion rate. As such we will investigate the interfacial capacitance that develops on pipeline steel as a function of corrosion product build-up (scaling) and soil properties such as, resistivity, mineral content and pH. In addition, we will conduct exploratory studies determine the susceptibility of pipeline steel to environmental fracture during exposure to AC. Results from these tests will be benchmarked in experiments conducted in industrial pipeline testing facilities at Mears Integrity and Marathon Petroleum. Finally, we will validate the project by collecting indirect inspection data on an in service pipeline in a transmission line right-of-way owned by Marathon. These data will be used as input to an AC Risk Algorithm to prioritize direct inspection of the pipeline. If permissible, the section of the pipeline identified as being at the greatest risk will be assessed using direct inspection.

TABLE OF CONTENTS

SUMMARY OF ACCOMPLISHMENTS

Degrees Awarded:

1. Elmira Ghanbari, Ph.D., "Corrosion Behavior Of Buried Pipeline In Presence Of AC Stray Current In Controlled Environment," University of Akron, Department of Chemical, Biomolecular and Corrosion Engineering, Sept. 2016.

2. Lizeth J. Sanchez Camacho, MS, "Effect Of AC Interference On The Corrosion Cracking Susceptibility Of Low Carbon Steel Under Cathodic Protection" University of Akron, Department of Chemical, Biomolecular and Corrosion Engineering, anticipated, August, 2018

3. Andrew Moran, "An Assessment Of The Susceptibility To Corrosion From Alternating Current Of Cathodically Protected Steel Pipelines In Soils," University of Akron, Department of Chemical, Biomolecular and Corrosion Engineering, anticipated, Jan. 2020.

Peer Reviewed Papers:

1. E. Ghanbari, R.S. Lillard, "The Influence of $CaCO_3$ Scale Formation on AC Corrosion Rates of Pipeline Steel Under Cathodic Protection," Corrosion, 74 (5), 2018.

2. A.J. Moran, R.S. Lillard, "The Relationship Between Cathodic Protection Levels, AC Current Density, and Corrosion Rate for Pipeline Steel," in preparation.

3. L.S Camacho, H. Cong, "Effect of AC interference on the corrosion and cracking behavior of cathodically protected pipeline steel" (in preparation)

3. A.J. Moran, R.S. Lillard, "The Interrelated Nature of AC and DC at an Electrochemical Interface as they Relate to AC-Affected Pipelines," in preparation.

4. A.J. Moran, R.S. Lillard, "The Effect of Soil Environment on Electrochemical Parameters, Principally Interfacial Capacitance, Which are Predicted to Alter the Risk of AC Corrosion," in preparation

Conference Papers:

1. E. Ghanbari, C. Carpenter, RS Lillard, "The Influence of Scale Formation on the AC Corrosion of API Grade X65 Pipeline Steel under Cathodic Protection" paper # 2017-9809, Corrosion/2017, NACE International, New Orleans, March 2017.

2. A.J. Moran, R.S. Lillard, "AC Corrosion Evaluation of Cathodically Protected Pipeline Steel," *Corrosion,* 75, 144-46, 2019.

3. A.J. Moran, J. Jennings, I. Stallman, K. Platt, K. Garrity, D. Wagner, R.S. Lillard, "Laboratory and Field Testing for the AC Corrosion of Pipeline Steel," Corrosion/2020, NACE International, Houston, March 2020.

Awards:

1. A.J. Moran, 2018 NACE Student Poster Contest, First Place: "AC Corrosion Evaluation of Cathodically Protected Pipeline Steel" Phoenix AZ, 2018.

2. L.J. Sanchez, 2019 NACE Student Poster Contest, Second Place: "AC-Induced Pitting and Pit to Crack Transition Behavior of Low Carbon Steels Under Cathodic Protection". Nashville TN, 2019.

Milestones:

In this work, AC corrosion was investigated through theoretical modeling and experimentation to gain a better understanding of the process as a whole, and as it relates to pipelines under cathodic protection. First, a comprehensive treatment of AC corrosion is given with historical background and motivations for studying this phenomenon, these being, primarily, the utility of accurate AC/corrosion rate relationships to pipeline integrity management. Then, a theoretical model based on Butler-Volmer kinetics and electrochemical interface processes is introduced as a mechanistic explanation of AC corrosion and as a tool to guide investigations. The AC corrosion model can be used to identify the parameters implicated in producing high corrosion rates from alternating currents. This is done to narrow the focus of study to certain measurable factors both in laboratory and in field experiments, specifically, the interfacial capacitance of steel as this parameter is predicted to have a considerable influence on the ratio of faradaic to capacitive current.

How the interfacial capacitance of steel changes as a function of its soil environment is the first exploration in this work. Experiments were conducted with a multitude of synthetic soils and with solutions of varying chemistries of which steel would be expected to encounter in pipeline applications. Measurements of interfacial capacitance were conducted on steel electrodes in these environments through the use of electrochemical impedance spectroscopy and equivalent circuit modeling. Evidence from these investigations indicates that interfacial capacitance on actively corroding steel derives, in large part, from the conductive magnetite corrosion product film. This porous magnetite imparts a uniquely large capacitance to the steel so that most AC is composed of capacitive current rather than faradaic current which would lead to corrosion. Soil minerals and dissolved ions do not influence this property with the exception of scale-developing cations. However, while deposited mineral scales and passive oxide layers can greatly decrease interfacial capacitance, they are unlikely to increase corrosion rates for AC-influenced steel due to their concomitant protective nature.

Long-term mass loss tests were conducted as a first means of assessing the impact of AC corrosion. Literature is either sparse or contradictory about the influence of AC on corrosion rates with some researchers reporting negligible effects and others reporting corrosion rates far in excess of acceptable standards, even at low AC densities. Tests in solution produced modest corrosion rates on cathodically protected samples even at high AC densities. At or below the commonly cited thresholds of AC density (30 A/m2 and 100 A/m2), cathodically protected samples show negligible increased corrosion rates. Greatly increased corrosion rates are observed on non-cathodically protected steel emphasizing the efficacy of and need for proper cathodic protection on pipelines.

Field studies were also conducted as a way to validate the observed trends in laboratory experiments. Samples were bonded to test pipelines and subjected to AC and cathodic protection voltages. Results show greater corrosion rates than laboratory samples at the same AC densities. Corrosion rates are

modest for cathodically protected samples with some samples showing corrosion rates greater than expected for their CP level and others showing full protection from increased corrosion. Data suggest that AC-induced corrosion can present a problem, even on cathodically protected pipelines, at AC densities greater than 100 A/m^2.

We have also used slow strain rate testing (SSRT), and electrochemical hydrogen permeation tests to investigate the cracking susceptibility of low carbon steels (1018 and API X65) under the combination of AC voltages and cathodic protection potentials in a simulated soil solution (NS4). The synergistic effect of cathodic potentials (−0.77, −0.85, and −1.12 V vs. SCE) and AC interference (1, 2, and 3 V rms) was systematically studied. The loss of plasticity and brittle behavior was more evident when more negative cathodic potentials were applied to the samples. The SSRT results demonstrated that the AC interference had a deleterious effect on the ductility and mechanical properties of the low carbon steel, increasing its SCC susceptibility. Corrosion products deposited on the surface were found to increase with an increase in the AC voltage and intensive pitting was observed at lower cathodic potential with AC interference. In addition, scanning electron microscopy (SEM) examination revealed changes in the fracture morphology. Ductile fracture with small dimples was mainly observed at less negative cathodic potential without AC interference, while cleavage planes and microcracks, characteristic of brittle fracture, increased with higher AC voltage and current densities. The brittle fracture presented under the AC interference was associated with anodic dissolution and/or hydrogen embrittlement mechanism. The hydrogen permeation tests were performed in a Devanathan-Stachurski cell, according to the ASTM G148 standard. Hydrogen diffusivity and sub-surface concentration of atomic hydrogen were calculated. Higher sub-surface hydrogen concentration was obtained at lower cathodic potential. The presence of AC voltage further increased the hydrogen permeation current, indicating more hydrogen adsorption on the steel surface and therefore possibly promoting embrittlement.

Due to the limitations of space, in this report we present the results from our field studies on the effects of AC on cathodically protected pipelines and slow strain rate experiments on cracking susceptibility. We refer the reader to our publications listed above for details on the other milestones discussed above.

1. INTRODUCTION

1.1 AC and Buried Pipelines

Unprotected buried pipelines would be subject to failure due to environment interactions such as corrosion. Therefore, pipelines are equipped with corrosion prevention systems, including insulating coatings and cathodic protection (CP). However, these mitigation strategies are reported to have failed in the case of AC corrosion. This type of failure is a threat to the integrity of the pipeline and there is a lack of well-agreed mitigation criteria for it. AC grounding systems as well as "consensus" standards that recommend limits on the maximum allowable AC current density and critical ratios of AC and CP currents are the only available techniques for preventing AC corrosion. Unclear mechanism of AC corrosion is the main reason for the uncertainty on the CP criteria in the presence of AC interference. AC interference can occur by conduction or induction mechanism where pipelines share right of way with some interference sources such as a high-voltage transmission line typically fed by a high voltage line at 50 or 16.7 Hz frequency. The goal of this work is to understand the mechanism of AC induced corrosion by studying the effects of AC interference on steel at different DC potentials.

Cathodic protection (CP), usually combined with insulating coatings is the most effective way for controlling the corrosion of underground or submerged metallic structures including AC corrosion. Utilizing the external potential or current sources (impressed current) and sacrificial anodes are two ways for applying CP and reducing the corrosion rate to a safe level. Although the concept of cathodic protection is based on the experiment by Sir Humphry Davy as early as 1824, it was not until 1983 when Hoar and Mears et al. using Evans diagrams, offered the following description for cathodic protection[1,2,3,4]:

> *… in cases where corrosion is entirely electrochemical in nature it is necessary to polarize the cathodes in the corrosion cell to the open circuit potential of the local anodes in order to obtain complete cathodic protection.*[2]

The recent CP criteria is still based on guidelines that were issued by NACE in 1969 with some modification in 2007 which is the most accepted set of CP standards. The current version of NACE CP standard contains three primary criteria for steel exposed to soil environments:[5]

-850 mVCSE potential criterion with current applied

-850 mVCSE polarized potential

100 mV cathodic polarization criterion[5]

1.2 Pipeline Failures Attributed to AC Corrosion

Increased corrosion rate in the presence of alternating current (AC) has been known to occur for quite some time. About 100 years ago, investigators from the National Institute of Science and Technology described the "Influence of Frequency of Alternating or Infrequently Reversed Current on Electrolytic Corrosion".[6] However, it was not until an accident on a pipeline in Germany in 1986 that it became a widespread industry topic and a safety concern. The mentioned failure occurred on a polyethylene coated pipe installed parallel to a 16.6 Hz powered railway. The pipeline was cathodically protected with instant off-potential of -1V vs. copper-copper sulfate electrode (CSE) using an impressed current system, typical of European industry standards of the time.[7] It was concluded that a low soil resistivity of 1900 ohm.cm from de-icing salts was a contributing factor in the failure. Since then, there have been numerous field cases of AC induced failures in pipelines with otherwise adequate cathodic protection (CP).[8] AC corrosion failures in France with CP On-potentials of -2 and -2.5 V_{CSE} and also five cases of failure in North America due to AC are only a few case histories of AC corrosion failures in CP condition.[9] As a result, international and US standards as well as "best practices" have been published detailing corrosion protection criteria to mitigate AC-induced corrosion on buried pipelines.[10,11,12] In addition to pipelines, the prospect of AC induced corrosion has prompted the oil and gas industry to develop mitigation strategies for its subsea operations.[13,14] In that application, AC is used for autonomous operations as well as to heat pipelines coming from the well to reduce the formation of hydrates and waxes.

To contribute to the development of standards, a large number of field studies along with laboratory experiments have been carried out to characterize the variables that contribute to AC induced corrosion on pipelines, such as: AC potential (or AC current), level of cathodic protection and soil resistivity. [15,16,17,18,19,20]

1.3 Standards Covering AC on Buried Pipelines

The NACE standard, Mitigation of Alternating Current and Lightning Effects on Metallic Structures and Corrosion Control Systems, as well as the NACE CP Interference Manual, describe AC interference as arising from three mechanisms.[21] These are Resistive (or Electrolytic), Capacitive, and Inductive. For this work, inductive coupling is the most relevant mechanism of AC interference and the most salient in terms of corrosion risk. The standard describes inductive coupling and its important factors as follows: AC flow in power conductors produces an alternating magnetic field around these conductors, thereby inducing AC potentials and current flow in an adjacent structure. The magnitude of the induced potential depends on many factors. The most important are:

(a) The overall separation distance between the structure and the power line;

(b) The length of exposure and the power line current magnitude;

(c) Changes in the arrangement of power line conductors or in separation distance;

(d) The degree to which current flowing in one power line conductor is balanced by the currents flowing in the others because of conductor arrangement and current distribution;

(e) The type of conductor used for the lightning shield wires on the power line;

(f) The coating resistance of the structure;

(g) The grounding present on the structure; and

(h) The soil resistivity as a function of depth.

Several organizations have composed documents outlining standard recommended practices for the control of AC corrosion. Among these are the NACE State-of-the-Art on AC corrosion,[22] the Canadian AC-Interference guideline report,[23] the ISO AC corrosion standard[24] and the European technical specification EN:15280.[25] These standards offer very similar guidance for AC corrosion control. The European technical specification suggests keeping i_{AC} to below certain likelihood thresholds as long as CP requirements are met:

- $i_{AC} < 30$ A/m^2: no or low likelihood
- 30 A/m^2 < i_{AC} < 100 A/m2: medium likelihood
- $i_{AC} > 100$ A/m^2: very high likelihood

The specification also suggests monitoring the ratio of i_{AC}/i_{DC} in the following manner:

- $i_{AC}/i_{DC} < 5$: low corrosion likelihood
- $5 < i_{AC}/i_{DC} < 10$: further investigation necessary
- $i_{AC}/i_{DC} > 10$: corrosion is likely, and mitigation should be pursued

The NACE State-of-the-art repeats these guidelines, as does the Canadian standard. These guidelines seem to be mostly based on the findings from German researchers which were compiled and summarized by Gummow et al.[26] In light of the industry-wide observation that cases of AC corrosion frequently occur even on pipelines within these thresholds, present guidelines and standards appear insufficient to control the problem of AC corrosion.

1.4 AC Corrosion - Overview of Mechanism

An induced electrical potential on a metal surface can serve to lower the "height" of the free energy barrier for various electrochemical reactions. Any change in potential away from the electrode potential for zero current flow (Ecorr) leads to an overpotential, η:

$$\eta = E - Ecorr \quad (1)$$

A positive overpotential leads to enhanced rates for oxidation (corrosion) reactions while a negative overpotential leads to enhanced rates of cathodic reactions. When a metal surface experiences an alternating potential, this overpotential alternates, at a certain frequency, between positive (anodic) and negative (cathodic). Assuming a sinusoidal signal, for AC-interference, this will take the form:

$$\eta(t) = E0\sin(\omega t) - Ecorr \quad (2)$$

where E0 is the amplitude of the alternating potential signal. For the duration of the positive potential portion of the alternating potential signal, the rate of oxidation of the metal will increase. For the negative portion, cathodic reaction rates, Equations (1) and (2), will increase. This situation is illustrated in Figure 1.1. The positive potential spikes induced by alternating voltage interference will momentarily increase the rate of the iron oxidation reaction and since corrosion is tied to the rate of the iron oxidation reaction, positive spikes in potential will lead to increased corrosion rates. The time-varying change in the oxidation reaction rate is the fundamental mechanism of AC-induced corrosion.

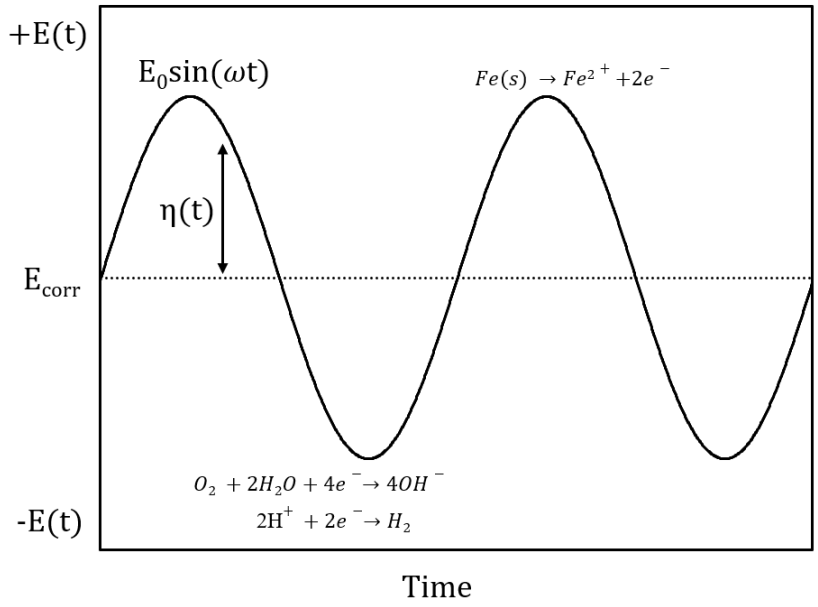

Figure 1.1: Time-varying change in the electrode overpotential, η, of a corroding metal experiencing sinusoidal AC interference.

1.5 Models for AC Corrosion

There are also some theoretical approaches developed trying to explain the way that AC produces and enhances corrosion. Gellings was among the first researchers to model AC corrosion rates of metals.[17] In that work, the influence of parameters such as Tafel slope (i.e. activation vs. transport control) were used to develop a generalized expression to estimate weight loss. However, no data or model validation was presented. Chin et al. proposed a preliminary theoretical approach to explain the polarization behavior of mild steel in a sodium sulfate solution with a superimposed AC potential.[16] In their model, a Butler-Volmer (B-V) style equation was used. While the comparison between the calculated polarization curves and the experimental results was limited at best, they reported oscillograms of the AC current response (current vs. time) as a function of frequency that showed a distortion in peak shape away from the "sinusoidal form." The magnitude of this distortion was a function of frequency, however, the frequency dependence was not explained by the authors.

Other theoretical investigations worth mentioning include the work of Bertocci and later by Bosch, both of which used a B-V style expressions of the form:[15,27]

$$i = i_{corr}\left[e^{\frac{(E_{DC}+E_0\sin(\omega t))}{\beta_a}} - e^{-\frac{(E_{DC}-E_0\sin(\omega t))}{\beta_c}}\right] \quad (3)$$

where: i is current density passing through the system, i_{corr} is the corrosion current density in the absence of applied alternating voltage, E_{DC} is the applied DC potential, β_a and β_c are anodic and cathodic Tafel slopes, E_0 is the peak potential and ω is the angular frequency of the AC signal. Equation (**Error! Reference source not found.**) assumes activation control and does not consider potential drop across the solution resistance or the effect of double layer capacitance. Bosch et al. were among a few researchers who considered the effect of diffusion phenomena on corrosion rate with applied AC potential.[15] In their analysis, they assumed that AC and DC polarizations do not influence each other and as a result, concentration of oxidants at the electrode surface consists of two separate DC and AC parts. However, the authors did not consider the effect of the solution resistance and double layer capacitance in their model. Based on their model, Bosch et al. concluded that the increase in the corrosion rate was limited by the diffusion-limited current density. This conclusion has been shown to be incorrect.[28]

In comparison, Lalvani *et al.* proposed a model that considered both potential-drop across the solution resistance and the effect of double layer capacitance.[29] In that model a simple Randles' circuit was assumed, where the total potential drop in the system (E_T), was the sum of DC and AC potentials:

$$E_T = E_{DC} + E_0 \sin \omega t \quad (4)$$

In this model E_T was equal to the sum of the potential drop across the electrochemical interface (E) plus the potential drop across the solution resistance (R_s):

$$E_T = E + i_T R_s \tag{1}$$

The total current flow (i_T) across the interface was defined as the sum of the capacitive current (i_c) and the faradaic current (i_F):

$$i_T = i_c + i_F \tag{2}$$

where iF is the sum of the anodic (i_o) and the cathodic (i_r) currents:

$$i_F = i_o + i_r \tag{3}$$

The current flow through the interfacial capacitance (C_i) was defined as:

$$i_c = C_i \frac{dE}{dt} \tag{4}$$

Substituting Equations (**Error! Reference source not found.**) and (**Error! Reference source not found.**) into Equation (**Error! Reference source not found.**) and further combination of result with Equations (**Error! Reference source not found.**), (**Error! Reference source not found.**) yielded a general expression for the potential drop across the interface:

$$\frac{dE}{dt} + \frac{E}{C_i R_s} + \frac{i_O + i_R}{C_i} = \frac{E_{DC} + E_0 \sin \omega t}{C_i R_s} \tag{5}$$

Lalvani et al. also considered both anodic and cathodic reactions under activation control. In their model, the values of i_o and i_r had their traditional Tafel definitions:

$$i_o = i_{corr} e^{\frac{(E - E_{corr})}{\beta_a}} \tag{6}$$

and

$$i_r = i_{corr} e^{-\frac{(E - E_{corr})}{\beta_c}} \tag{7}$$

where E_{corr} is the corrosion potential measured in the absence of AC. Substituting Equations (**Error! Reference source not found.**) and (7) into Equations (**Error! Reference source not found.**) led to their final nonlinear differential equation for E:

$$\frac{dE}{dt}+\frac{E}{C_i R_s}+\frac{i_{corr}e^{\frac{(E-E_{corr})}{\beta_a}}+i_{corr}e^{-\frac{(E-E_{corr})}{\beta_c}}}{C_i}=\frac{E_{DC}+E_0\sin\omega t}{C_i R_s} \quad (8)$$

In this model, Lalvani et al. obtained numerical solutions using two different methods, one using a linear model and the other using a perturbation method.[30] Based on their models, the corrosion current should be lower at higher frequencies, in agreement with experimental data.[31] Another conclusion from this model is that the ratio of the anodic to cathodic Tafel slopes (r) defines a change in corrosion potential caused by the AC perturbation although that point will be rebutted here. In the linear model, they assumed the applied DC potential to be close to the open circuit potential (OCP). For the perturbation analysis they assumed that the ratio of DC corrosion current to the double layer capacitance value is much lower than unity and, therefore, could be neglected.[30,31] Due to assumptions in their numerical solution, the DC potential does not have any influence on AC corrosion rates, which is in contrast with the results obtained by others. In this work we proposed a model based on Equation (**Error! Reference source not found.**) by Lalvani.[30]

Factors addressed by the new model develop by Ghanbari and Lillard[28] that previous models have omitted include: the effect of solution resistance, mixed cathodic reactions such as transport limited oxygen reduction, and hydrogen evolution. The model is, in part, based on the work by Lalvani' (Equation 12).[30] One of the assumptions in Equation (12) is that the Faradaic currents i_o and i_r can be described by activation control which is not always the case. Typically, at moderate overpotentials, the cathodic reaction is controlled by the diffusion limited oxygen reduction ($i_{r,O2,}$) while at lower potentials by hydrogen evolution ($i_{r,H2}$). As such, we present a modified B-V exponential function that describes the anodic reaction under activation control while the cathodic reaction is assumed to be under mixed control:

$$i_r = i_{r,O_2} + i_{r,H_2} \quad (13)$$

where the mass transport limited oxygen reduction rate is governed by the expression:[32]

$$i_{r,O_2} = i_{corr}\frac{e^{2.3\frac{(E-E_{corr})}{\beta_c}}}{1-\frac{i_{corr}}{i_l}+\frac{i_{corr}}{i_l}e^{2.3\frac{(-E+E_{corr})}{\beta_c}}} \quad (14)$$

where: i_L is the limiting current density of oxygen reduction and the remaining terms take the usual meaning. The hydrogen evolution reaction rate is governed by the Tafel equation:[33]

$$i_{r,H_2} = i_{0H_2}e^{2.3\frac{(-E+E_0)}{\beta_{H_2}}} \quad (15)$$

where: i_{0H2} is hydrogen exchange current density and is a function of the nature of the cathode, E_0 is the hydrogen standard equilibrium potential that is equal to zero in the SHE scale and β_{H2} is the Tafel slope of the hydrogen evolution reaction.

Substituting Equations (**Error! Reference source not found.**) and (**Error! Reference source not found.**) in Equation (**Error! Reference source not found.**) and following combination of Equations (**Error! Reference source not found.**),(**Error! Reference source not found.**) and (**Error! Reference source not found.**) leads to the nonlinear equation for potential drop across the Faradaic resistance (E):

$$\frac{dE}{dt} + \frac{E}{C_i R_s} + \frac{\xi}{C_i} = \frac{E_{DC} + E_0 \sin \omega t}{C_i R_s} \tag{16}$$

where:

$$\xi = i_{corr}\left(e^{2.3\frac{(E-E_{corr})}{\beta_a}} - \frac{e^{2.3\frac{(-E+E_{corr})}{\beta_c}}}{1-\frac{i_{corr}}{i_l}+\frac{i_{corr}}{i_l}e^{2.3\frac{(-E+E_{corr})}{\beta_c}}}\right) + i_{0H_2}e^{2.3\frac{(-E-0.244)}{\beta_{H_2}}} \tag{17}$$

Ghanbari and Lillard used this expression to model corrosion rates of carbon steel API grade X65 pipeline steel in sodium chloride solutions with and without AC at different DC potentials.[28] The model was benchmark using weight loss analysis. Both experimental and model results showed the importance of the interfacial capacitance on the rate of AC corrosion, especially at a frequency of 60Hz. The model was also used to explain the observation that the AC corrosion rate was equal to the average AC current in the system.

1.6 Cracking Susceptibility Under AC Interference

Few studies have been carried out to investigate the influence of AC interference on the environmentally assisted cracking (EAC) of pipeline steels. The fact that localized corrosion has been found in the failures under AC interference, raises concerns of its potential influence to promote cracking. Pitted sites have been shown to facilitate the crack initiation process in metals. Research in high pH environments has found that crack nucleation appears to increase with increasing pit density due to higher stress concentration.[34] Additionally, it has been shown that the AC signals can increase the anodic and cathodic current densities, affecting the Tafel slopes and kinetics of the reactions. Therefore, an increase in the oxygen and hydrogen evolution under the AC influence could also induce embrittlement in the structure.[35] Wan et al. studied the effect of AC current densities on the SCC behavior of X80 pipeline steel in near-neutral NS4 solution. The SCC susceptibility increased with higher AC current densities. Pits were found near the fracture surface of the specimens with secondary cracks and brittle fracture. The mechanism of cracking was attributed to anodic dissolution and hydrogen embrittlement promoted by the AC faradaic

currents.[36] Research has also suggested that unstable conditions of cathodic polarization applied to the pipeline steels can affect the cracking susceptibility.[37]

Zhu et al. investigated the cracking behavior of X80 steel under the short-term application of AC current densities in a high pH carbonate solution. The passivity of the steel was degraded by the AC interference.[38] The SSR tests showed the elongation loss rate increased rapidly above a critical AC current density threshold of 30 A/m^2. The potentiodynamic polarization curves showed a decrease in the passivation region with increasing AC current density and the occurrence of pitting on the sides near the fracture was attributed to a change in the critical pitting potential.[38] The authors correlated pitting with cracking and an intergranular fracture mode. However, studies under long-term AC superimposition performed by the same authors showed a change in the mode of crack propagation under the AC interference. Intergranular cracking was observed without AC while transgranular cracking was observed with AC current applied. The SSR experiments with applied AC current densities of 30 to 300 A/m^2 showed that the elongation-loss rate and reduction in area were greater for the samples with AC current applied, especially at the current density higher than 100 A/m^2. A brittle fracture was observed under AC influence, along with wide and deep cracks at the sides near the fracture. The transgranular fracture morphology under AC interference was believed to be controlled by the mechanisms of anodic dissolution and hydrogen embrittlement.[39]

Parameters such as the AC waveform and frequency have also been studied to evaluate the SCC behavior in pipeline steels.[38] Sinusoidal, square, and triangular AC waveforms were applied to the pipeline steel in a high pH solution. All three waveforms of AC influence increased the susceptibility to cracking. However, the triangular wave showed the highest susceptibility associated with higher cathodic currents and an intense hydrogen evolution reaction was possibly responsible for the propagation of cracks. The transition from intergranular to transgranular morphology was evidenced only under the AC interference. The parameter of AC frequency and its influence on the SCC susceptibility have also been studied.[40] The SCC susceptibility was found to be higher at lower frequencies (around 30 Hz) with brittle fracture morphology, possibly due to longer time for the migration of ions, and the transport and absorption of hydrogen on the surface.

The crack propagation rate (CGR) of steel under applied AC was investigated using compact tension (CT) specimens in a cyclic load test setup. When 5 V rms AC was applied with a DC potential of −580 mV/SCE, the crack length increased rapidly compared to that without the AC signal. Longer and deeper cracks were observed under the AC influence. In contrast, the cracks without AC interference were short and narrow, with some branches indicating classic IGSCC. The authors concluded that the CGR of the steel was increased from 7.48×10^{-7} to $7.056 \times 10^{-6}\ mm/s$, due to the AC influence.[41]

The effect of AC on EAC is rather complicated, partly because it is due to the conjunctive action of the positive and negative cycles on the steel surface. For that reason, Wan et al. studied only the negative half-wave AC signal and its magnitude on the SCC behavior in a neutral NS4 solution. Their results showed low SCC susceptibility under the AC current densities of 10 A/m^2 and 20 A/m^2. The application of AC with the negative half-wave current densities greater than 30 A/m^2 led to severe corrosion, enhanced cathodic hydrogen reaction and higher susceptibility to SCC. The increased SCC susceptibility was explained by the mechanism of hydrogen-induced embrittlement in the steel.[42] To elucidate the effect of hydrogen on this phenomenon, Schmitt et al. studied the hydrogen diffusion behavior with hydrogen permeation tests under the AC current densities from 30 to 500 A/m^2. No clear indication was found about the AC influence on the hydrogen transport mechanism.[43] These studies show how the AC interference can be detrimental by accelerating cracking in the structure. However, none of these studies considers the effect of AC interference under the CP conditions, which is commonly found for pipelines in the field.

2. EXPERIMENTAL PROCEDURES

2.1 Potentiodynamic Polarization Curves

Potentiodynamic polarization curves were conducted using a three-electrode electrochemical cell (Figure 2.1) with a saturated calomel electrode (SCE) as the reference electrode (RE) andeither a niobium-coated stainless steel mesh counter electrode (CE) or a graphite rod counter electrode. Experimental samples (WE) were made from X65-grade pipeline steel taken from a pipeline in Argentina as per Ghanbari et al.[44] Samples were machined to a 12.6 mm tall, 9.6 mm wide cylinder (4.5 cm^2 surface area) electrode tapped with a 10-32 thread insert for connection with a threaded steel rod. Samples were polished using 240, 320, 400 and then 600 grit SiC polishing paper and DI water as lubricant. The steel rod was isolated from solution using a Teflon gasket sealed against a glass tube with a rubber O-ring. The RE was placed close to the WE by using a Luggin-Haber capillary tube. Tests were performed using one of either a Princeton Applied Research 273A or 263A, Solartron 1287, Gamry Reference 600, or BioLogic VSP-300 potentiostat.

Polarization tests were run by first allowing the sample to reach a steady OCP (1 hour of immersion). Anodic or cathodic polarization was then run at a 0.1667 mV/s scan rate. Results were corrected for IR-error at the end of tests by subtracting the $I*R_S$ from each potential reading. R_S was determined by the impedance at high frequency from EIS. The Gamry Reference 600 potentiostat was capable of automatic IR-compensation. Tests run using this feature did not require manual IR-error correction.

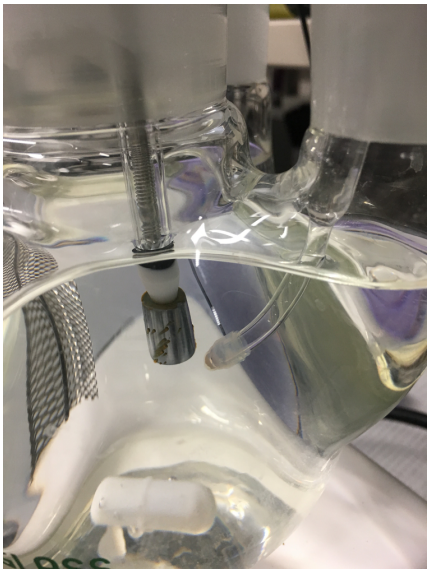

Figure 2.1: Image of three-electrode electrochemical cell showing the cylindrical working electrode sample, reference electrode Luggin capillary tube, and mesh counter electrode.

2.2 Mass Loss

Mass loss experiments were conducted to measure corrosion rates of steel afflicted by AC by using a three-electrode cell. However, graphite counter electrodes were prone to obliteration under the high compensation voltages needed to maintain large voltages (≈3 V_{RMS}) on the WE. Niobium-coated Stainless-Steel mesh CEs were used instead of graphite. These tests were limited to the Princeton Applied Research 273A or 263A, or Solartron 1287 potentiostats. These potentiostats have an external input that allows for the simultaneous application of a sinusoidal voltage on the working electrode and a DC bias in reference to a Saturated Calomel Electrode. Externally applied sine waves were produced using one of either a Tektronix AFG2021 Function Generator, Solartron SI 1255 or 1260 Frequency Response Analyzer. Figures 2.2 and 2.3 show the cell setup used for these experiments.

Tests were conducted for approximately a total of six weeks. The experimental workflow was generally conducted as follows: Immersion in solution, EIS, OCP for 30 min (minimum time to achieve a steady -0.68 V vs. SCE), EIS, application of AC for 2 weeks, EIS, application of AC for 2 weeks, EIS, application of AC for 2 weeks, EIS and then mass loss by following the procedures of ASTM G1-03 for chemical cleaning of iron and steel.[45] Mass loss was measured to an accuracy of 0.1mg.

Samples were maintained at a constant DC potential of either -0.78, -0.85, -1.0, -1.2, or -1.5 V vs. SCE. The constant DC bias values are in the typical range of cathodic protection potential values. An alternating voltage of 2-5 V_{RMS} was used with 3 V_{RMS} being applied to most samples. The Solartron FRAs were limited to 3 V_{RMS} while overall cell current was limited to around 150 mA. This means a maximum of around 320 A/m^2 of AC could be imposed on any one sample with some limitations on the compensation voltage as well. To overcome this current density limitation, some test samples were taped off using electrochemist's tape to restrict the exposed surface area.

Periodic measurements of RMS voltage and current were taken using an oscilloscope and the external output from the potentiostats. Phase differences between the voltage and current waveforms could also be tracked in this way. The waveforms were recorded for up to one second intervals using a USB6015 DAQ from National Instruments. The recorded values were averaged to get the final AC density.

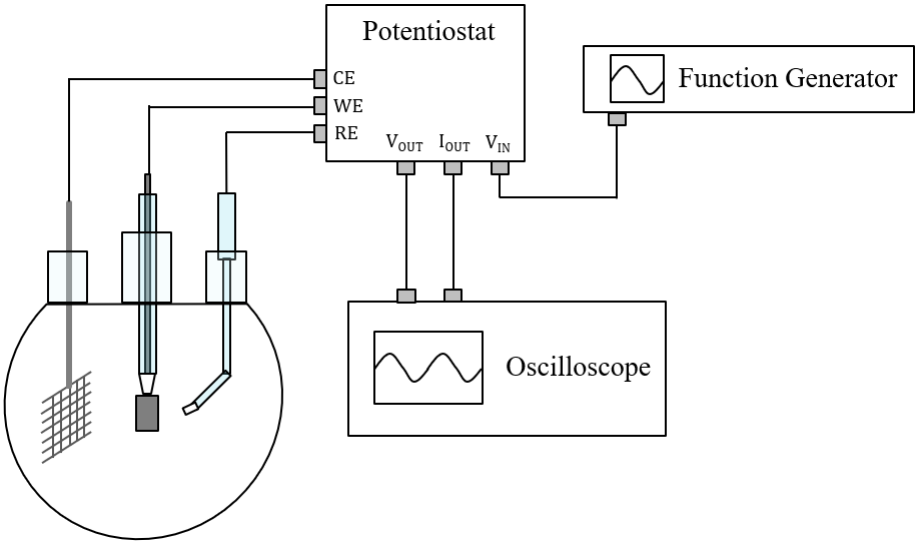

Figure 2.2: Schematic of three-electrode cell setup with potentiostat, function generator for generating AC, and oscilloscope for waveform monitoring.

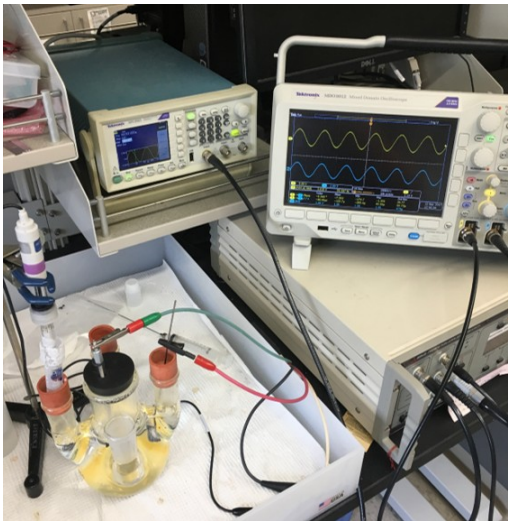

Figure 2.3: Image of three-electrode cell setup with potentiostat, function generator for generating AC, and oscilloscope for waveform monitoring.

Mass loss tests were performed in a modified NS4 (originating from Parkins[46]) solution with the following chemical composition shown in Table 2.1 The solution composition was modified from that quoted in literature by removing Ca^{+} and Mg^{2+} containing compounds and adding appropriate amounts of KCl and $NaSO_4$ to achieve an equivalent content of chloride and sulfate. This was done to eliminate the confounding effects of scaling on steel samples. The chemicals were added to ultrapure 18.2 MΩ-cm DI water. This modified NS4 solution was measured to have a pH of 8.2 and a conductivity of 1200 μS/cm (resistivity of 830 Ω-m).

Table 2.1: Composition of Modified NS4 Solution

Compound	Mass (g/L)
KCl	0.3056
$NaHCO_3$	0.483
$NaSO_4$	0.0633

2.3 Field Experiments

2.3.1 Rosebush, MI

A cathodic protection testing and training facility in Rosebush, MI was used for field experiments. This facility was provided for temporary use by Mears Group, Inc. A schematic of the facility is shown in Figure 2.4. Field experiments consisted of several rounds of buried coupon exposure. Coupons were constructed from a 1018 carbon steel rod cut into 2" segments. Each segment was polished using 240, 320, 400 and then 600 grit SiC polishing paper and DI water as lubricant. 14 AWG wire was attached to the samples using electrical crimp terminals and a screw-on coupon holder. The coupon was wrapped in electrical tape to expose only the desired area (10 cm^2) to soil. The samples were affixed to the end of a PVC pipe (Figure 2.5) and buried to the approximate depth of the test pipelines.

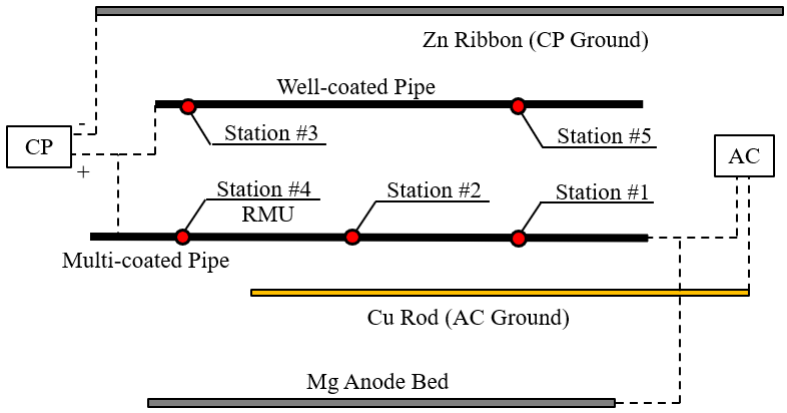

Figure 2.4: Pipeline and ground bed installation schematic of the cathodic protection training facility in Rosebush, MI. This facility was used for field testing from April to December 2017.

CP was supplied by a pre-installed magnesium anode bed to provide a steady -1.1 V vs. CSE on-potential. The CP-rectifier installed on this system was not used to supply CP due to interference problems with the rectifier anode shunting much of the applied AC. AC was controlled by a Variac device with a copper rod acting as the electrical ground. For safety reasons, the AC voltage was limited to 25 V_{RMS}. This system was able to supply AC densities around 100 A/m^2. Samples were installed at 5 test stations on either the well-coated pipe or the multi-coated pipe. One test station (Station #4) was outfitted with a Mobiltex corTalk RMU for remote monitoring of the coupon.

Coupons were assessed for adherent soil and corrosion damage morphology upon removal from the test field. Then, samples were weighed for mass loss to determine corrosion rates by following the procedures of ASTM G1-03 for chemical cleaning of iron and steel.

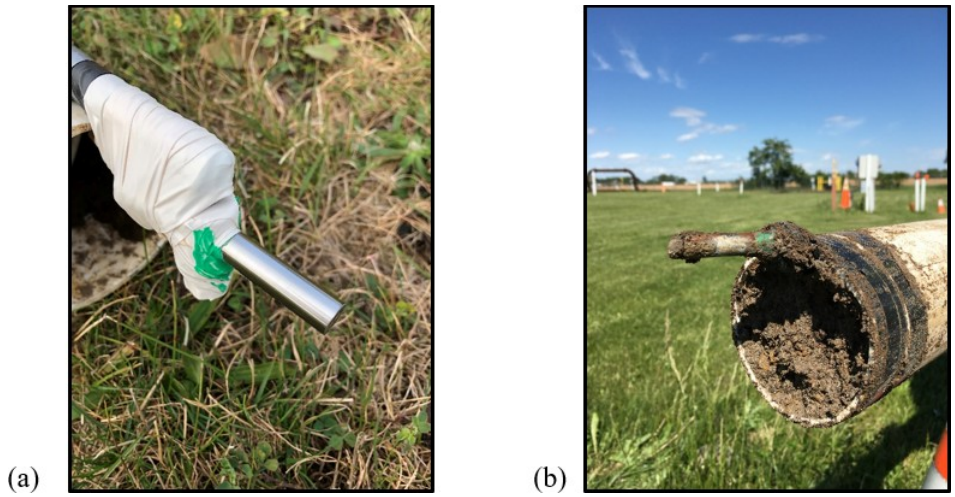

Figure 2.5: Samples before (a) and after (b) field testing at the Rosebush CP site.

2.3.2 La Grange, TX

Corrosion coupon field tests were conducted at the Quanta Services Lazy Q Ranch in La Grange, TX. A cathodic protection training facility at the site was outfitted with AC capability. In contrast to the Rosebush site, this facility allowed for the simultaneous use of a CP-rectifier and AC application. The AC was supplied by a variac connected to the power line mains. The system was set up so that an unused pipeline was used as the AC-ground in order to maximize the achievable AC density on coupons. A separate pipeline was used as the CP-ground rather than an anode ground bed as this decreased the mitigation effect of the CP loop on the AC loop.

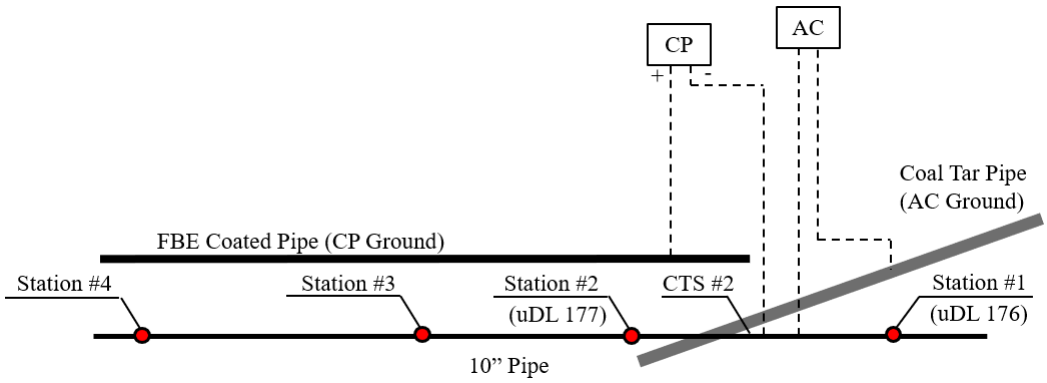

Figure 2.6: Pipeline and ground bed installation schematic of the cathodic protection training facility in La Grange, TX. This facility was used for field testing from May to December, 2018.

Coupons were attached to PVC pipes to be buried in the soil. In an effort to increase AC densities, several coupons were taped off to expose only 1 cm^2 as opposed to the 10 cm^2 on other coupons. A Mobiltex or Talk uDL2 was installed on Stations #1 and #2 to measure continuous AC, DC, off-potential, on-potential, and AC potential. Coupons were weighed for mass loss to determine corrosion rates by following the procedures of ASTM G1-03 for chemical cleaning of iron and steel.[45]

An electrical resistance (ER) probe was also used to measure instantaneous corrosion rates on a cylindrical sample. The electrical resistance of the probe is a function of its material thickness and can thus indicate metal loss which can be converted to a corrosion rate. Figure 2.8a, and b show the ER probe and data logger device from Metal Samples Company. The ER coupon was buried in the same manner as the mass loss coupons. The large coupon area was restricted with electroplating tape to expose an area of 10 cm^2 at the tip of the probe. This probe and data logger were able to record electrical resistance data at hourly intervals.

(a) *(b)*

Figure 2.7: Images of the La Grange cathodic protection test site showing several installed test stations.

(a) *(b)*

Figure 2.8: ER Probe (a) after removal from testing showing the taped probe area and the corresponding data logger (b) to gather electrical resistance data.

2.3.3 Seabrook, TX

An active pipeline in the charge of Marathon Pipe Line LLC in Seabrook, TX was identified as a hotspot of alternating voltage. This pipeline was collocated with multiple high-voltage transmission lines in a corridor with several other pipelines. Prior investigations revealed alternating voltages up to 15 V_{RMS} at this location. Cathodic protection was provided by an active system and on-potentials were consistently in the range of -1.2 V. Figure 2.9b shows two images of the Seabrook site. A mass loss sample of 10 cm^2 and an ER probe (same as above) with a 10 cm^2 exposed area were buried about 3 feet into the soil with cables attached to the installed posts. A Mobiltex corTalk uDL2 was installed on the ER probe and the mass loss coupon to measure continuous AC, DC, off-potential, on-potential, and AC potential. Mass loss was used to determine corrosion rates by following the procedures of ASTM G1-03 for chemical cleaning of iron and steel.[45]

(a) *(b)*

Figure 2.9: Images of the Seabrook pipeline installation location. (b) The ER probe and mass loss sample station is seen in the foreground while the ultrasonic corrosion probe is located near the solar panel instrument station.

2.4 Experiments in Artificial Soils

To control the composition of soils in the laboratory environment, artificial soils were composed of commercially sourced sand, silt, and clay minerals. The trade names and types of the clay minerals used were KY Ball Clay (Illite Clay), Edgar Plastic Kaolin (Kaolin Clay), and McNamee Kaolin (Kaolin Clay). The silt minerals used were feldspar potash and 200 mesh silica. The sand mineral was 30 mesh quartz sand. The chemical compositions of these minerals, confirmed by EDS, is shown in Table 2.2

Table 2.2: Names and Compositions of Soil Minerals (at%)

	KY Ball Clay (Illite)	EPK (Kaolin)	Feldspar Potash	McNamee (Kaolin)	200 Mesh Silica	30 Mesh Sand
Si	14.04	11.61	22.14	10.35	23.00	25.80
Al	10.73	12.39	6.50	10.43	0.21	3.15
O	74.86	75.07	65.60	79.22	70.88	
K	0.36	0.92	4.98	-	0.06	0.17
Na	-	-	0.78	-	-	-
Total	100.00	100.00	100.00	100.00	100.00	100.00

The sand, silt, and clay minerals were mixed in predefined portions according to the USDA soil texture triangle to develop the following categories of artificial soil: Sand, Sandy Clay, Sandy Loam, Clay, Silty Clay and Silty Clay Loam. These categories are displayed on the USDA soil texture triangle shown in Figure 2.10.[47] The composition of soil minerals in each soil category is tabulated in Table 4.3. The soils were mixed with the raw clay, silt, and sand mineral components and then solution was slowly added while mixing. Most soils were mixed using 0.1 M NaCl solution to a saturated state (the soil would no longer hold water).

Table 2.3: Composition of Artificial Soils (wt%)

Soil Type	Soil Name	Sand	Sandy Clay	Sandy Loam	Clay	Silty Clay	Silty Clay Loam
Clay	KY Ball Clay	0	10	5	12.5	12.5	7.5
Clay	EPK	0	10	5	12.5	12.5	7.5
Clay	McNamee	0	20	10	25	25	15
Sand	30 Mesh	100	25	70	20	5	20
Silt	200 Mess	0	25	5	15	5	20
Silt	Feldspar	0	10	5	15	40	30
	Total	100.00	100.00	100.00	100.00	100.00	100.00

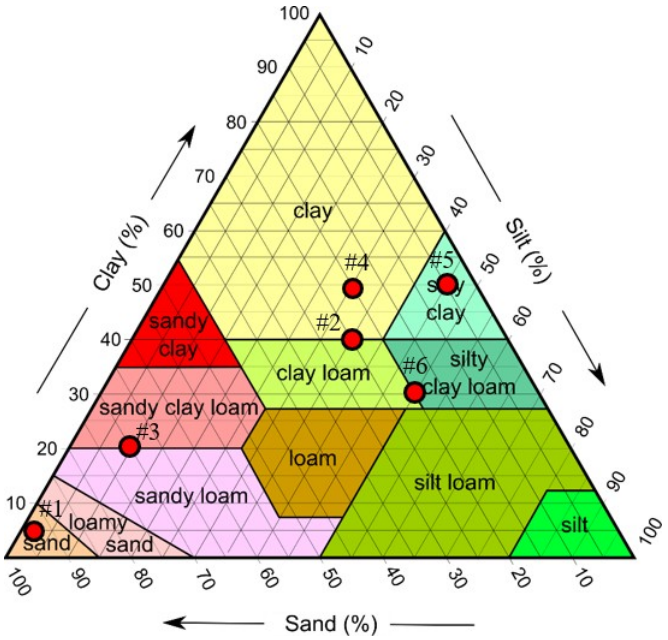

Figure 2.10: USDA soil texture triangle showing the location of artificially constructed soils. Triangle reproduced from [9].

2.5 Slow Strain Rate Experiments

2.5.1 Materials and Test Solutions

In the SSRT study, carbon steel 1018 (UNS G10180) and API (American Petroleum Institute) X65 steel, commonly used for pipelines were used. The chemical composition and mechanical properties of the steels are given in the Table Error***! No text of specified style in document.***.4 and Table 2.5, respectively.[48,49] The cylindrical tensile specimen has a gauge section with an average of 3.22 ± 0.2 mm in diameter and 27 ± 0.2 mm in length, as shown in Figure 2.11. These tensile samples were supplied by Metal Samples. Before each test, the surface of the samples was ground to grit 1200 with SiC abrasive paper. After polishing, the samples were rinsed with deionized (DI) water, degreased with ethanol and blown-dried with Ar gas (99.998%). The initial immersion area of the specimen was 11 cm^2 (Figure 2.11b). In order to evaluate the effect of the AC current densities under the AC voltage conditions, the immersion area was reduced by covering the non-gauge section of the tensile sample with an epoxy paint (Figure 2.11a). Only the gauge section of the sample was immersed, and the final area in contact with the solution was ~3.8 cm^2.

*Table **Error! No text of specified style in document.**.4. Chemical composition (wt.%) of the carbon steel 1018 and API X65.*

Steel	C	Mn	P	S	Si	Nb	Ti	Ni	Cu	Fe
1018	0.15-0.20	0.60-0.90	≤0.04	≤0.05	-	-	-	-	-	bal
API X65	0.28	1.40	0.020	0.030	0.45	0.05	0.06	0.16	0.23	bal

*Table **Error! No text of specified style in document.**.5. Mechanical properties of carbon steel 1018[48] and API X65.[49]*

Carbon steel	Ultimate Tensile strength (MPa)	Yield Tensile strength (MPa)	Modulus of elasticity (GPa)
1018	448	370	205
API X65	531 - 758	448 - 598	210.7

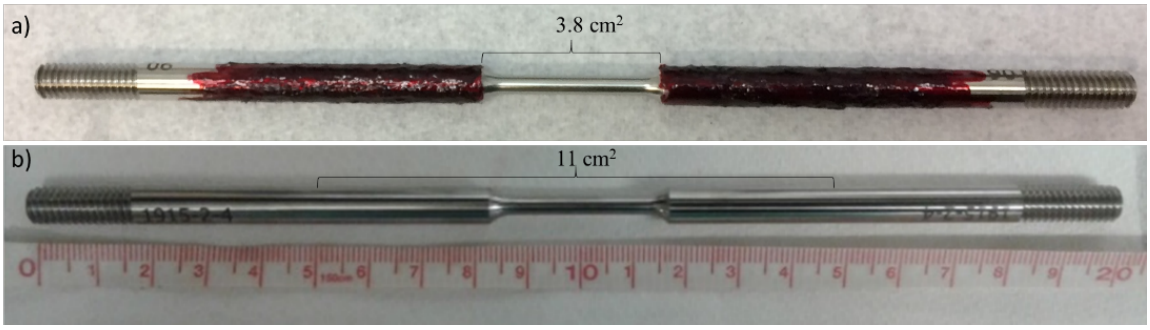

Figure ***Error! No text of specified style in document.****..11. Photos of a cylindrical tensile specimen used for SSR testing, (a) reduced immersed area of 3.8 cm² by epoxy coating, and (b) with 11 cm² of immersed area.*

The solution used as a corrosive environment was NS4, which simulates typical soil composition for laboratory testing. The composition of NS4 solution is KCl (0.122 g/L) + $NaHCO_3$ (0.483 g/L) + $CaCl_2 \cdot 2H_2O$ (0.181 g/L) + $MgSO_4$ (0.131 g/L).[50] and was prepared with analytic grade reagents and DI water (18.2 MΩ·cm resistivity). The solution volume in the test cell was approximately 300 mL.

2.5.2 Electrochemical Parameters

The slow strain rate tests (SSRT) were performed on a CERT machine (Cortest Company) with a load capacity of 4536 kgf (Figure 2.12a). After the specimen was fixed in place, a pre-load of 100 kgf was applied manually to securely fasten the specimen. The test procedure and selection of parameters (e.g., strain rates) were according to the ASTM G129 standard.[51] All the measurements were performed at room temperature and open to air. During the tensile test, the carbon steel specimen was slowly pulled at a constant strain rate until failure while it was subject to cathodic potentials and AC voltages inside an electrochemical cell (Figure 2.12b). Figure 2.12c is the schematic diagram of the electrochemical cell.

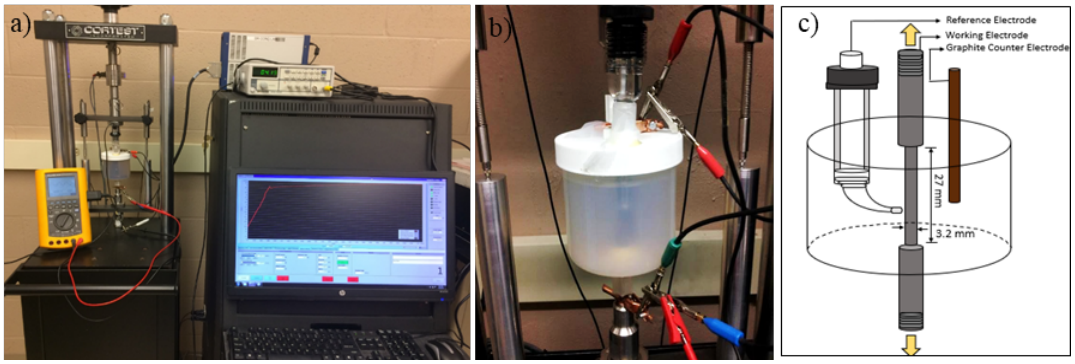

Figure ***Error! No text of specified style in document.****..12. (a) SSR test setup, (b) electrochemical cell, and (c) schematic diagram of the electrochemical cell.*

A conventional three-electrode cell was used for the application of DC and/or AC potentials. The counter electrode was a graphite rod (10 cm long and 6 mm in diameter), the reference electrode (RE) was a saturated calomel electrode (SCE), and the working electrode (WE) was the carbon steel tensile sample. A Lugging capillary was used to minimize IR-drop and the distance between the WE and RE was approximately 5 mm. Three different levels of cathodic potentials were applied to the tensile specimens by using a Gamry 600+ potentiostat (−0.774, −0.85 and −1.12 V *vs.* SCE), with and without impressed AC voltages. These cathodic potentials were chosen based on the field applications and their conversion to the copper/copper sulfate electrode (CSE) is listed in Table 2.6. The AC signal was generated by a function generator (GM Instek SFG-1013) that was connected to the external input of the potentiostat. Three different levels of AC voltages (1, 2 and 3 V rms (root mean square)) were applied at a constant frequency of 60 Hz.

*Table **Error! No text of specified style in document.**.6. Cathodic potentials applied to the tensile specimens vs. saturated calomel electrode (SCE) and copper/copper sulfate electrode (CSE).*

Cathodic Potentials	
V *vs.* SCE	V vs. CSE
−0.77	−0.85
−0.85	−0.93
−1.12	−1.20

The schematic process of the SSRT is presented in Figure 2.13. Before the application of CP and/or AC potentials and tensile force, an initial pre-corrosion for 24 hours in NS4 solution was performed. This was done to form a layer of natural corrosion products on the sample surface, simulating a corroded pipe surface in the field. The open circuit potential (OCP) was continuously measured over time. After the pre-corrosion period, different levels of CP and/or AC potentials were applied for another 24 hours before the start of an SSRT. This is termed as the pre-charging period, which allowed the samples to reach a steady state under the DC/AC electrical fields. The pre-corrosion and pre-charging periods of the sample prior to the tensile experiment make it possible to simulate the surface conditions of pipelines in the field. After the initial 48 hours of pre-corrosion and pre-charging periods, SSRT was started by pulling the sample continuously at a constant strain rate until failure under the DC/AC influence.

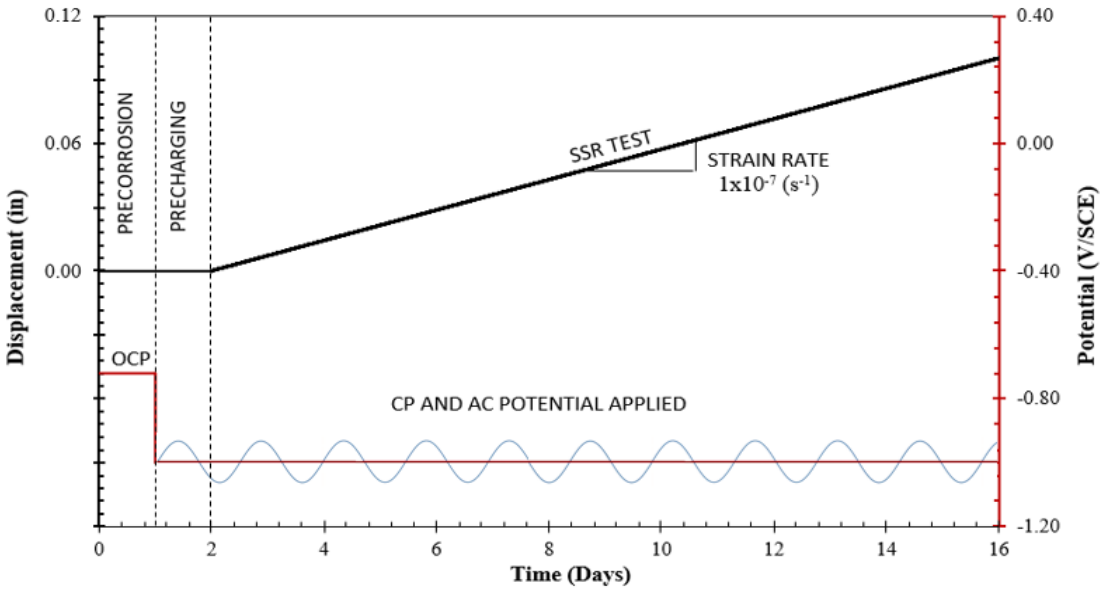

Figure ***Error! No text of specified style in document.****..13. Schematic diagram of the SSRT process under the AC and CP conditions.*

Depending on the metal-environment system, the strain rate plays an important role in the detection of SCC using SSRT. In general, slower strain rate is more suitable for studying SCC phenomenon since it allows sufficient time for the electrochemical reactions to occur. However, longer time is needed to complete the test when the strain rate is decreased. In this study, several strain rates were first evaluated to choose the optimal rate that was neither too fast to inhibit the SCC process or too slow to complete the test within reasonable timeframe. The range of strain rates was evaluated from 10^{-5} to 10^{-7} in/s in NS4 solution and in inert environment (lab air), in accordance with the ASTM G129 standard.[51]

During the test, the DC current-time response was recorded by the Gamry potentiostat and also measured by a multimeter (Fluke 115 True RMS digital) and an oscilloscope (Tektronix TDS 2012C). The real-time AC sinusoidal wave signals were recorded by the multifunction data acquisition card (DAQ, USB 6215 from National Instruments), interfaced with the LabVIEW software.

After the completion of the tensile tests, the surface of the broken specimens was examined, the final diameter and elongation was measured by a Mitutoyo ABS digimatic caliper (model C-D 8" ASX). Important parameters were calculated including the percentage of plasticity loss (Iδ (%)), the reduction area ratio (RAR), and the ratio of time to failure (RTTF).

2.5.3 Surface Analysis

Optical microscopic images of the samples were taken using the stereomicroscope (Nikon SMZ 745T) with a working distance of 115 mm. It was used to examine the mode of fracture and the gauge section of the SSRT specimens.

Scanning electron microscopy (SEM, Hitachi TM 3030) with an accelerating voltage of 15 kV was used to analyze the morphology of the SSRT samples under the different DC/AC potentials. When higher resolution was necessary, a TESCAN LYRA 3 field emission SEM was used to evaluate the morphology of the fracture surfaces and the necking regions, with secondary electron (SE) mode and an accelerating voltage of 30 kV. Energy dispersive X-ray spectroscopy (EDS) was used to analyze the elemental composition of corrosion products on the metal surface.

The characterization of pit distribution on the gauge section of the samples and the measurement of pit depth were carried out with the 3D microscope (ALICONA infinite focus G5).

3. RESULTS AND DISCUSSION

3.1 The Relationship Between Cathodic Protection Levels, AC Current Density, and Corrosion Rate for Pipeline Steel

With cathodic protection, negative polarization of the steel can reduce the oxidation reaction to a residual fraction of its normal equilibrium reaction rate, with more negative potentials reducing the rate of oxidation even further. Alternating potential interference will create periodic increases in potential which reduce the effectiveness of the cathodic polarization. In this manner, the AC corrosion of cathodically protected steel is dependent on the magnitude of both the cathodic potential and the alternating potential across the steel interface. Measuring the interfacial potential would then allow for estimates of corrosion rate. But due to IR-error, direct measurement of interfacial potentials is impossible. Thus, researchers have relied on the measurement of current density as a substitute. But since there is no direct conversion from AC density to corrosion rate, measurements are, at best, only a guideline, and multiple factors must be considered.

This chapter will present and discuss the results of experiments designed to establish the relationship between cathodic protection, AC current density, and corrosion rate on steel. Long-term mass loss tests in laboratory conditions and in field test environments were conducted where alternating potentials were induced on cathodically protected steel coupons. The results are discussed in terms of the electrochemical understanding of AC corrosion.

3.1.1 Open Circuit Potentials of X65 Steel

Before potentiodynamic and laboratory mass loss experiments, X65 steel samples were allowed to come to a stable OCP for about 30 minutes. Figure 3.1 shows a typical OCP measurement during the first 30 minutes of immersion in modified-NS4. The final potential value was around -675 mV_{SCE} and other tests confirm the steel does not vary from this OCP at longer times. The stable OCPs of X65 steel in various environments obtained by voltage vs. time measurements are shown in Table 5.1.

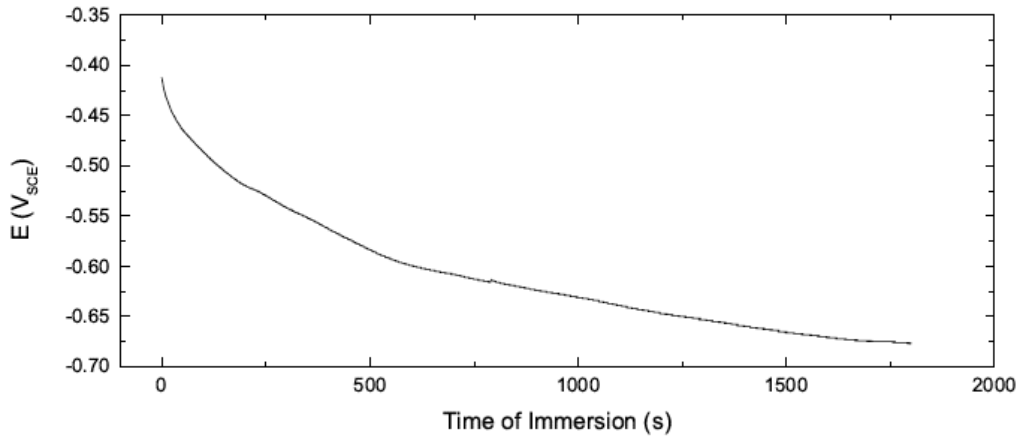

Figure 3.1: Open Circuit Potential of X65 steel in modified-NS4 solution before potentiodynamic polarization.

OCPs in soil are closely correlated to the moisture content of the soil with lower moisture content leading to more positive potentials. See Table 5.2 for an example. This is because the oxygen diffusion rate is greater in dry soil and the limiting current density for diffusion-limited oxygen reduction is increased. A study by Noor and Al-Moubaraki also demonstrates this by showing OCPs ranging from -540 mV_{SCE} at 2.5 % moisture content to -790 mV_{SCE} at 20 % moisture content[52]. Since most OCPs in this dissertation were obtained in saturated soil conditions, it is difficult to derive meaning from the OCP measurements, but they are presented here for completeness.

Table 3.1: Long-term stable open circuit potential of X65 steel in various environments.

Solution/Environment	OCP Range (mV_{SCE})
Modified-NS4	-680 to -720
0.1 M NaCl	-610 to -650
Sand	-640 to -710
Clay Soil	-650 to -690
Sandy Clay Soil	-600 to -700
Silty Clay Loam Soil	-680 to -720
Sandy Loam Soil	-700 to -715
Silty Clay Soil	-620 to -650

Table 3.2: Long-term stable open circuit potential ranges of X65 steel in sandy loam soil at 4-6 wt.% and at 12 wt.% moisture.

4-6 wt%	12 wt%
-450 to -600 mV_{SCE}	-600 to -800 mV_{SCE}

3.1.2 Potentiodynamic Response of X65 Steel in Solution and in Soil

Representative polarization responses of X65 steel in modified-NS4 solution and in 0.1 M NaCl are given in Figure 3.2. More experimental polarization curves are provided in Appendix A. Figure 3.3 shows a graphical representation of some of the parameters that can be obtained from the polarization plots. These include the corrosion potential, E_{corr}, corrosion current density, i_{corr}, the anodic tafel slope, b_a, the hydrogen evolution tafel slope, b_H, and the transport-limited current density of oxygen reduction (i_{lim}). These parameters have been calculated from the curves in Figure 3.2 and are tabulated in Table 3.3.

According to Figure 3.2 the current-potential response of steel in 0.1 M NaCl is similar to that in modified-NS4 but has a slightly more positive OCP of approximately -600 mV_{SCE} compared to -680 mV_{SCE} in modified-NS4. The anodic tafel slope, hydrogen tafel slope, and transport-limited current densities are similar in these two solutions. In both modified-NS4 and in NaCl solution, there are two clearly defined reduction regimes: the transport-limited oxygen reduction reaction from E_{corr} to about -1000 mV_{SCE} and the hydrogen evolution reaction line at potentials more negative than -1000 mV_{SCE}. In oxygenated solution the corrosion current density, i_{corr}, of steel is usually controlled by the transport-limited current density of oxygen reduction, i_{lim}. This occurs because the concentration of oxygen at the steel surface is controlled by the diffusion of dissolved oxygen. In such situations, i_{corr} is equal to i_{lim}. i_{corr} of steel in modified-NS4 is larger than in 0.1 M

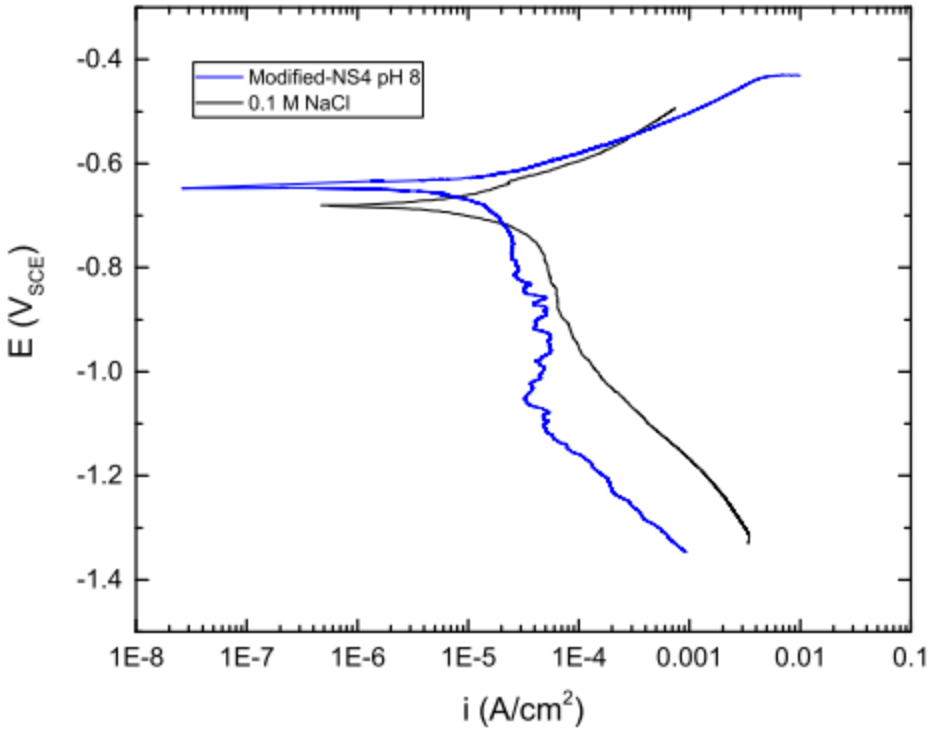

Figure 3.2: Polarization curve for X65 steel in a modified-NS4 solution and in 0.1 M NaCl.

NaCl; 3×10^{-5} A/cm^2 in modified-NS4 compared to 1×10^{-5} A/cm^2 in 0.1 M NaCl.

The Tafel slope for the oxygen reduction reaction cannot be measured experimentally in this system since it is obscured by the anodic response of the steel and only the diffusion-limited region of the oxygen reduction reaction can be measured. The cathodic tafel slopes given in Table 3.3 are therefore only estimates. But for the purposes of corrosion current density calculations according to the Stern-Geary relationship, the cathodic tafel slope of a diffusion-controlled cathodic process can be considered equal to infinity, $|b_c| = \infty$ [65].

Table 3.3 also includes parameters calculated from the polarization responses of steel in other environments: sandy clay soil and modified-NS4 adjusted to an acidic and basic pH of 4 and 12. Representative polarization plots for steel in these solutions are given in Figures 3.4 and 3 .5.

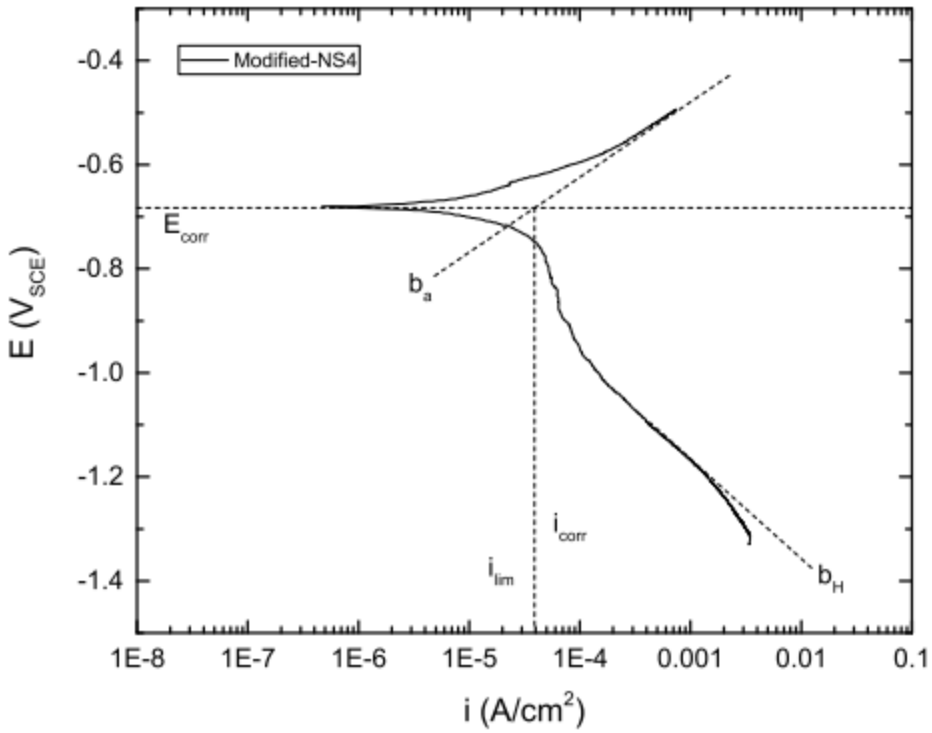

Figure 3.3: Polarization curve for X65 steel in a modified-NS4 solution with labels for the determination of anodic and cathodic tafel slopes, E_{corr}, i_{corr}, and oxygen reduction limited current density (i_{lim}).

Table 3.3: Electrochemical parameters obtained from polarization plots (Figures 3.2, 3.4, 3.5).

	Modified-NS4	0.1 M NaCl	Sandy Clay	NS4, pH 4	NS4, pH 12
E_{corr} (mV_{SCE})	-680	-620	-600	-630	-570
i_{corr} (A/cm^2)	3×10^{-5}	1×10^{-5}	1×10^{-7}	4×10^{-5}	2×10^{-7}
b_a (V/dec)	0.15	0.10	0.4	0.25	0.15
b_c (V/dec)	∞	∞	0.4	∞	∞
b_H (V/dec)	0.22	0.18	0.35	0.18	0.18
i_{lim} (A/cm^2)	3×10^{-4}	1×10^{-5}	—	4×10^{-5}	2×10^{-7}

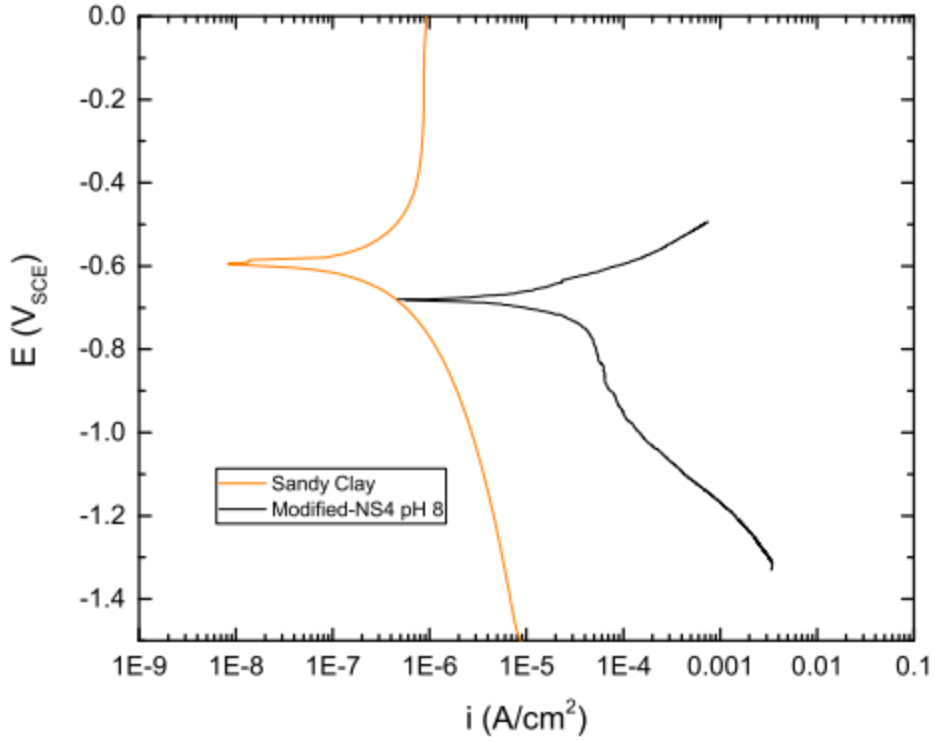

Figure 3.4: Polarization curve for X65 steel in a modified-NS4 solution and in Sandy Clay soil.

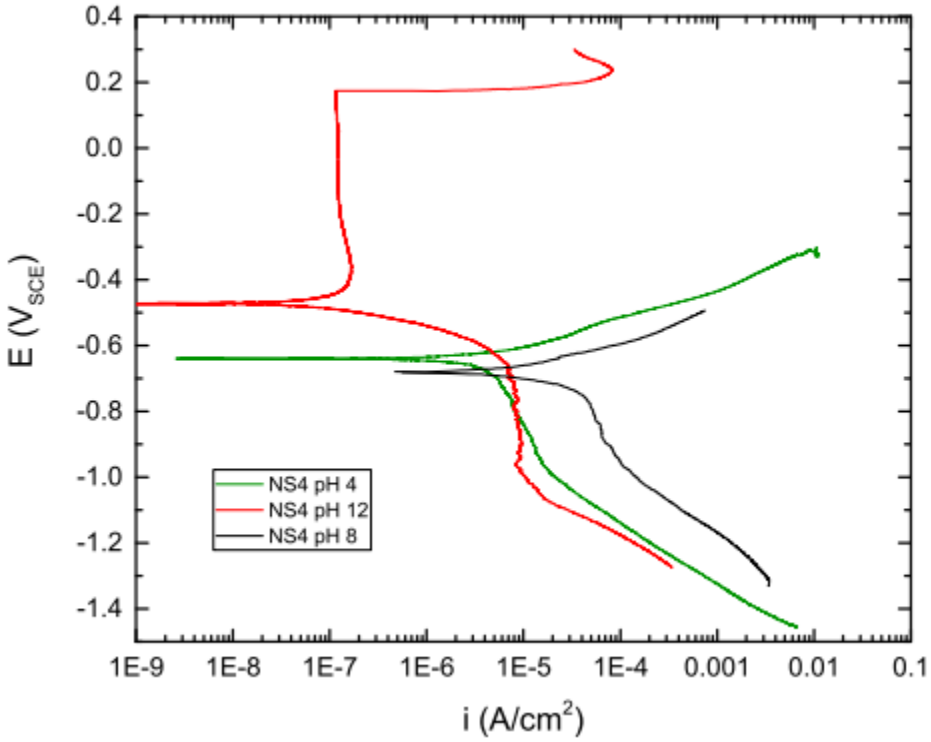

Figure 3.5: Polarization curve for X65 steel in a modified-NS4 solution at a neutral pH 8 and at a pH of 4 and 12.

The polarization curve acquired in saturated sandy clay soil is very similar to polarization curves seen by other researchers[52]. In soil, the polarization curve for steel exhibits a much lower current density at all potentials. This is likely due to restricted transport of species at the interface. There is no appearance of a transport-limited oxygen reduction region. This is probably due to almost fully anoxic conditions as the soil test in Figure 3.4 was conducted at full saturation leading to restricted oxygen transport as shown by Aachib et al.[53]. This means the cathodic region of this polarization curve is due entirely to hydrogen evolution which is also limited by transport restrictions through the soil medium. The anodic region of this curve approaches a current density limitation. One could suppose that this is due to a lack of diffusion of the Fe^{2+} ions away from the steel surface at high anodic potentials.

Soil is generally slightly alkaline (≈8 pH) but is known to be more acidic or basic in certain circumstances. The pH of the solution has a large effect on the polarization response. At a high pH of 12, the steel shows a large passive region at anodic potentials. This is due to the development of a passive oxide, likely $Fe(OH)_2$ or FeOOH, through the following mechanism[54]:

$$Fe + OH^- \rightarrow FeOH^-_{ad}$$

$$FeOH^-_{ad} \rightarrow FeOH_{ad} + Fe^-$$

$$FeOH_{ad} \rightarrow Fe(OH)_2 + e^-$$

$$Fe(OH)_2 + OH^- \rightarrow FeOOH + H_2O + e^-$$

The solid FeOOH provides passivity for the carbon steel when it is stable at high pH. However, a passive material is susceptible to pitting corrosion. The pitting potential of the steel at 12 pH can be observed at around 0.2 V vs. SCE in Figure 3.5.

The decrease in limiting current density for the oxygen reduction reaction in both pH 4 and pH 12 as compared to neutral NS4 is nearly two orders of magnitude. This observation can be explained by the difference in oxide layer composition at these pH levels. At neutral pH, magnetite (Fe_3O_4) is the most stable corrosion product expected from thermodynamic considerations (see Section 2.10). Since magnetite is conductive, it is capable of supporting the oxygen reduction reaction. The porous nature of magnetite means that it will possess a large surface area. This may mean that steel with a magnetite corrosion product layer is capable of significantly greater oxygen reduction rates. In fact, magnetite is known to support water reduction (hydrogen evolution) at high rates and this could also help to explain why the hydrogen evolution line is at much greater current densities in neutral solution[55]. Since magnetite is not thermodynamically stable at either 4 pH or 12 pH, steel in these solutions does not possess the same high-surface area corrosion product as in neutral solution and thus cannot support the same oxygen reduction rates.

3.1.3 Corrosion Rates in Soil-Simulants

Results from mass loss measurements are provided in Figure 3.6 after long-term (4-6 weeks) exposure to alternating current at various DC potentials in either modified-NS4 solution or M NaCl for some of the high current density samples. The data indicate three trends:

- With or without CP, the corrosion rate of steel increases as the magnitude of i_{AC} increases.
- With CP, the corrosion rate of steel does not exceed 1 mpy and is thus adequately protected from AC corrosion below 600 A/m^2.
- More negative CP potentials decrease corrosion rates at all magnitudes of i_{AC}.

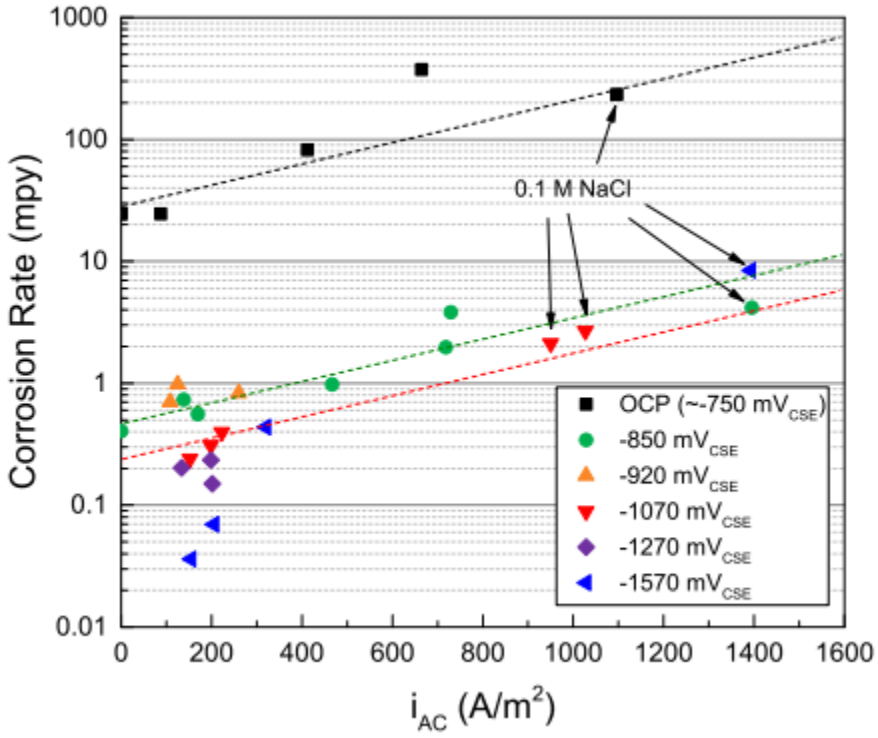

Figure 3.6: Corrosion rates from mass loss tests in a modified NS4 soil-simulant (0.1 M NaCl for high current densities) of samples at various DC potentials as a function of i_{AC}.

The first trend is most salient in the tests at the standard CP potential, -850 mV_{CSE} shown by the green dots on Figure 3.6. The corrosion rate with zero i_{AC} is 0.4 mpy. As i_{AC} increases, so does the corrosion rate. At around 600 A/m^2, the corrosion rate begins to exceed 1 mpy which is considered a benchmark for proper cathodic protection[56]. The corrosion rate continues to increase at greater i_{AC} reaching several mpy at the largest i_{AC}. Tests at a CP potential of -1070 mV_{CSE} (red

triangles) show the same trend with corrosion rates increasing as i_{AC} increases. Likewise with unprotected samples held at their OCP (black squares). Dashed lines on Figure 3.6 indicate an approximate trend line for -850 mV_{CSE}, -1070 mV_{CSE}, and no CP conditions. This trend is less visible with samples at other CP potentials due to a lack of data, but no apparent deviations can be observed.

While AC does increase the corrosion rate of cathodically protected steel, rates are less than the corrosion rate of freely corroding steel (≈10-25 mpy) at all current densities tested. When comparing the corrosion rates of unprotected samples to protected samples, the difference is large. Corrosion rates on unprotected samples can be as high as 250 mpy when AC is applied while the largest corrosion rate measured on protected samples (-850 mV_{CSE}) was only around 10 mpy at an extremely large i_{AC} of 1500 A/m^2. As previously stated, a benchmark for proper cathodic protection and corrosion control of buried steel structures is to maintain corrosion rates below 1 mpy[56]. According to Figure 3.6, when cathodically protected, AC does not appreciably enhance corrosion rates above this level until around 600 A/m^2. AC has an extremely detrimental effect on unprotected steel. When not cathodically protected, steel greatly exceeds the 1 mpy benchmark and AC further exacerbates this dangerous corrosion condition. It is also evident that CP is more protective at more negative potentials. This is most visible in the 0-300 A/m^2 i_{AC} range in Figure 3.6. Samples held at a more negative CP potential showed lower corrosion rates at almost all levels of i_{AC}. Even at very high i_{AC}s, the corrosion rates of cathodically protected steel do not exceed those of unprotected steel with no AC. The data points for -920 mV_{CSE} seem to show a reversal of this trend, but it is likely that measurement error is larger in this low corrosion rate range. Likewise for the data points at 1500 A/m^2, but this may be due to experimental error as well.

All experiments in Figure 3.6 were controlled potentiostatically so that the applied DC and AC potentials were constant for each experiment. This meant that the i_{DC} and i_{AC} would vary throughout the experiment, usually with i_{AC} increasing consistently by about 20% and i_{DC} decreasing to a stable value within a few days. As an example of the time-varying i_{DC}, Figure 3.7 shows i_{DC} on a sample with a CP potential of -850 mV_{CSE} and i_{AC} of 700 A/m^2. Reported i_{DC} data of samples used an estimate of the stable long-term value of i_{DC}. The reported value of i_{AC} in Figure 3.6 is an average of measurements taken every few days using an ammeter in series with the sample.

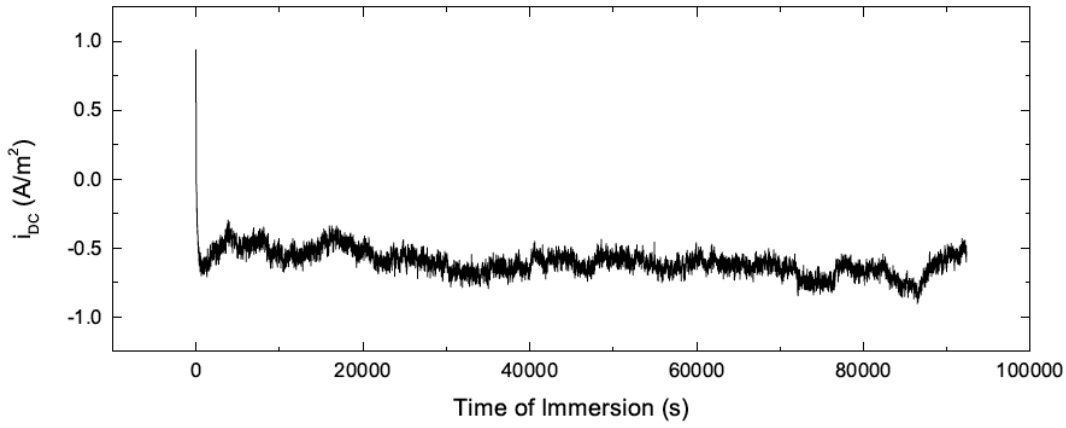

Figure 3.7: CP current, i_{DC}, during 24 hours of an AC corrosion mass loss experiment. CP potential = -850 mV_{CSE}. i_{AC} = 700 A/m^2.

3.1.4 The Relationship Between DC Current Density and AC corrosion Rate

The i_{DC} for each sample was not only dependent on the E_{DC} but also on the i_{AC}. Through asymmetric faradaic current generation, i_{AC} is capable of inducing changes in the time-averaged current density (i_{DC}). Figure 3.8 shows a plot of i_{DC} vs. i_{AC} for several samples along with the estimated i_{DC} at zero i_{DC} based on polarization curves for steel in modified-NS4. i_{DC} was not collected for every mass loss sample in Figure 3.6 and Figure 3.8 does not include data from field measurements since i_{DC} and i_{AC} values were generally too low to see any kind of trend. The trend from Figure 3.8 is that a more negative E_{DC} will increase the $-i_{DC}$ and greater i_{AC} will change i_{DC} for any E_{DC}. In most cases, i_{AC} will cause an increase in $-i_{DC}$ although i_{AC} can also induce the generation of positive i_{DC} as seen by samples held at their OCP.

It has often been stated that i_{DC} is a critical factor in consideration of the rates of AC corrosion. Figure 3.9 gives the corrosion rate of mass loss specimens as a function of the average i_{DC}. From these data, the corrosion rate seems to increase as the i_{DC} increases. This is a spurious correlation and can lead to a misunderstanding of the mechanism of AC corrosion. According to the electrochemical model, it is not that the corrosion rate is a function of i_{DC}, but that both i_{DC} and corrosion rate are functions of i_{AC}. Increasing i_{AC}, at any CP potential, will increase corrosion rate and also change the i_{DC} and make it appear as if corrosion rate were a function of i_{DC}. In this case, it is incorrect to think that decreasing $-i_{DC}$ (by decreasing CP current) will decrease the corrosion rate.

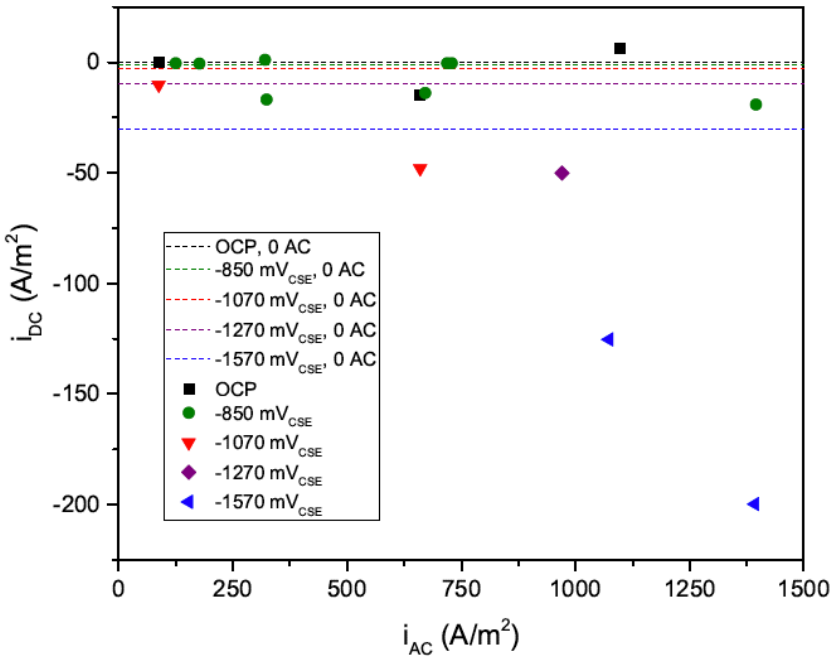

Figure 3.8: Average i_{DC} as a function of average i_{AC} during long-term mass loss experiments in modified-NS4 at different CP potentials. Lines indicate the i_{DC} expected from E_{DC} at zero i_{AC}.

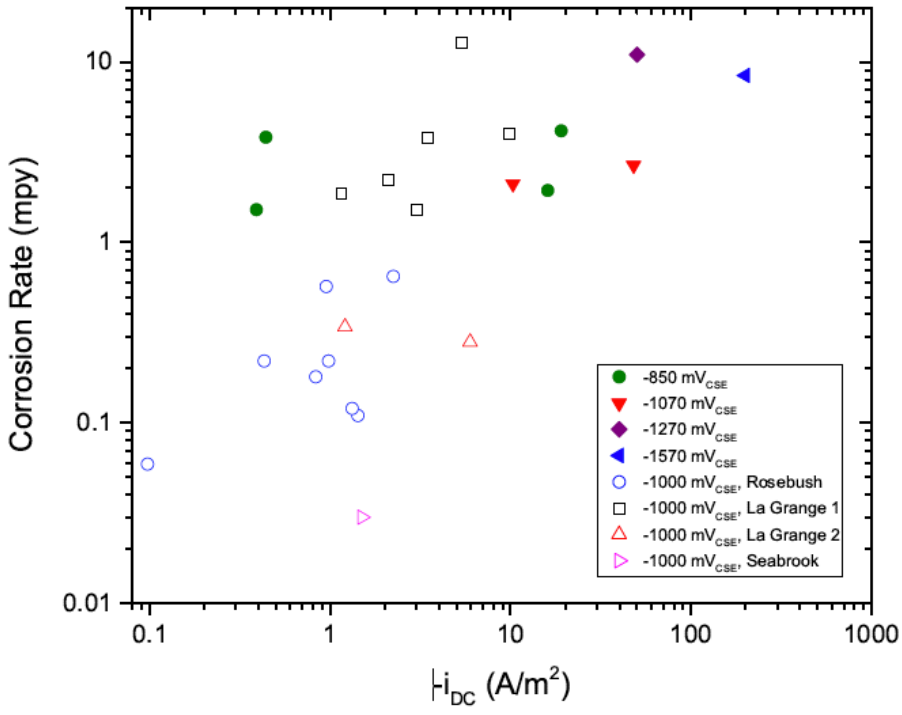

Figure 3.9: Corrosion rate as a function of i_{DC} for laboratory and field samples.

Another way to visualize the combined effect of i_{DC} and i_{DC} on corrosion rate is a bubble plot. Figures 3.10 and 3.11 show bubble plots for long-term mass loss tests where corrosion rates are a function of the bubble size and data is plotted as i_{DC} vs i_{AC}. These data do not indicate any apparent correlation between i_{DC} and corrosion rate. Since i_{DC} is a complex function of both cathodic protection potential as i_{AC}, there is no simple relationship between i_{DC} and corrosion rate. In contrast to the findings of many researchers, these data do not imply that there is any risk of greater AC corrosion at higher i_{DC}. The most reliable predictor of corrosion rates is the cathodic protection potential in combination with i_{AC} as shown by Figures 3.6 and 3.24.

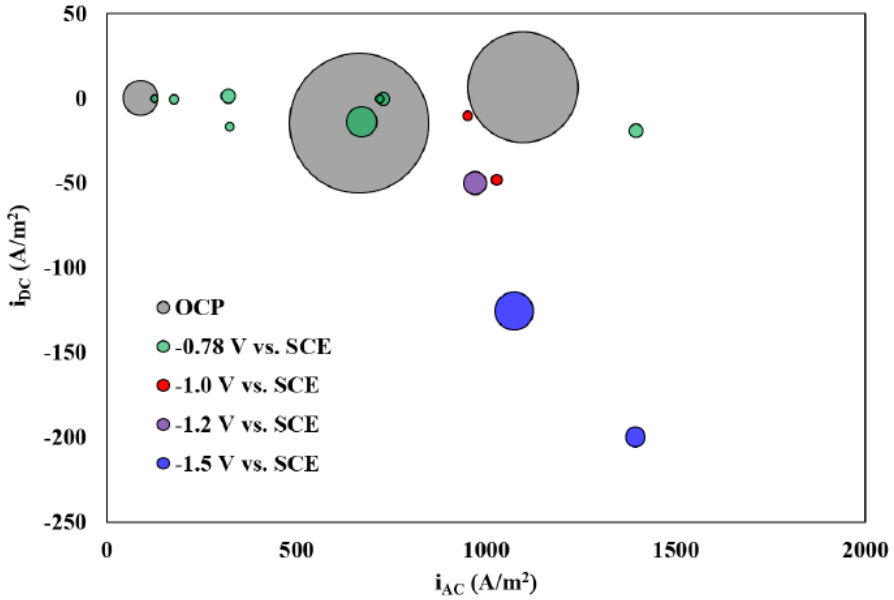

Figure 3.10: Corrosion rates (bubble size) and iDC vs. iAC for samples in long-term laboratory mass loss tests. Largest bubble corresponds to a corrosion rate of about 375 mpy.

Besides using i_{AC} or i_{DC} alone as indicators of susceptibility in AC corrosion, some have instead attempted to use the ratio of i_{AC} to i_{DC}. In fact, the European technical specification CEN/TS 15280:2006 specifies AC corrosion likelihood as a function of the ratio of i_{AC} to i_{DC} with the following risk levels [57]:

- $i_{AC}/i_{DC} < 5$: low corrosion likelihood
- $5 < i_{AC}/i_{DC} < 10$: further investigation necessary
- $i_{AC}/i_{DC} > 10$: corrosion is likely and mitigation should be pursued

The tabulation of susceptibility as a function of the i_{AC}/i_{DC} ratio can be stated another way: an increase in i_{AC} with a constant i_{DC} or a decrease in i_{DC} at a constant i_{AC} will both increase this ratio and lead to greater corrosion susceptibility.

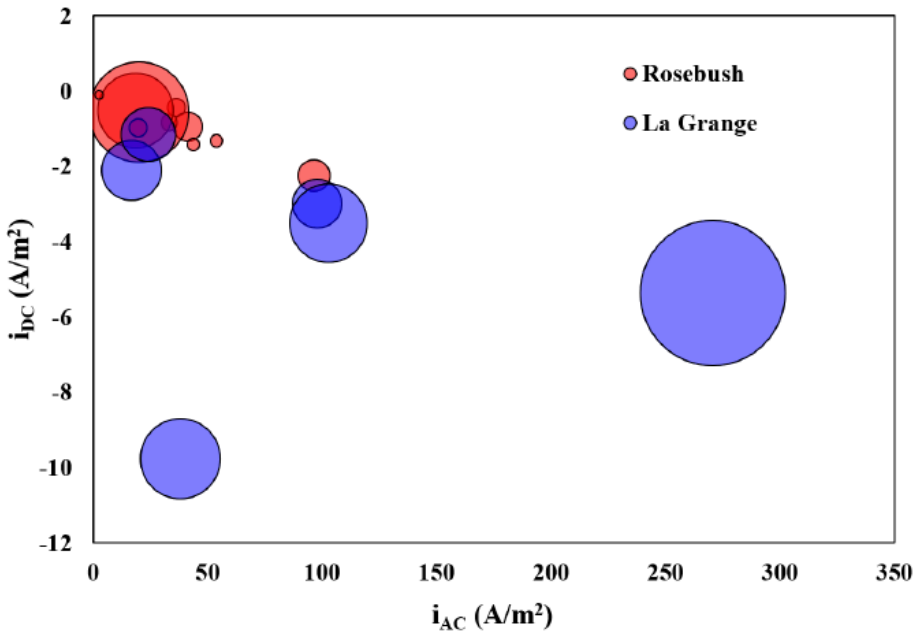

Figure 3.11: Corrosion rates (bubble size) and iDC vs. iAC for samples in long-term mass loss field tests. Largest bubble corresponds to a corrosion rate of about 13 mpy.

To investigate the validity of this ratio in assessing AC corrosion risk, Figure 3.12 shows corrosion rates as a function of the i_{AC}/i_{DC} ratio for samples held at various CP potentials. Samples held at their OCP could not be included because many of them displayed a positive i_{DC}. There is no discernible trend in these data. Samples with an i_{AC}/i_{DC} ratio greater than 10 do not always have an increased corrosion rate while many samples with a ratio below 10 do show high corrosion rates. But it is difficult to make any statements with respect to the European standard for i_{AC}/i_{DC} ratios due to a lack of data with an i_{AC}/i_{DC} ratio below 5.

Figure 3.13 shows the effect that experimental duration has on the mass loss of steel. Steel at the cathodic protection potential was exposed to either 130 A/m^2 or 0 A/m^2 of i_{AC} for various times. Extremely large corrosion rates at short experiment times quickly decrease to a lower steady-state corrosion rate at long times. Presumably, this is due to the buildup of corrosion product and the eventual decrease in faradaic oxidation as the magnetite begins to present a large capacitance and capacitive current accounts for a greater fraction of the i_{AC}.

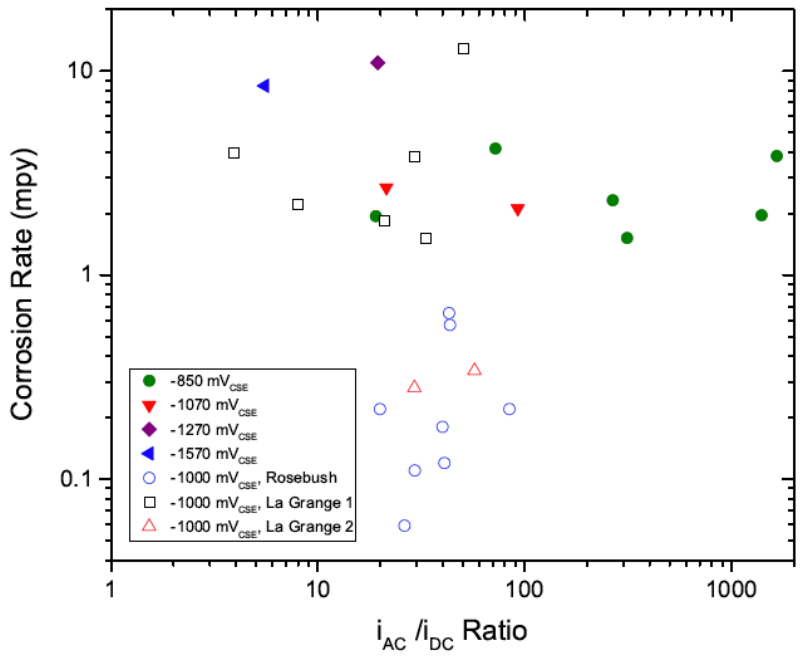

Figure 3.12: Corrosion rate as a function of the i_{AC}/i_{DC} ratio for samples held at a CP potential of -780 mV_{SCE}.

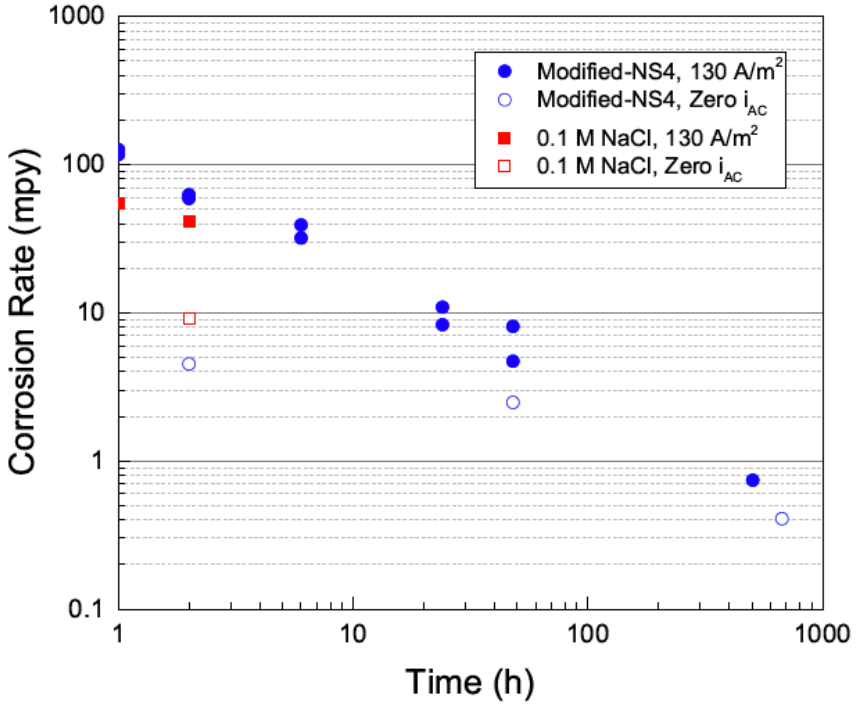

Figure 3.13: Corrosion rate as a function of time for steel electrodes in modified-NS4 and in 0.1 M NaCl with either 130 A/m^2 i_{AC} or 0 i_{AC}.

The progression of corrosion product buildup is best illustrated by the images in Figure 3.14. The sample shows buildup of both black and orange corrosion product after sitting in solution for 1 hour at its OCP (Figure 3.14b). Then, after application of CP and AC for 2 hours (Figure 3.14c), we see mostly black corrosion product form. This is Fe_3O_4, or magnetite. At this point, magnetite is not quickly oxidized to form the orange oxide Fe_2O_3 since it is still held at a cathodic potential. After a few days of CP and AC application, however, a large enough fraction of the magnetite has oxidized so that orange rust is visible in Figure 3.14d.

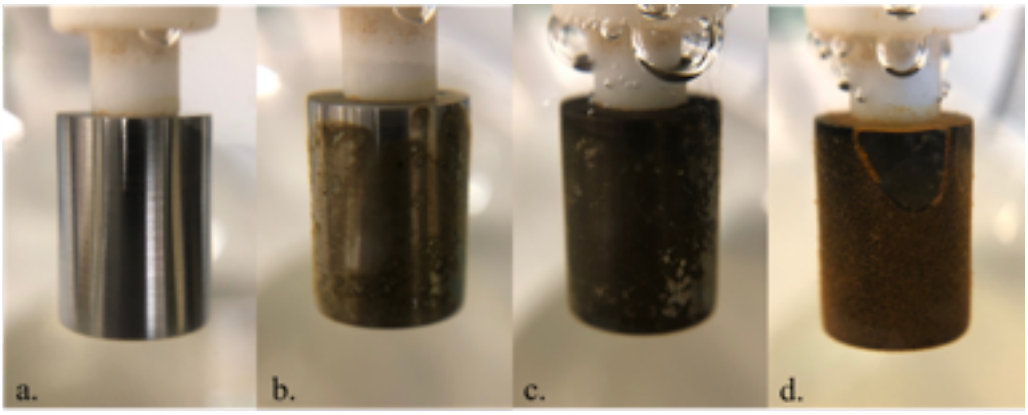

Figure 3.14: Image of working electrode samples in a modified-NS4 solution at first immersion (a), after 1 hour of OCP (b), 2 hours after application of CP and AC (c), and after 3 days of AC application (d).

Table 3.4 reports observations made during long-term corrosion rate tests. These observations support the prevailing theory that magnetite forms as an inner layer on the steel surface. More positive potentials or greater i_{AC} increase the duration of positive potentials on the steel which increases both oxidation to magnetite and oxidation of magnetite to Fe_2O_3 (orange rust). Therefore, more positive potentials and greater i_{AC} show more Fe_2O_3 development. For comparison with 3.14, an image of an electrode after the application of 600 A/m^2 of AC and -1000 mV_{SCE} CP for 3 days is shown in Figure 3.15. Despite the large i_{AC}, the sample did not develop the Fe_2O_3 because it was held at a sufficiently negative CP potential. After a longer time, it is expected that this sample will develop some Fe_2O_3.

Table 3.4: Descriptions of the corrosion product from long term mass loss at different levels of CP and AC.

	Low AC (<100 A/m^2)	Medium AC (100-400 A/m^2)	High AC (>400 A/m^2)
-850 mV$_{CSE}$	black with orange outer layer	black with orange outer layer	black with significant orange rust in solution
-1070 mV$_{CSE}$	black	black	black with orange outer layer
-1270 mV$_{CSE}$	black	black	black
-1570 mV$_{CSE}$	black only at edges	black	black

Figure 3.15: Image of an electrode after 3 days of -1000 mV$_{SCE}$ CP and 600 A/m^2 of AC.

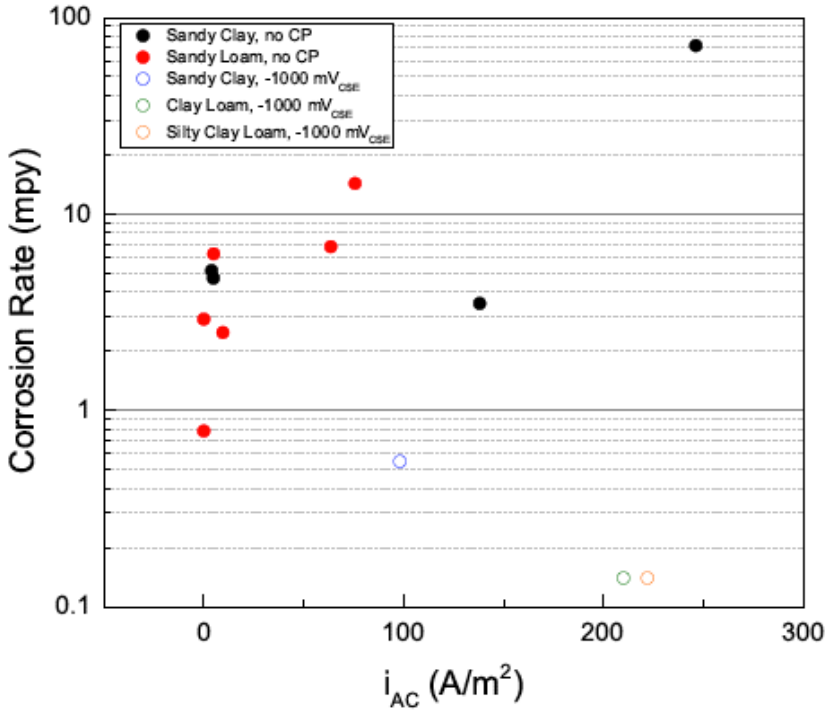

Figure 3.16: Corrosion rates vs. i_{AC} for steel in artificial soils with and without applied CP.

Figure 3.16 gives the corrosion rates of steel specimens in artificial soils under the influence of AC. Tests without CP applied were conducted using a variac to apply the AC instead of a potentiostat. This was done to overcome current limitations in high-resistivity soil. These data do not show any noticeable differences between soil types. But they do further demonstrate the effectiveness of CP.

As pointed earlier, in order to achieve large magnitude i_{AC} in laboratory tests, the exposed area of cylindrical steel samples was reduced with electroplater's tape. While this increased the total ohmic resistance in the cell, it decreased the normalized ohmic resistance. This is because the grounding resistance for a flat disk (approximated by the small reduced area on the electrode) is a function of the radius, not the area. The increase in ohmic resistance is linearly proportional to the decrease in radius while the decrease in area scales with the square of the radius.

In order to achieve high AC current densities on field coupons, the same strategy was used. The exposed areas of cylindrical steel samples were reduced by taping off the sides of the electrodes and leaving only the bottom exposed.

Table 3.5: Soil types and resistivities (determined by 3-point Wenner method) at the three field-testing locations.

Location	Soil Type	Resistivity (Ω-cm)
Rosebush, MI	Sandy Clay Loam	5500
La Grange, TX	Sand and Clay Loam	1400
Seabrook, TX	Clay	1500

3.1.4 Corrosion Rates from Field Testing

The corrosion rate results obtained from mass loss experiments of pipeline-bonded coupons on two AC-capable test pipeline systems and an in-service pipeline are shown in Figure 3.17. The corrosion rates from field experiments on a Mg anode system are in line with corrosion rates obtained in the laboratory. That is, greater AC leads to greater corrosion rates, but the corrosion rates, even to an i_{AC} of 100 A/m^2 are still below 1 mpy. It can be concluded that the Mg anode CP system was effective in mitigating corrosion due to AC at these current densities over the range tested.

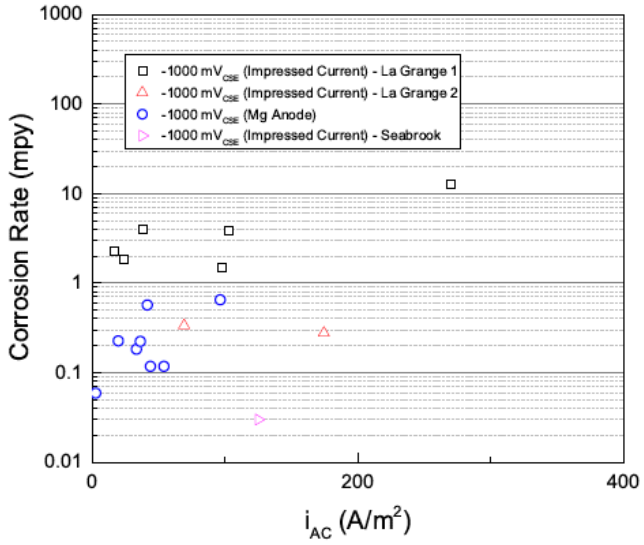

Figure 3.17: Corrosion rates as a function of i_{AC} from mass loss tests of pipeline-bonded coupons on two CP test systems and an in-service pipeline (Seabrook).

As for samples bonded to a pipeline using an impressed current rectifier, there are two different groupings. The first grouping, referred to as" La Grange 1" came from the use of the La Grange test system in 2018. These data show an overall greater corrosion rate at all i_{AC} compared to the Mg anode system. The data in the second grouping," La Grange 2", came from tests in 2019. These samples experienced low corrosion rates in line with the Mg anode system. The mass loss sample on the Seabrook pipeline also experience a low corrosion rate.

It is difficult to say why a difference in corrosion rate is observed between the two locations. It could be that the soil properties of the Texas location are more conducive to corrosion than the Rosebush location or it could be that the impressed current rectifier is less effective in providing CP than a passive anode system. But the difference in corrosion rate can also be explained by examining the voltage and current density data obtained on the two systems. Figure 3.18 shows data for a sample on the impressed current system while Figure 3.19 shows data on the Mg anode system. At the early test times for the Texas site (1st week in Figure 3.18), the system experienced an off potential of -700 mV_{CSE} compared to the more negative average of around -1000 mV_{CSE}, indicating a period of insufficient CP. Although the duration of this potential anomaly seems short relative to the total duration of the experiment, considering the non-linear relationship of corrosion rates with respect to DC potential, it is likely that these samples experienced a greatly increased corrosion rate for this period of time which adversely affected the final measurement. The data for the Mg anode system do not indicate any periods of insufficient CP during the test (There is an absence of data for a period these tests but there is no reason to believe the system was malfunctioning during this period.).

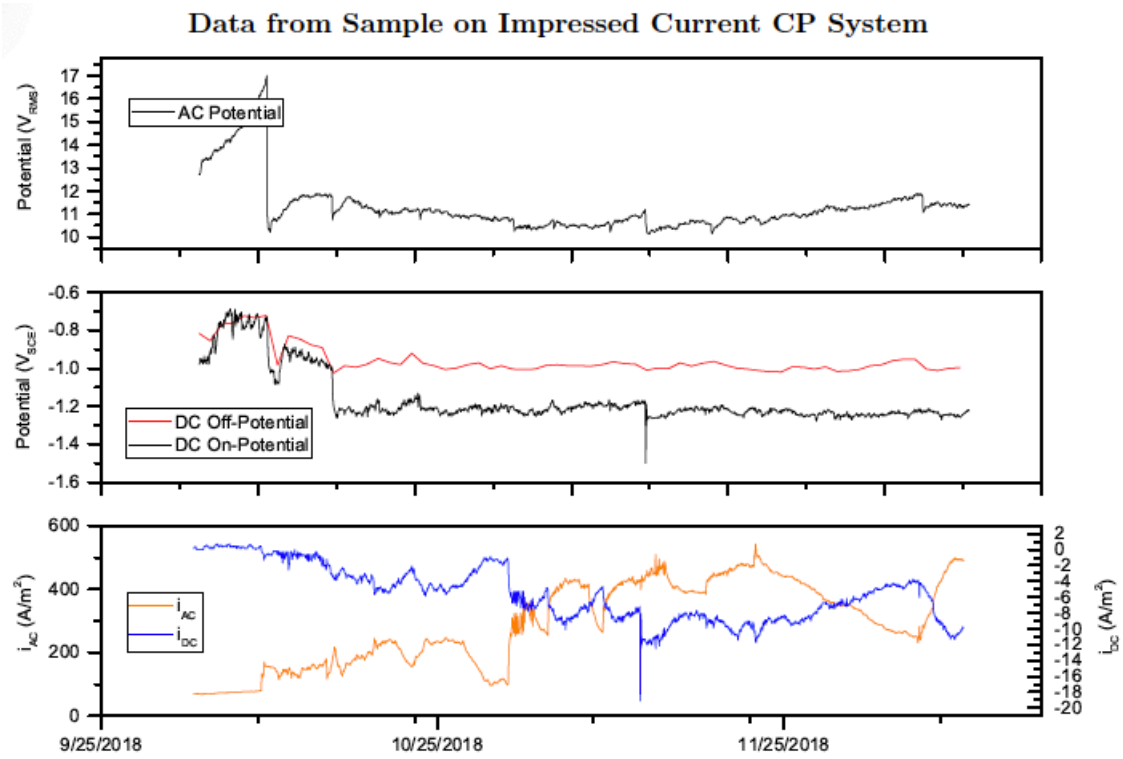

Figure 3.18: AC Potentials (top), DC on and off-potentials (middle) and i_{AC} and i_{DC} (bottom) for a 5 cm^2 sample buried for 2 months at the La Grange facility in 2018.

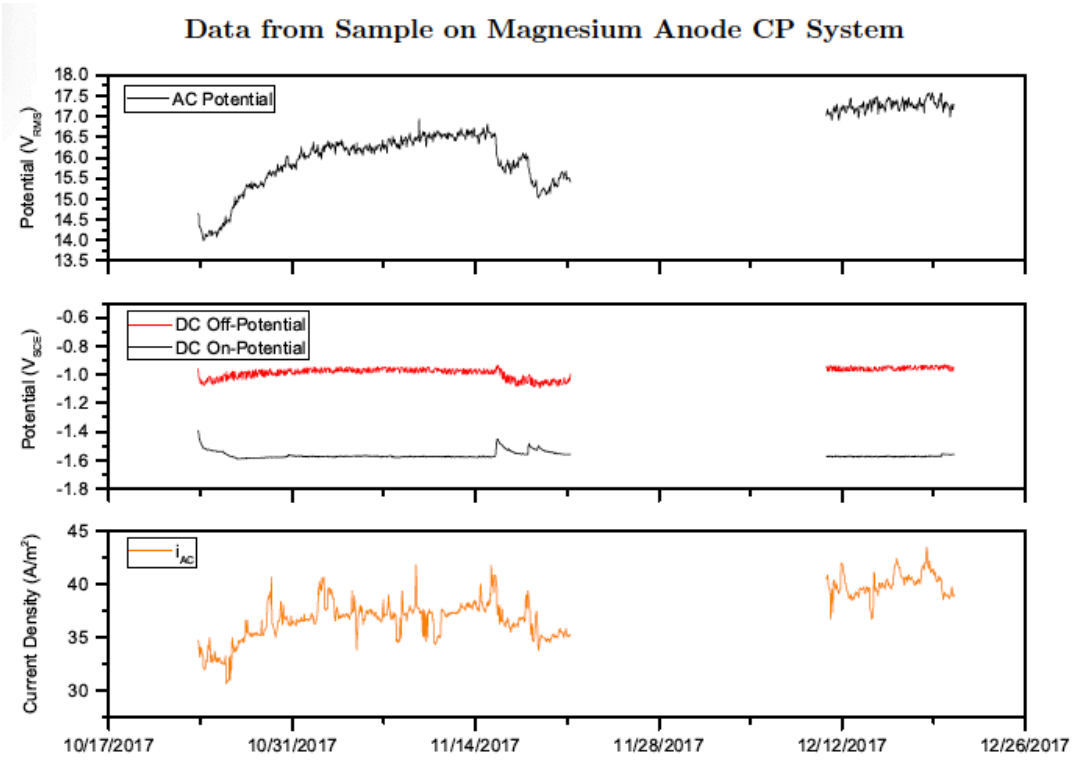

Figure 3.19: AC Potentials (top), DC on and off-potentials (middle) and i_{AC} (bottom) for a 10 cm^2 sample buried for two months at the Rosebush facility in 2017.

Figures 3.20 and 3.21 show metal loss and corrosion rate data for ER probes used at the La Grange test facility and the Seabrook pipeline, respectively. The metal loss data is a converted electrical resistance value proportional to the thickness of the probe These data indicate that no metal is lost over the baseline value over time. The maximum resolution of these probes over the time tested is around 0.5 mpy so the corrosion rate could not have exceeded this value without showing up as a total increase in metal loss. The variability of the corrosion rate calculation is simply due to noise. A rolling average would likely provide a flat line.

Mass loss samples were prepared with the same dimensions as the ER probes as a simple verification of the ER data. These mass loss samples experienced very similar current densities as the ER probes. The corrosion rates of these mass loss samples (Seabrook mass loss sample, and La Grange Sample # 7) are less than 0.5 mpy. These low corrosion rates verify the measurements by ER probes.

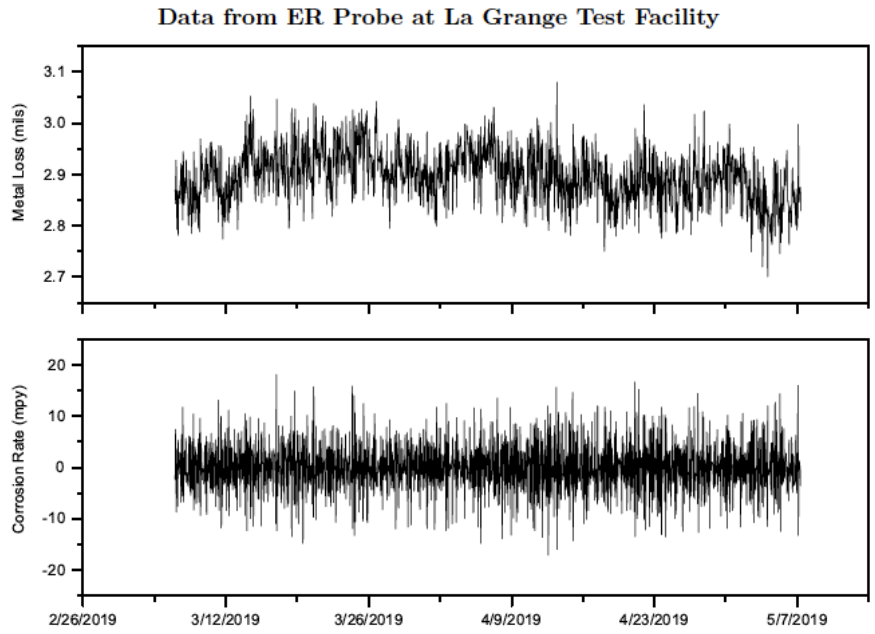

Figure 3.20: Metal loss (top) and instantaneous corrosion rate (bottom) of a cathodically protected steel ER coupon under the influence of AC at the La Grange test site. Current and voltage data for this sample is provided in Figure 5.25

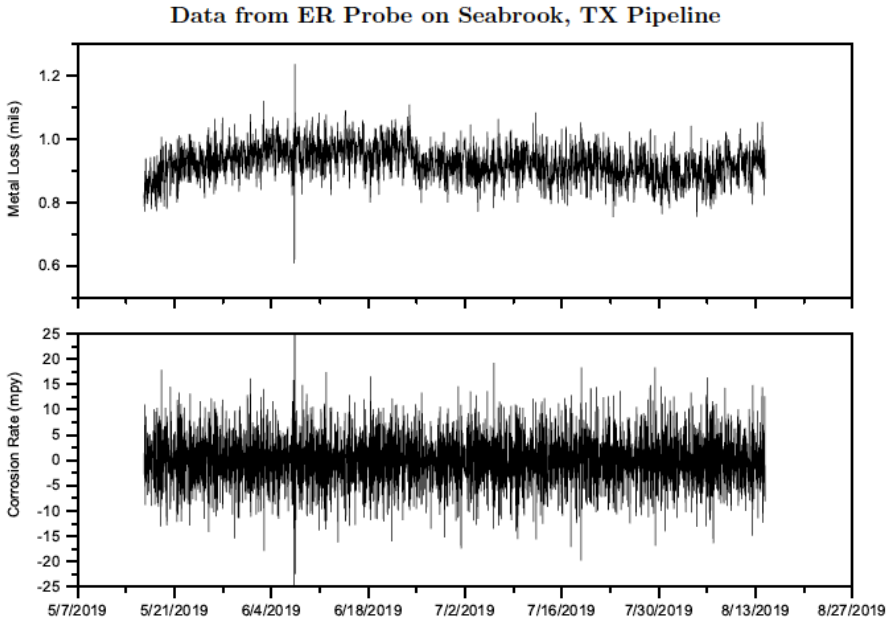

Figure 3.21: Metal loss (top) and instantaneous corrosion rate (bottom) of a steel ER coupon bonded to an in-service pipeline under the influence of AC.

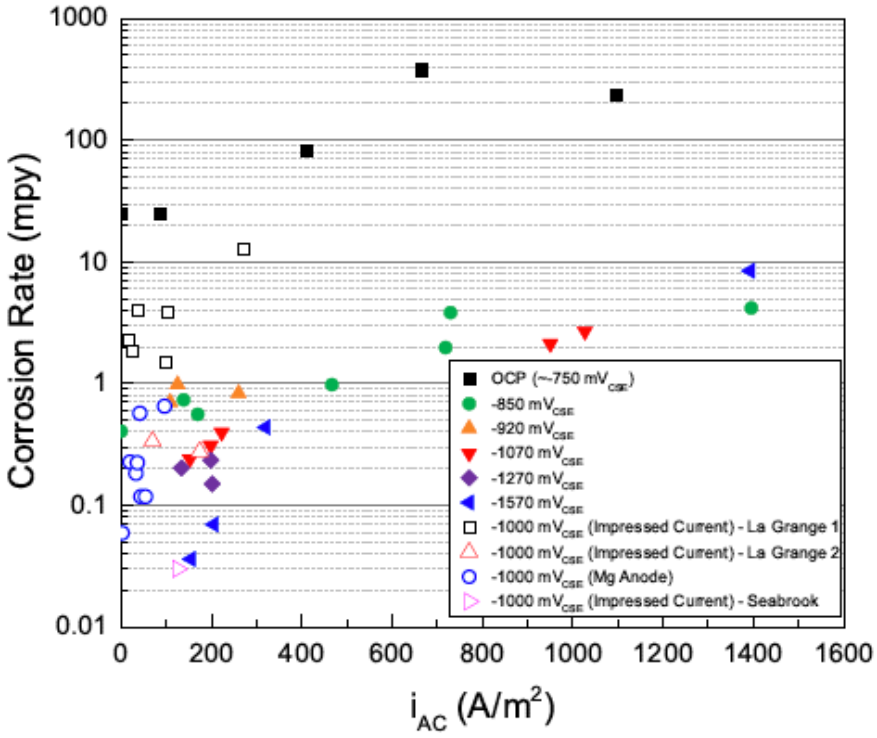

Figure 3.22: Corrosion rates as a function of i_{AC} from mass loss tests for field tests and laboratory tests in soil-simulant.

Figure 3.22 shows the corrosion rate data vs. i_{AC} for both laboratory and field tests. The corrosion rates on field samples where consistent CP can be assured are in line with those obtained on laboratory tests. As explained above, the first-round samples on the impressed current system," La Grange 1" show a larger corrosion rate than laboratory tests at any i_{AC} and this is likely due to the initial period of more positive off-potentials as seen in Figure 3.18.

3.1.5 Corrosion Morphology and Pitting

The morphology of AC corrosion on steel in soils can present in different ways. Figure 3.23a, b, and c show images of a 10 cm^2 mass loss coupon used for a test at the La Grange location after pulling samples from the ground. The sample is shown with adhered soil and other particulate in 3.23a, and then after cleaning, 3.23b, and after using Clarke's solution, 3.23c. The corrosion rate for this sample was very low and corrosion is nearly imperceptible from visual inspection.

(a) *(b)* *(c)*

Figure 3.23: Images of Sample 1 from La Grange field tests immediately after removal (a), after cleaning adhered soil (b), and after cleaning with Clarke's solution (c).

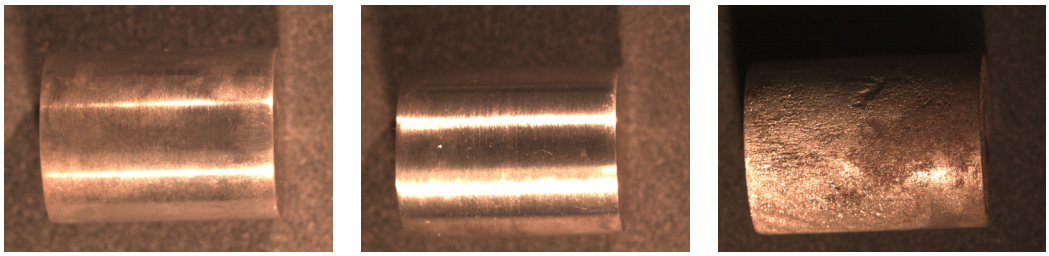

(a) *(b)* *(c)*

Figure 3.24: Image of corrosion morphology of electrode after application of 6 weeks of AC (around 200 A/m^2) at (a) -1500 mV$_{SCE}$, (b) -780 mV$_{SCE}$, and (c) at OCP.

Images of some laboratory samples after mass loss are given in Figure 3.24a, b, and c. The polishing lines can still be observed on the cathodically protected samples indicating minimal general corrosion. The sample held at its OCP during application of AC shows a more corroded surface morphology. These images exhibit the difference in corrosion between steel which is and is not cathodically protected.

The ostensible development of pitting corrosion has very often been attributed to AC. Indeed, "pits" can be observed under high corrosion rate conditions. However, this phenomenon is likely not equivalent to a bona fide pitting corrosion as it is known on passive metals. Rather, the observation of "pits" is likely just a general corrosion which is transiently localized to certain susceptible regions of the steel. In other words, there is no localized chemistry inducing auto-catalytic pitting corrosion. It may simply be that current is not always distributed evenly on the steel surface, especially under high AC conditions where areas of high current can distort the potential fields on the metal surface. This is similar to electrode edge effects.

It is also possible that mineral scaling induces similar corrosion morphology which can be mistaken for pitting. The formation of scale on the steel surface has been shown to protect the steel from AC corrosion through a decrease in activation kinetics[58]. In field tests, mineral scale accompanied by pitting was often observed on samples which did not receive adequate CP. Figures 3.25 and 3.26 show samples buried at the Rosebush, MI testing facility. During testing, the CP system was offline for a few weeks. In this time, samples received AC but not CP and experienced very high corrosion rates. These samples exhibited a severe pitting morphology. Corrosion pits were observed only underneath the adhered soil and not under the scaled sections of steel. This indicates that the scale protected the samples where it is present.

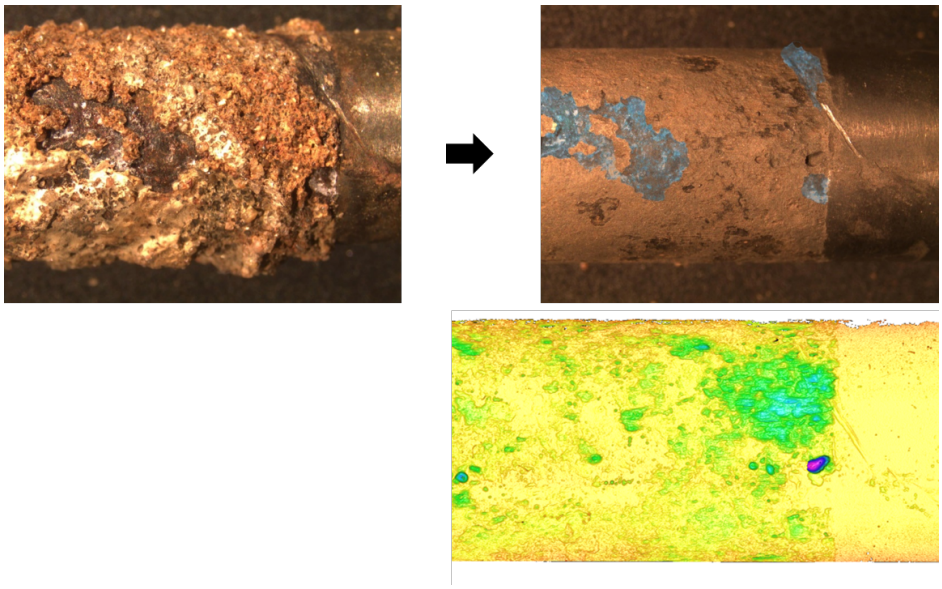

Figure 3.25: Scale and pitting morphology on steel sample subjected to AC without CP. Bottom image shows the 3D topography of the sample.

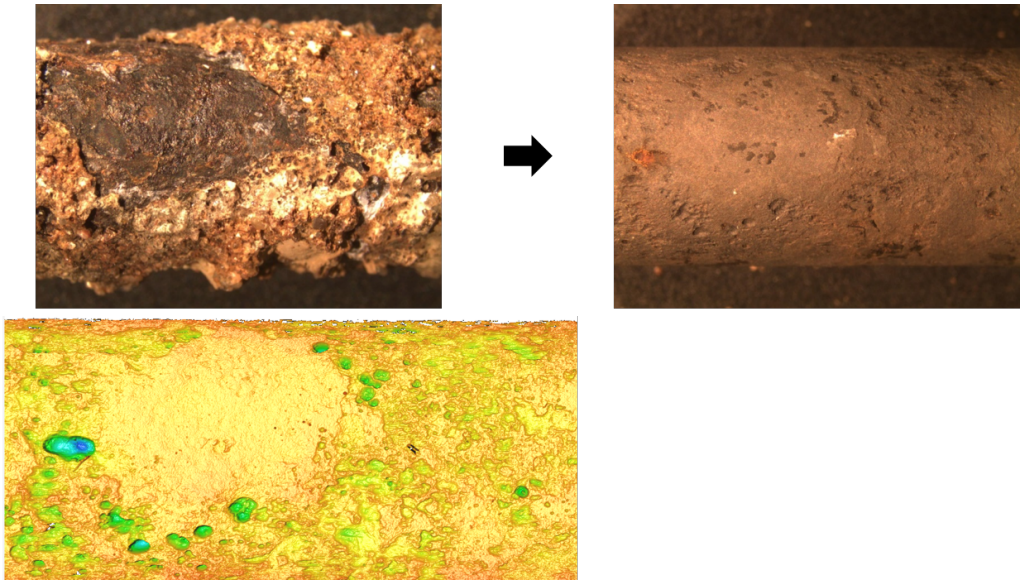

Figure 3.26: Scale and pitting morphology on steel sample subjected to AC without CP. Bottom image shows the 3D topography of the sample.

Figure 3.27 shows an image of a sample which was immersed in a normal NS4 solution (with Ca^{+} and Mg^{+}) for a few hours. After a few hours, scale was visible on certain areas of the sample, but not across the entire sample. The sample was subjected to high current density AC for a short while, then cleaned and examined. The areas of the sample which developed scale appear to show a pit-like corrosion morphology. The non-scaled areas appear as a smooth general corrosion morphology. Another example is given in Figure 3.28 after the AC corrosion of a sample with a $FeCO_3$ grown by the methods from[58]. The effect of real soils on the morphology of AC corrosion can appear similar. Field samples display a corrosion morphology which can often be mistaken for pitting corrosion for two reasons: First, it can be expected that soils possess earth alkaline cations in concentrations sufficient to produce mineral scaling through carbonate or hydroxide precipitation as well as the development of iron carbonate scale[59]. If this scaling is protective of the underlying metal but forms unevenly on the surface, then mineral scaling would produce the same sort of apparent pitting of the samples as shown in Figure 3.27. Uncovered areas of the sample will be exposed to the alternating voltages while scaled areas will be protected.

The second reason that pits might appear on steel subjected to AC in soils is that it is the heterogeneous nature of soils that specific areas of an exposed metal would experience paths of low ionic resistance while other areas may be shielded from potential fields by local soil macro-particles or drier local areas of soil. This would naturally expose specific areas of the steel to the detrimental effects of AC producing an uneven corrosion morphology, possibly appearing as pits.

This last point has implications on the measurement of AC corrosion through the use of coupons. If the current distribution is not evenly distributed, then measured i_{AC} is not correct since the current is localized to specific regions on the sample. Since the relationship between i_{AC} and corrosion rate is not linear, this can lead to a much greater local corrosion rate than would be expected from the nominal i_{AC} measurement, while the overall corrosion rate, taking into account the entire exposed surface area may not be greatly enhanced. However, in all field tests performed, the heterogeneity of current distribution has not been seen as a problem. Most samples, according to appearance, seem to have experienced homogeneous current.

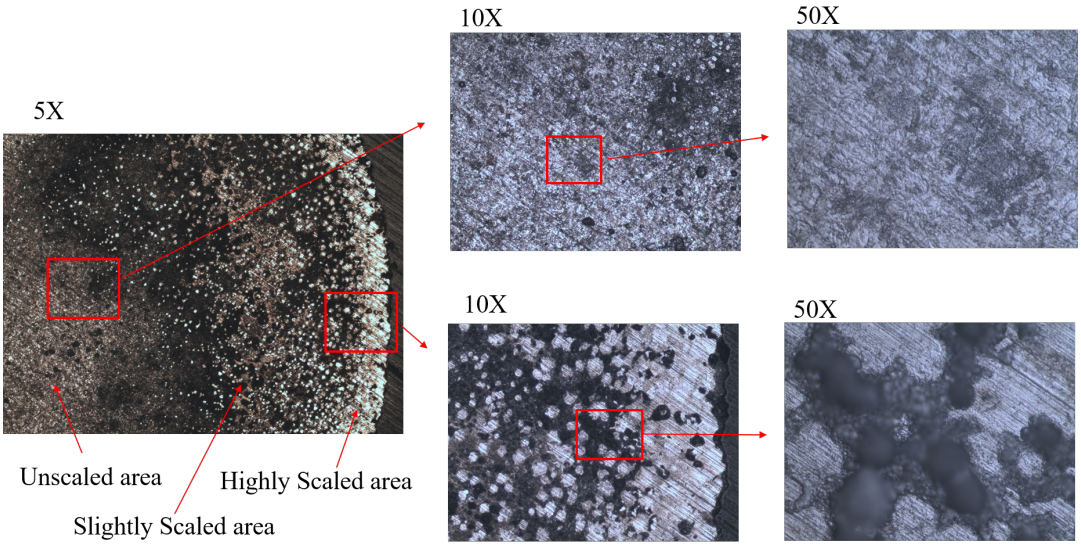

Figure 3.27: Images of the corrosion morphology of steel exposed to AC after the development of mineral scale.

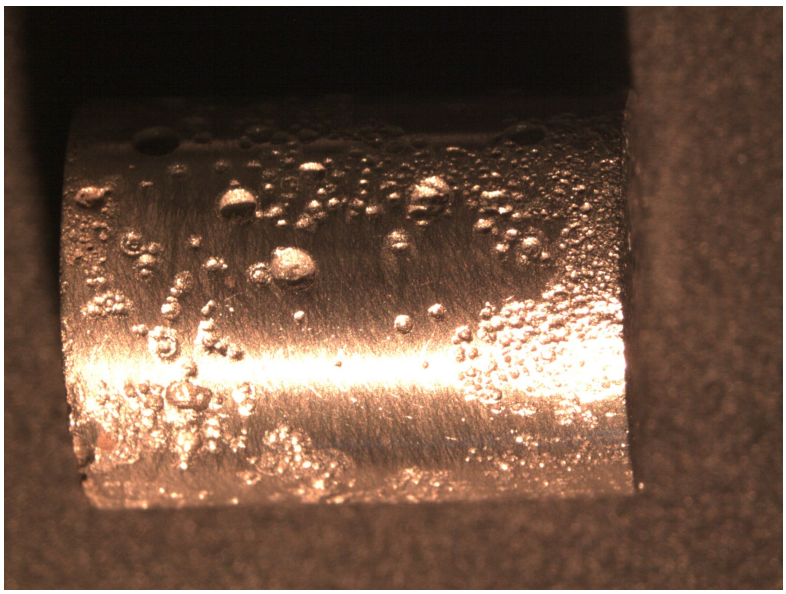

Figure 3.28: Images of the corrosion morphology of steel exposed to AC after the development of $FeCO_3$ scale.

3.2. Environmental Cracking Susceptibility

3.2.1 SCC Behavior Under Cathodic Potentials - No AC

The slow strain rate (SSR) technique was used to obtain the stress-strain curves of carbon steel 1018 in various environment. Final elongation and area reduction for each specimen were also measured after the fracture. The first SSR test was performed on carbon steel 1018 in lab air at the strain rate of 1×10^{-6} in/s. This test in an inert environment provided baseline for comparing different SSR results. The slow strain rate of 1×10^{-6} in/s is commonly used and in the range from 10^{-5} to 10^{-7} in/s in accordance with the ASTM G129 standard. The second SSR test was carried out in NS4 solution at the same rate of 1×10^{-6} in/s, with the corrosion potential monitored over time. The comparison of these two curves (Figure 3.29) showed almost identical stress-strain behavior of carbon steel 1018 in NS4 solution and in air, which suggests that the testing time may be insufficient for the corrosion mechanism to occur on the sample.

A third test was performed with a 24-h pre-corrosion before the SSR test started. The stress-strain curve with pre-corrosion showed a slight difference in the slope of the elastic region and in the strain obtained compared to that without 24-h pre-corrosion. This shows that the pre-corrosion time used before the tensile test affected the mechanical parameters of the sample to some extent, however not significantly.

Studies have shown that strain rate can significantly influence the SSR test results.[60] Parkins suggested that with high strain rates, a ductile fracture would occur before the necessary corrosion reactions occur.[60] To determine the effect of strain rate and select the optimal one for detecting the SCC susceptibility, a lower strain rate of 1×10^{-7} in/s was used in NS4 solution, and the result is shown in Figure 3.29. It was found that at a lower strain rate, the carbon steel 1018 specimen showed a significant decrease in the elongation compared to that in the inert lab air environment and also noticeable change in the elastic region. Therefore, it was concluded that a slower strain rate of 1×10^{-7} in/s is more suitable for detecting the SCC susceptibility of carbon steel in NS4 solution, compared to the commonly adopted 1×10^{-6} in/s. At this rate, it usually took 16 days to complete an SSR test, depending on the severity of the test condition (e.g, applied CP and AC potentials). In addition, a 24-h pre-corrosion period was also considered beneficial for the SCC detection in the laboratory.

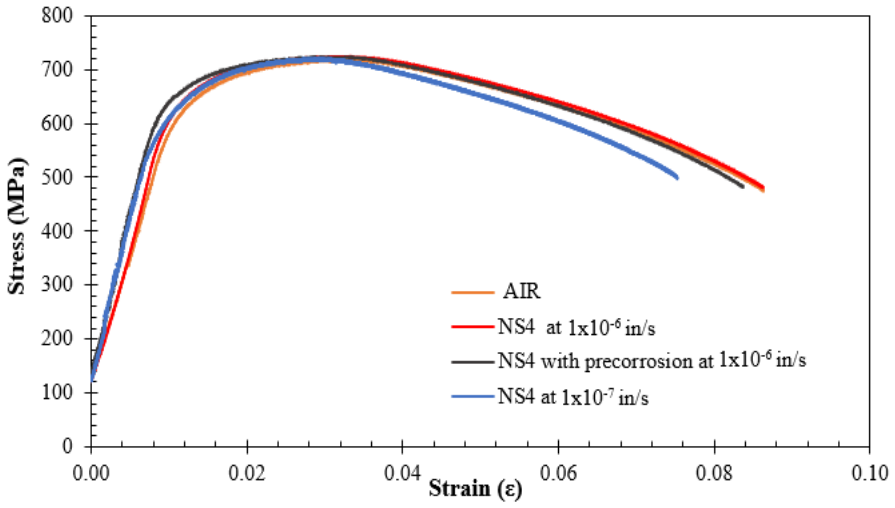

Figure 3.29. Comparison of stress-strain curves for carbon steel 1018 in different environment (lab air and NS4 solution), with different strain rates (1×10^{-6} *in/s and* 1×10^{-7} *in/s), and with and without 24-h pre-corrosion.*

It is desirable to generate a metal surface in the lab that can mimic that in the field. A long term (96 h) immersion test was performed on a cylindrical carbon steel 1018 sample (non-gauge section of an SSR specimen) in NS4 solution. The OCP trend in Figure 3.30a shows a sharp decrease from −0.48 V/SCE to −0.72 V/SCE in the first two hours of immersion and a steady state OCP of −0.74 V/SCE for the rest of the test. Images taken at different stages showed that a uniform corrosion film formed on the metal surface after 24 hours of immersion. As the immersion time increased, more corrosion product formed on the surface and the accumulation of corrosion products at the bottom of the cell also increased (Figure 3.30 d to g). Based on the OCP trend and visual observations, it was determined that a 24-h pre-corrosion period before SSR test was sufficient to create a uniformly corroded surface, which can represent the field condition. In addition, since the diameter of the gauge section (3.22 mm) used in the SSR tests was much smaller than the immersed sample (6.34 mm), the 24 h pre-corrosion would be enough for the formation of a uniform film of corrosion products.

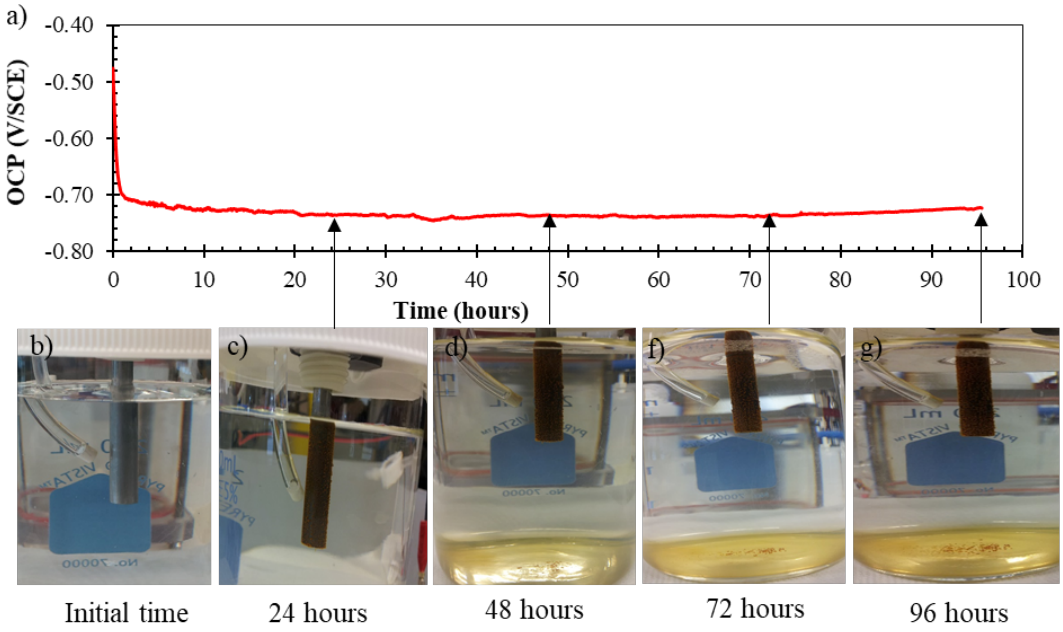

Figure 3.30. (a) Open circuit potential (OCP) evolution of the carbon steel 1018 in NS4 solution for 96-h and (b-g) images of the sample at different time.

After establishing that 24-h OCP immersion was needed to create a pre-corroded surface, SSR tests were carried out to study the effect of different CP potentials (i.e., −0.77, −0.85, and −1.12 V/SCE) on the SCC susceptibility without the AC influence. A 24-h pre-charging period was added after the pre-corrosion period and before the SSR test. This was done so that the specimen reached steady state under the applied cathodic potential before the SSR test. Figure 3.31 shows the effect of the CP potentials on the ductility and mechanical properties of the carbon steel 1018 at the strain rate of 1×10^{-7} in/s. Two tests were added for comparison, one in NS4 solution at OCP and the other baseline test in air, which exhibited the highest tensile strength and the largest elongation. The ultimate tensile strength (UTS) and yield strength (YS) of the sample under −1.12 V/SCE were close to the values of the samples in air and NS4 at OCP. However, the elongation was the smallest. As shown in Figure 3.31, the SCC susceptibility increased as the electrochemical cathodic potential shifted to more negative value. More loss of ductility was observed when lower cathodic potentials were applied.

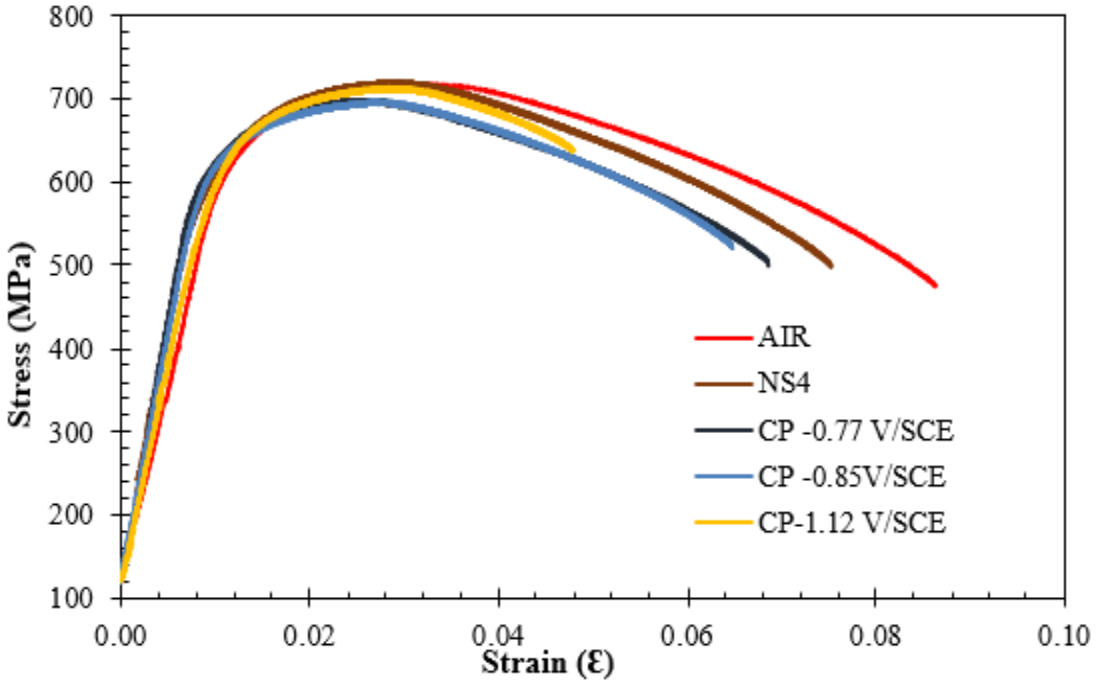

Figure 3.31. Comparison of stress-strain curves of carbon steel 1018 in NS4 solution with different CP potentials, −0.77, −0.85, and −1.12 V/SCE. They are compared with the baseline results at OCP (NS4) and in air.

The OCP of the steel was around −0.70 V/SCE, located in the domain overlapped with both corrosion ($Fe \rightarrow Fe^{2+} + 2e^{-}$) and HER. This suggests that the loss of ductility in the sample under −0.77 V/SCE may be due to the simultaneous actions of anodic dissolution and HER. Suppression of the anodic dissolution is expected at lower cathodic potential, and the enhanced cathodic reaction (i.e., HER) on the surface could cause the embrittlement and acceleration of cracking in the sample. Researchers have shown that the absorption of hydrogen atoms into the steel lattice and especially at the crack tip can promote plastic deformation and accelerate crack growth.[61]

The current density vs. time behavior under different applied cathodic potentials during the SSR tests is shown in Figure 3.32. All three current profiles exhibited steady state with slight increase over time. More negative cathodic currents were obtained when lower cathodic potentials were applied to the samples. It can be explained by an increase in the kinetics of the cathodic reactions. The increase could accelerate the HER on the surface and, therefore, more severe embrittlement was found at lower cathodic potentials as shown in Figure 3.32.

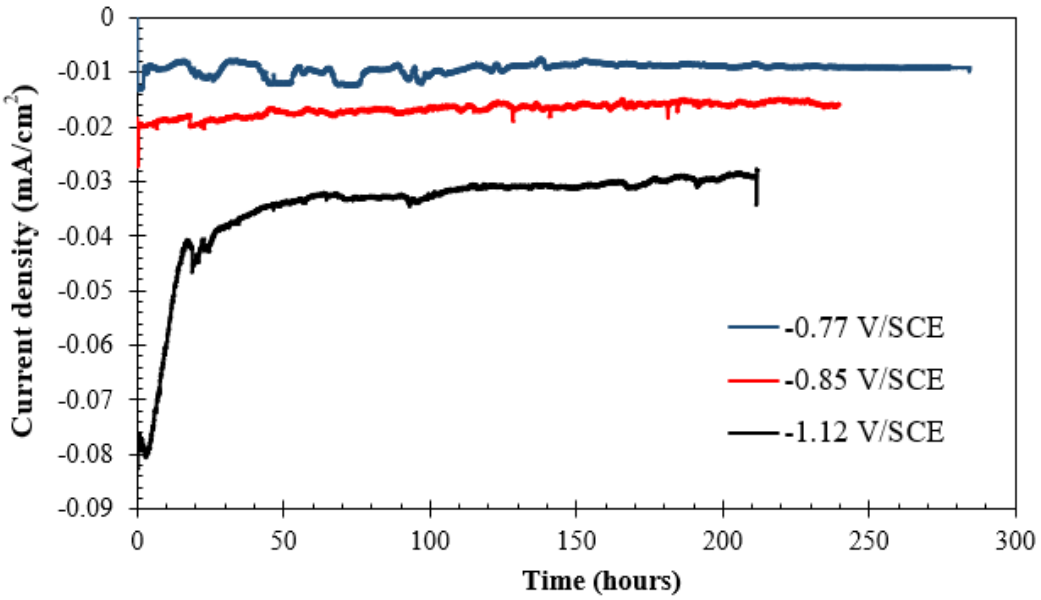

Figure 3.32. Current density vs. time behavior of carbon steel 1018 SSR specimens in NS4 solutions under different applied potentials (−0.77, −0.85, and −1.12 V/SCE).

The SSR test samples after failure were examined by visual observation, evaluating the fracture mode and possible presence of secondary cracking around the necking region. The optical images in Figure 3.33 show a typical cup and cone fracture mode for most of the samples except the one at −1.12 V/SCE (Figure 3.33d), where necking was minimal. This mode of fracture in steel is often associated with low ductility. In contrast, the reduction in area was the highest for the OCP sample in NS4 solution (Figure 3.33a). Lastly, the surface close to the fracture did not show any secondary fissures in all samples.

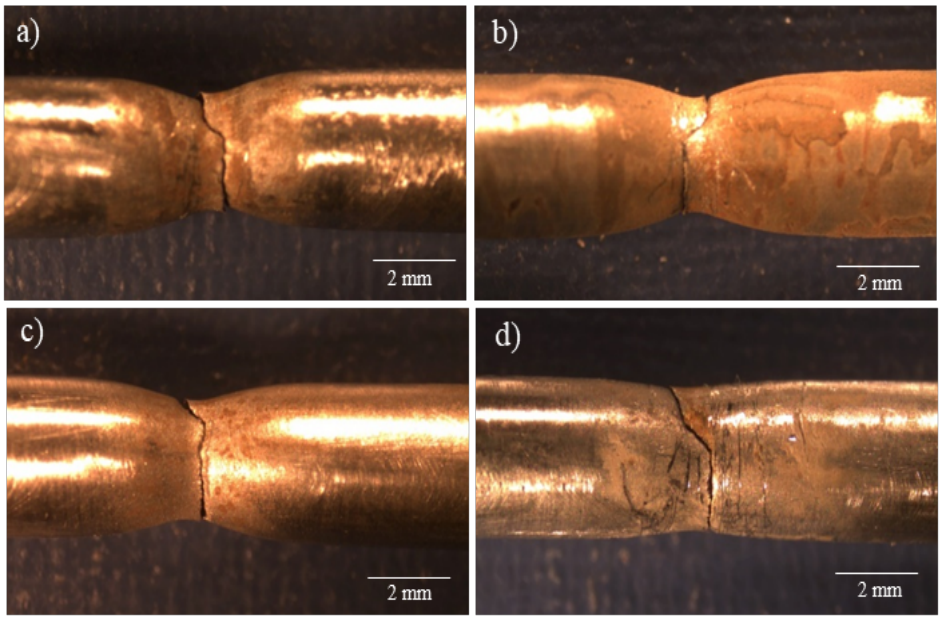

Figure 3.33. Optical microscopic images of fractured samples from SSR tests in the NS4 solutions, a) at OCP, b) at −0.77 V/SCE, c) at −0.85 V/SCE, and d) at −1.12 V/SCE.

The fracture morphology of the SSR test samples under applied cathodic potentials were examined by SEM and the results are shown in Figure 3.34. Changes in the fracture morphology were observed as the applied potential was increased in the cathodic direction. Although not shown, the sample in air showed mainly small dimples that correspond to a typical ductile fracture mode. The dimples were also present after the sample was exposed to NS4 solution at OCP (Figure 3.34b), −0.77 V/SCE (Figure 3.34d) and −0.85 V/SCE (Figure 3.34f), however the amount was smaller. In contrast, the fracture morphology of the sample under cathodic potential of −1.12 V/SCE showed mainly cleavage planes without cavities or dimples (Figure 3.34). It indicated brittle fracture behavior that is consistent with the least elongation and failure time obtained in the stress-strain curve (Figure 3.31), representing the highest SCC susceptibility.

Table 3.6 summarizes the typically reported mechanical properties for carbon steel 1018, including the yield strength (YS), ultimate tensile strength (UTS), Young's Modulus (E), rupture stress, elongation and failure time obtained from the experimental SSRT curves under each condition. From the results, the decrease in failure time and the reduction in the ductility (elongation) at lower cathodic potentials are clearly observed. A minimum elongation and highest rupture stress were found for the sample with −1.12 V/SCE. In addition, this sample showed high yield stress and ultimate tensile stress similar to the sample in air. It is hypothesized that this is due to a strengthening mechanism caused by the hydrogen atoms, that block the movement of dislocations and thus increase the strength. [62]

*Table **Error! No text of specified style in document.**.6. Summary of the mechanical properties of the carbon steel 1018 samples.*

Environment and applied potential	YS (MPa)	UTS (MPa)	E (MPa)	Rupture stress (MPa)	Elongation (mm)	Failure time (hours)
Air	650.9	716.4	46860	475	2.35	275.5
NS4 at OCP	626.2	719.2	59812	497	2.05	260.9
NS4 at −0.77 V/SCE	628.2	696.7	64632	498	1.85	258.7
NS4 at −0.85 V/SCE	638.3	695.9	58202	519	1.75	216.9
NS4 at −1.12 V/SCE	650.2	712.3	51735	637	1.30	186.8

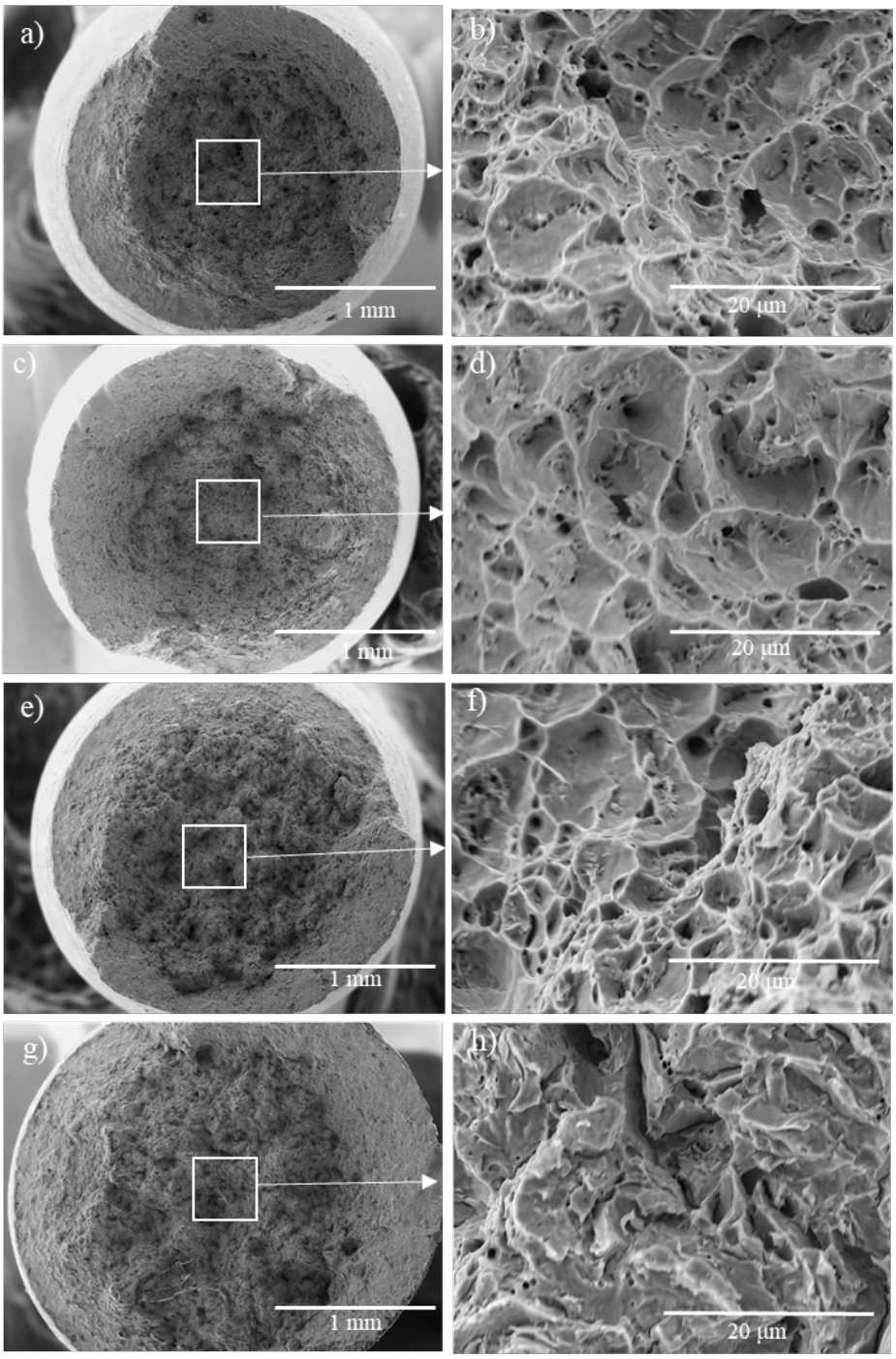

Figure 3.34. SEM images of fractured surfaces from SSRT samples in the NS4 solutions, (a-b) at OCP, (c-d) at −0.77 V/SCE, (e-f) at −0.85 V/SCE, and (g-h) at −1.12 V/SCE.

According to the NACE TM-198 [63] and ASTM G129 [51] standards, the SCC susceptibility can be evaluated using ratio of time to failure (RTTF), reduction area ratio (RAR) and percentage of plasticity loss (Iδ (%)). RTTF is the ratio of the time to failure determined for the material in the test environment (t_E) over the time to failure determined in the lab air environment (t_A)

$$\text{RTTF} = \frac{t_E}{t_A} \tag{3-1}$$

The plasticity loss, Iδ (%), is defined according to the following equation (3-2).

$$I_\delta\,(\%) = \left(\frac{\delta_A - \delta_E}{\delta_A}\right) \times 100 \tag{3-2}$$

where δ_A and δ_E, are the elongations of the specimens in air and in susceptible environment, respectively. The area reduction, (%)RA, is defined according to the following equation (3-3).

$$(\%)RA = \frac{({D_i}^2 - {D_f}^2)}{{D_i}^2} \times 100 \tag{3-3}$$

where D_f and D_i are the final and the initial diameters of the tensile specimen, respectively. RAR is calculated by relating the area reduction after fracture for the specimen in each environmental condition (RA_E) to that in lab air condition (RA_A), as defined in equation (3-4).

$$\text{RAR} = \frac{RA_E}{RA_A} \tag{3-4}$$

Table 3.7 lists the abovementioned parameters for each SSR test. The plasticity loss increased with more negative potential and was the greatest for the sample under −1.12 V/SCE, suggesting the highest susceptibility. According to the ASTM G129 standard [51], RTTF and RAR ratios in the range of 0.8 - 1.0 usually denote high resistance to environmentally assisted cracking (EAC), while lower values (< 0.8) generally indicate susceptibility to SCC. The results in Table 3-2 showed that carbon steel 1018 was susceptible to SCC in NS4 solution when the applied cathodic potential was below −0.85 V/SCE. The SCC susceptibility increased when the applied cathodic potential was more negative, which was clearly observed with the RAR values.

*Table **Error! No text of specified style in document.**.7. Summary of key parameters for the SCC susceptibility of carbon steel 1018 in NS4 solution with applied cathodic potentials[*].*

Environment	RTTF	I_δ (%)	(%)RA	RAR
Air	-	-	52.60	-
NS4 at OCP	0.94	13.86	48.90	0.93
NS4 at −0.77 V/SCE	0.94	19.11	47.95	0.91
NS4 at −0.85 V/SCE	0.79	26.40	35.73	0.68
NS4 at −1.12 V/SCE	0.68	55.30	18.02	0.34

[*]Highlight in yellow indicates possible susceptibility to SCC (< 0.8).

3.2.2 Effect of AC Voltages on SCC Behavior Under Cathodic Potentials

After studying the effect of applied cathodic potentials on the SCC behavior of carbon steel 1018 in NS4 solution, SSR tests were carried out to investigate the effect of AC voltages with simultaneous CP potentials applied to the tensile specimens. Three different magnitude of AC potentials were studied, 1, 2 and 3 V rms (root mean square) at two different cathodic potentials (−0.77 V/SCE and −1.12 V/SCE).

Figure 3.35 shows the effect of the AC voltages (0, 1, and 2 V rms) on the ductility and mechanical properties of carbon steel 1018 specimens in NS4 solution at the cathodic potential of −0.77 V/SCE. The elastic portion of the curves is almost overlapped for all the tests. It is interesting to note that both AC curves had higher UTS values than the curve with only CP of −0.77 V/SCE. However, the application of higher AC voltage showed a more brittle behavior. The AC voltage of 2 V rms significantly reduced the ductility, suggesting increased SCC susceptibility of the steel. This is possibly due to a greater entry of hydrogen into the steel, promoted by the cathodic half-cycles of the AC superimposition.

Contrary to this behavior, the sample with 1 V rms AC showed longer elongation, longer time to failure and less susceptibility compared to that with only CP of −0.77 V/SCE. This result is surprising as it suggests that the superimposition of 1 V rms AC at the cathodic potential of −0.77 V/SCE may have a beneficial effect for carbon steel 1018 in NS4 solution.

Figure 3.36 shows the effect of the AC voltages (0, 1, and 3 V rms) on the ductility and mechanical properties of carbon steel API X65 specimens in NS4 solution at the cathodic potential of −1.12 V/SCE. The stress-strain curve in lab air showed the highest ductility and was added as baseline. The pipeline steel API X65 shows better ductility and toughness in comparison to the 1018 steel in lab air (inert) environment, possibly due to its alloying elements.

It is shown in Figure 3.36 that the ductility was significantly reduced when a cathodic potential of −1.12 V/SCE was applied to the steel, probably due to an increased rate of HER. The yield stress for the sample with cathodic potential only was lower than the other conditions, which suggests an early start of plastic deformation. A reduction of the elongation was observed when the AC voltage was superimposed on the sample as compared to the result in lab air. The sample with 1 V rms AC voltage showed an elongation and stresses similar to, but slightly higher than the one with CP potential only. More surprisingly, a higher AC voltage (3 V rms) superimposed on the sample produced an increased ductility compared to that with CP potential only. This beneficial effect of AC interference has been found by other authors and attributed to the hydrogen-induced plasticity (HIP) effect.[64,65] It is believed that HIP can decrease the stress intensity at the crack tip and decrease the SCC risk by releasing the stress concentration which produces a more deformed zone.

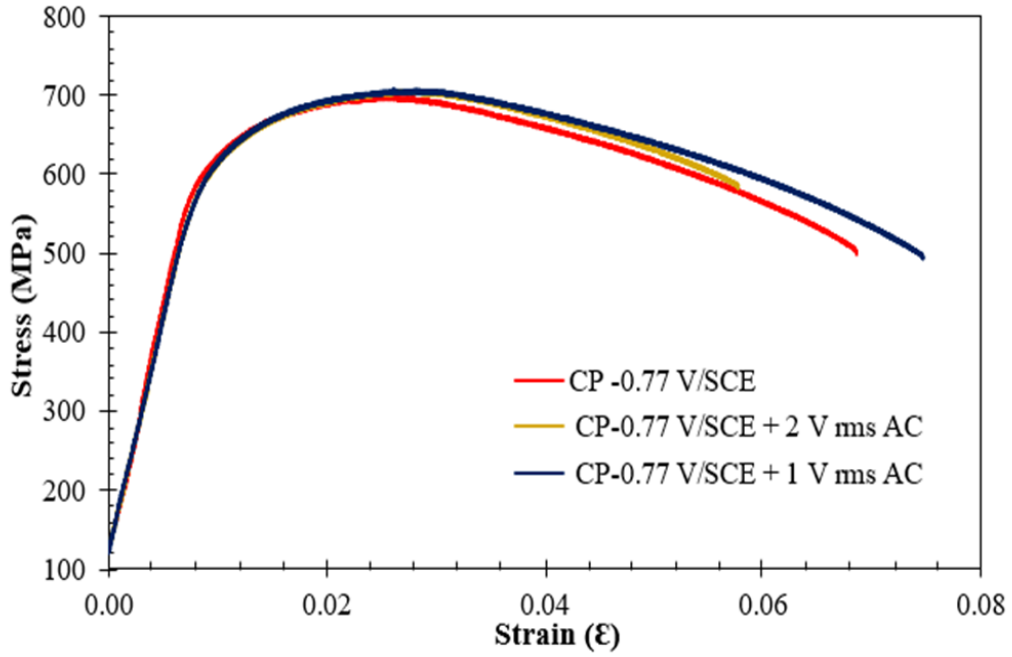

Figure 3.35. Comparison of stress-strain curves of carbon steel 1018 under different AC voltages (0, 1, and 2 V rms) at a cathodic potential of −0.77 V/SCE. Strain rate was 1×10^{-7} *in/s.*

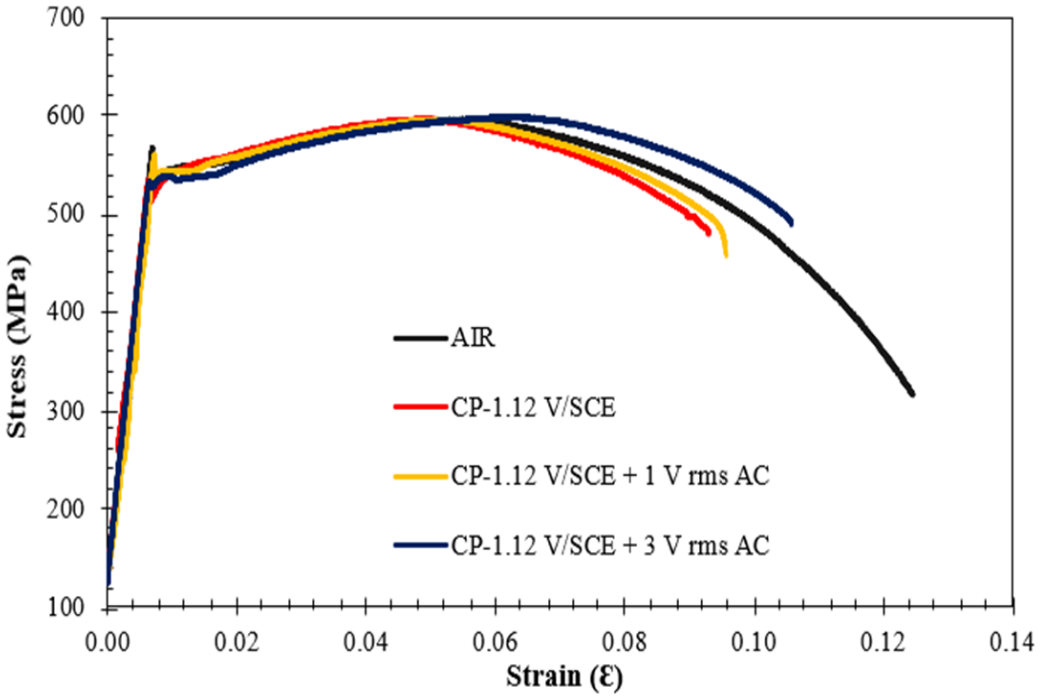

Figure 3.36. Comparison stress-strain curves of carbon steel API X65 in NS4 solution under different AC voltages (0, 1, and 3 Vrms) at the CP potential of −1.12 V/SCE. Strain rate was 1×10^{-7} *in/s.*

A comparison between Figure 3.35 and Figure 3.36 suggests that the SCC susceptibility of carbon steel depends on both cathodic potentials and AC voltages. At the application of 1 V rms AC, the susceptibility is slightly decreased compared to the case with cathodic potential only, and independent of the magnitude of the cathodic potentials. At the application of higher AC, the SCC susceptibility is significantly increased at −0.77 V/SCE with 2 V rms AC, but decreased at −1.12 V/SCE with 3 V rms AC.

Figure 3.37 shows the optical microscopic images of all the SSRT samples after fracture. The typical cup and cone fracture morphology was observed on the majority of the samples. Differences in the reduction in area were observed for different CP potentials with 1 V rms AC voltage (Figure 3.37 c vs. d). With the same AC voltage, lower area reduction was found at more negative cathodic potentials, suggesting higher susceptibility to EAC. In addition, the sample under 1 V rms AC and CP potential of −1.12 V/SCE showed the most typical brittle mode of fracture.

For the sample under the CP potential of −1.12 V/SCE and 3 V rms AC, it was interesting to find that small pits randomly distributed on the gauge section, along with secondary cracks around the necking region, as shown in Figure 3.38. In comparison, the other samples did not show cracks or pits on the necking region and the gauge section.

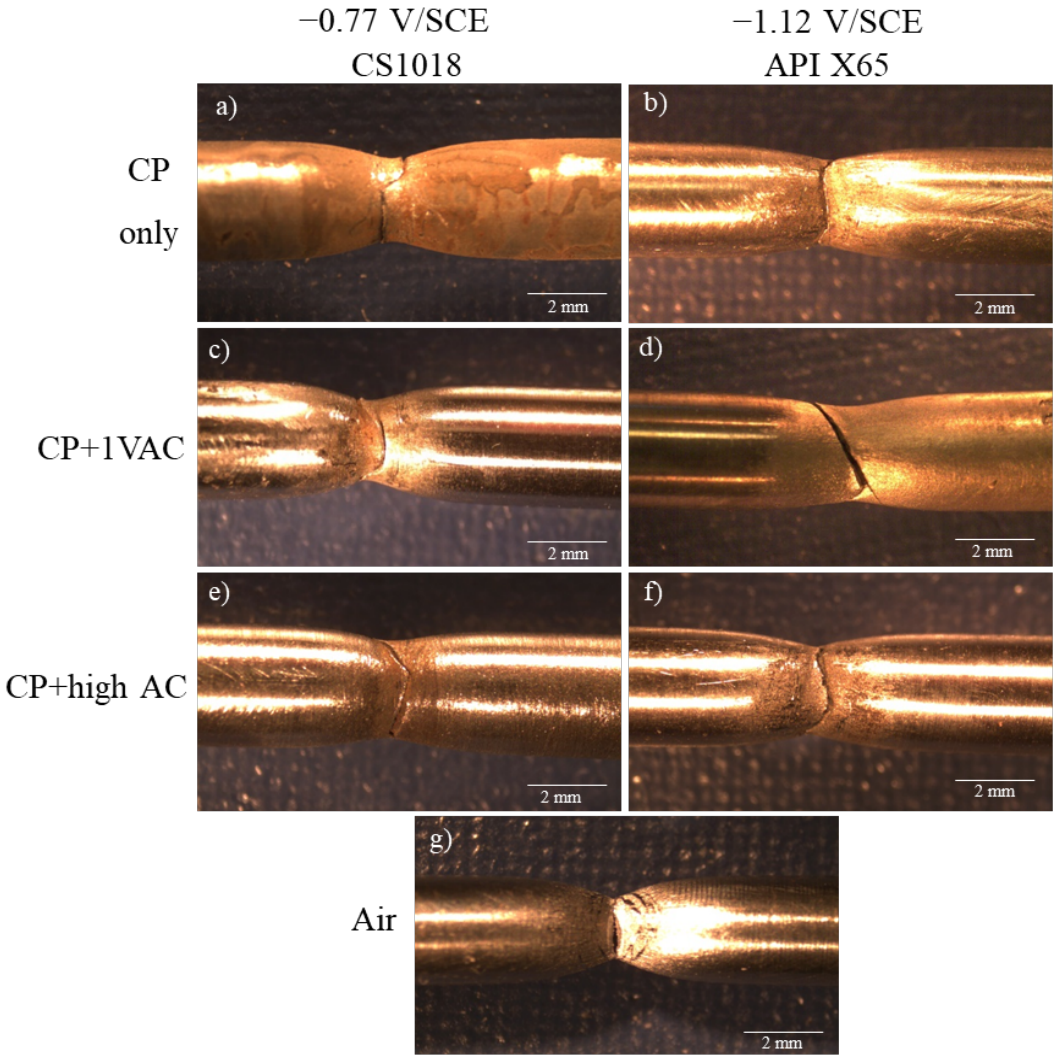

Figure 3.37. Optical images of fractured carbon steel specimens after SSR tests in NS4 solution, a) at −0.77 V/SCE, b) at −1.12 V/SCE, c) at −0.77 V/SCE + 1 V rms AC, d) at −1.12 V/SCE + 1 V rms AC, e) at −0.77 V/SCE + 2 V rms AC, f) at −1.12 V/SCE + 3 V rms AC, and g) baseline test in lab air environment. API X65 steel was used for (b, d, f, and g) and 1018 steel was used for (a, c, and e).

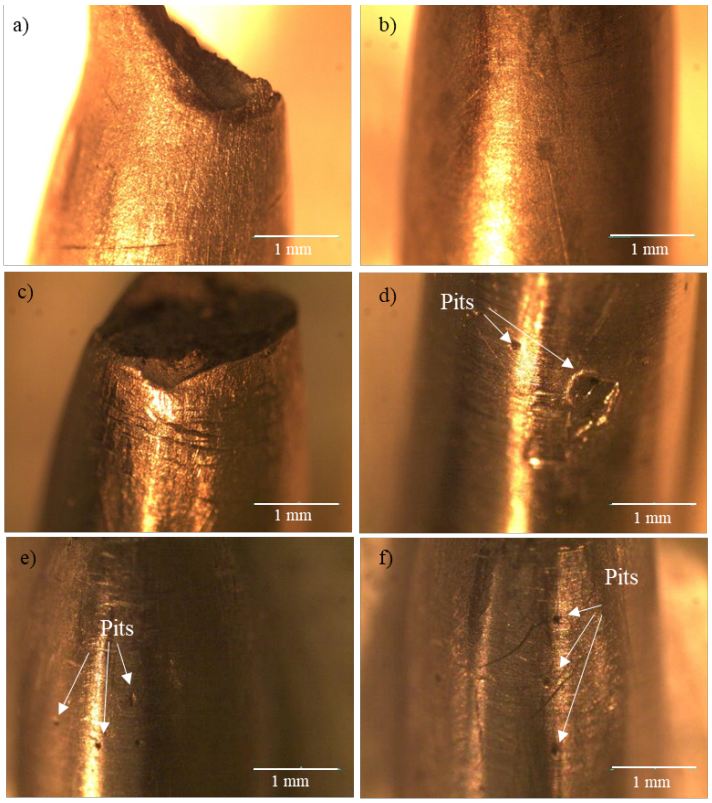

Figure 3.38. Comparison of fracture surface and gauge section of the API X65 samples after SSR tests in NS4 solution at the CP potential of −1.12 V/SCE, with (a-b) 1 V rms AC and (c-f) 3 V rms AC. Pits were found at 3 V rms AC (d-f).

For the API X65 steel exposed to the CP potential of −1.12 V/SCE and 1 V rms AC, the fracture surface was examined by SEM and the corrosion products formed were analyzed by EDS. The result is shown in Figure 3.39 and Table 3.8. Elements such as Fe, O, Ca, and Mg were identified in the corrosion products on the fracture surface. These elements can form components such as $FeCO_3$, Fe_2O_3, Fe_3O_4, and $Fe(OH)_2$, that have been reported as corrosion products under AC interference.[66] In addition, environmental effect was observed by the identification of Mg, Ca and Na on the metal surface.

Figure 3.40 shows the fracture morphology of the carbon steel 1018 SSRT samples subject the cathodic potential of −0.77 V/SCE with different levels of AC influence. The fractographs without AC application showed mainly dimples characteristic of ductile fracture. More distribution of microvoids was localized in the center of the specimen (Figure 3.40 a and b).

Under the AC interference, change in the fracture morphology was evidenced by more brittle behavior at higher AC voltages. When lower AC voltage was applied to the steel, insignificant difference was observed in the morphology (Figure 3.40 c and d). The decrease in the number of voids and the appearance of quasi-cleavage zones were found at higher AC voltage, showing brittle behavior (Figure 3.40 e and f).

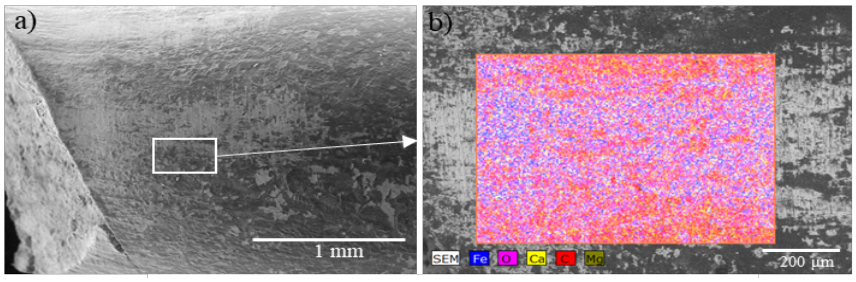

Figure 3.39. (a) SEM image of the fracture surface subject to EDS analysis, (b) selected area for EDS analysis.

Table 3.8. Quantitative EDS analysis of the surface in the Figure 3.39

Element	Weight %	Atomic %
Fe	48.72	21.50
O	23.46	36.13
C	14.61	29.98
Mg	10.22	10.36
Mn	1.19	0.54
Ca	0.94	0.58
Na	0.86	0.92

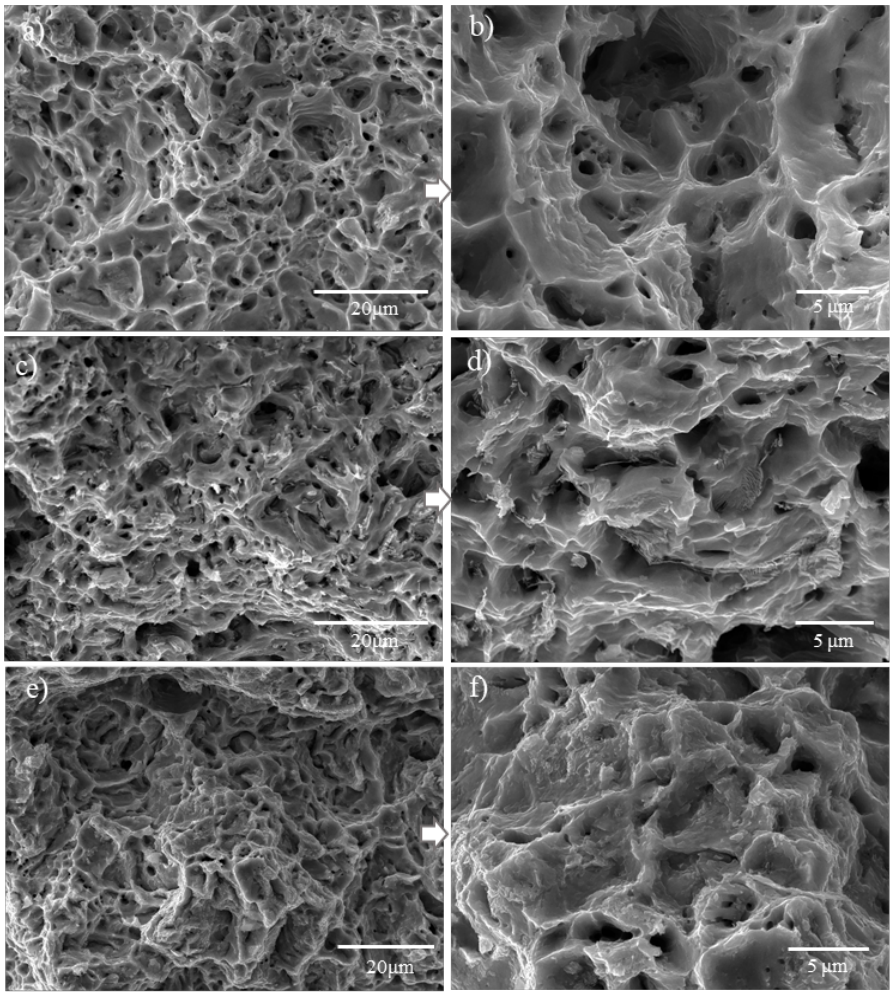

Figure 3.40. *Fracture morphology of the carbon steel 1018 SSRT samples in NS4 solution, (a, b) at −0.77 V/SCE, (c, d) at −0.77 V/SCE + 1 V rms AC, and (e, f) at −0.77 V/SCE + 2 V rms AC.*

Figure 3.41 shows the SEM images of the API X65 steel fracture surface under the most negative CP potential (i.e., −1.12 V/SCE) and with different AC voltages. The sample tested in lab air shows numerous dimples (Figure 3.41 b), possibly due to microvoid coalescence according to the ductile fracture mechanism. In contrast, when the CP potential and/or AC voltage were applied, the dimples disappeared, and the morphology changed to cleavage planes, clearly indicating brittle fracture. It has been reported that the AC fluctuations on the steel can increase the hydrogen evolution on the surface and produce the effect of hydrogen embrittlement.[38] The characteristics of brittle fracture were noted in all the samples at the CP potential of −1.12 V/SCE with different AC voltages (Figure 3.41 d, f and h).

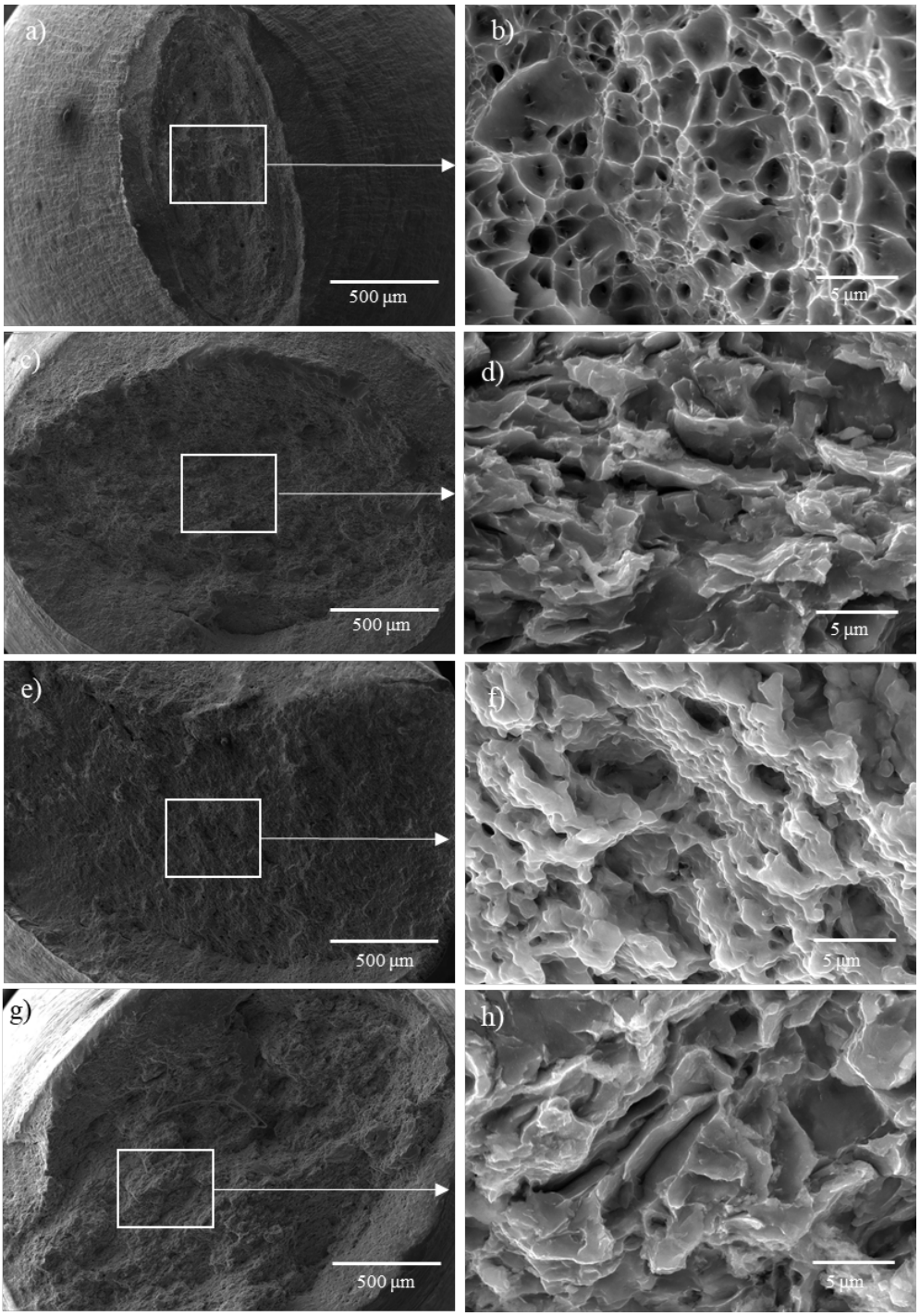

Figure 3.41. *Fracture morphology of the carbon steel API X65 SSRT samples, (a, b) in lab air, (c, d) at −1.12 V/SCE, (e, f) at −1.12 V/SCE + 1 V rms AC, and (g, h) at −1.12 V/SCE + 3 V rms AC. Tests were performed in NS4 solution when DC and AC potentials were applied.*

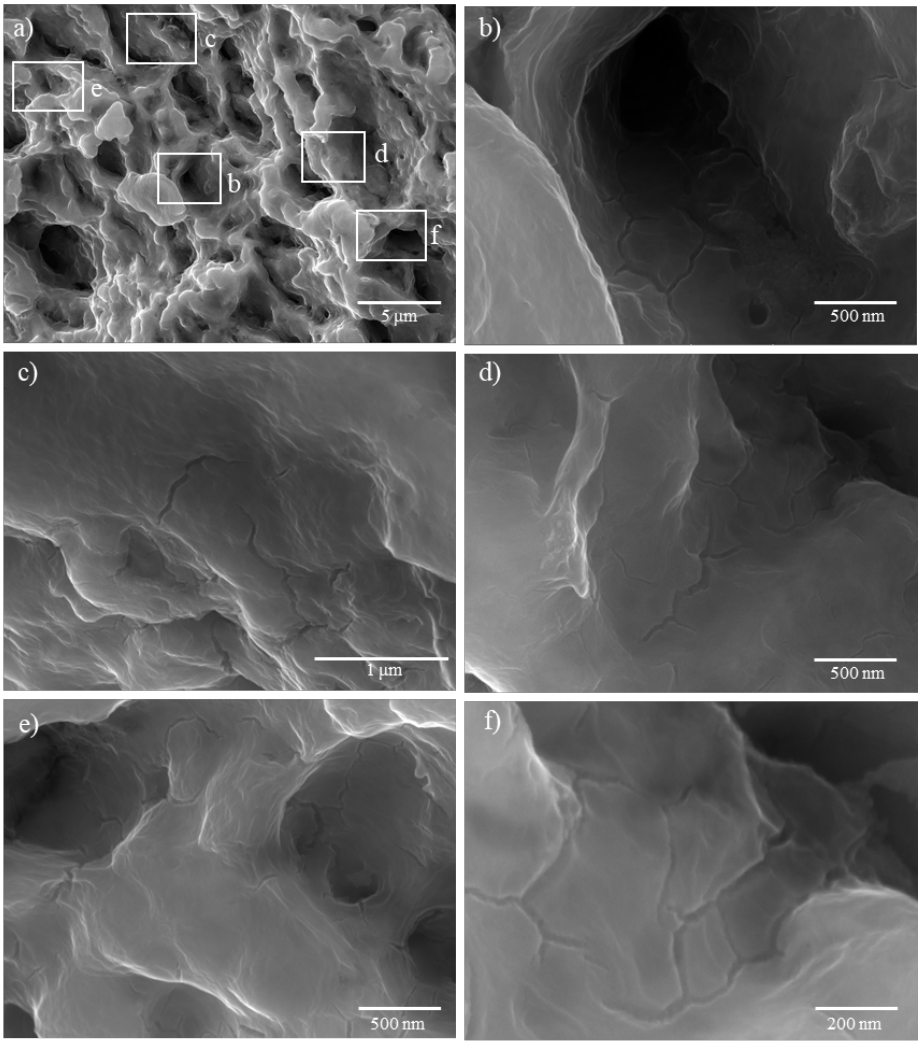

Figure 3.42. Fracture morphology of microcracks from the API X65 SSRT sample tested at the CP potential of −1.12 V/SCE and 1 V rms AC. Microcracks are clearly seen at high resolution (b-f).

Comparison of mechanical properties

It is interesting to note that the sample with 1 V rms AC was the only one where microcracks were observed at higher magnification, as shown in Figure 3.42. The cracking found inside the fracture surface indicates the effect of AC interference on the SCC susceptibility of the steel under this condition. Short and sharp cracks with little branching appeared in the morphology, characteristic of intergranular fracture.

Table 3.9 summarizes the mechanical parameters of the carbon steel samples obtained from the stress-strain curves (Figure 3.35 and Figure 3.36). Higher values of yield stress and ultimate tensile stress were obtained for the samples under the AC interference compared to those with CP potential only. Similar results have been found by other authors.[67] A significant reduction in the elongation was observed at the cathodic potential of −1.12 V/SCE with and without AC voltages, compared to the baseline result in air. Rupture stress was noticeably higher at the highest AC voltage under both cathodic potentials.

Table 3.9. Summary of the mechanical properties of the carbon steel samples

Materials	Environment* and DC/AC potentials	YS (MPa)	UTS (MPa)	Rupture stress (MPa)	Elongation (mm)	Failure time (hours)
Carbon steel 1018	Air	651	716.4	475	2.35	275.5
	−0.77 V/SCE	628	696.7	498	1.85	258.7
	−0.77 V/SCE +1 V rms	640	707.4	493.1	2.02	269.7
	−0.77 V/SCE +2 V rms	632	704.3	583.1	1.56	223.2
Carbon steel API X65	Air	533	594.9	315	3.45	397.0
	−1.12 V/SCE	512	596.0	479.3	2.41	313.0
	−1.12 V/SCE +1 V rms	538	595.1	457.7	2.47	313.3
	−1.12 V/SCE +3 V rms	527	598.1	489.1	2.74	343.4

* *NS4 solution if not specified otherwise.*

The SCC susceptibility based on the SSRT results was evaluated by the key parameters listed in Table 3.10 For the CP potential of −0.77 V/SCE, the plasticity loss, I_δ (%), was greater for the 1018 steel sample with 2 V rms AC. For the cathodic potential of −1.12 V/SCE with different AC voltages, the plasticity loss did not show a noticeable difference, but a slight decrease was observed with 3 V rms AC. According to the parameters of RAR and RTTF, the high susceptibility to environmental cracking was obtained for the samples at the cathodic potential of −1.12 V/SCE, with and without AC voltages. It is concluded that the effect of AC interference on the SCC susceptibility of carbon steels in NS4 solution depends on the CP potential applied. Lalvani et al.[18] suggested that under the AC influence, the electrochemical corrosion processes could either increase or decrease, depending on the CP potential applied to the steel.

Table 3.10. Summary of the key parameters for the SCC susceptibility of carbon steel in NS4 solution[*].

Material	Environment and DC/AC potentials	RTTF	I_δ (%)	(%)RA	RAR
Carbon steel 1018	Air	-	-	52.60	-
	NS4, −0.77 V/SCE	0.94	19.11	47.95	0.91
	NS4, −0.77 V/SCE +1 V rms	0.98	15.96	39.94	0.76
	NS4, −0.77 V/SCE +2 V rms	0.81	29.13	34.39	0.65
Carbon steel API X65	Air	-	-	73.02	-
	NS4, −1.12 V/SCE	0.79	29.50	41.79	0.57
	NS4, −1.12 V/SCE +1 V rms	0.80	29.94	40.99	0.56
	NS4, −1.12 V/SCE +3 V rms	0.86	26.37	39.01	0.53

[*]Highlight in yellow indicates possible susceptibility to SCC (< 0.8).

3.2.3 The Effect of AC Current and Potential

Changes in the current registered with the AC application confirm that AC interference can change the electrochemical activity of the surface. Figure 3.43 shows the current densities registered at the CP potential of −0.77 V/SCE with different AC voltages for carbon steel 1018 SSRT samples in NS4 solution. A positive shift in the current density was observed when the AC voltage was applied to the sample. The current magnitude increased as the AC voltage increased from 1 V to 2 V rms. Similar results were obtained by other authors.[68,65.]

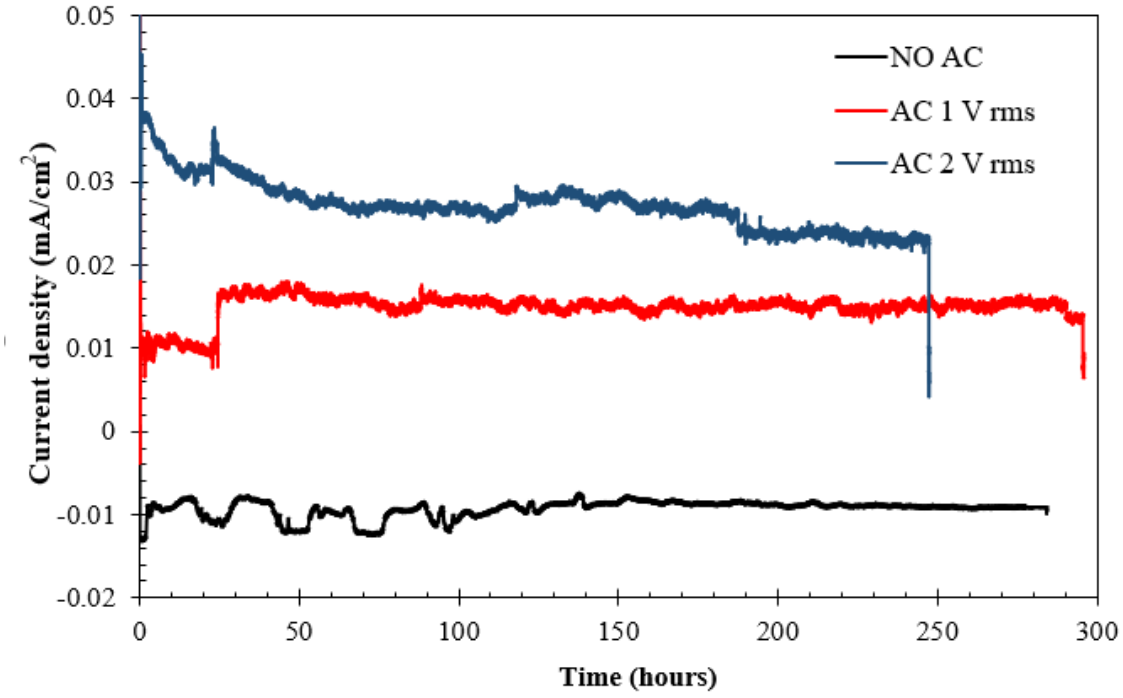

Figure 3.43. Current density vs. time curves at the CP potential of −0.77 V/SCE and different AC voltages (1 and 2 V rms) on carbon steel 1018 SSRT samples in NS4 solution.

As shown in Figure 3.44, at the CP potential of −1.12 V/SCE, a negative shift of the current was observed with the AC interference. Higher negative current densities were found with increasing AC voltages. The current density at 3 V rms AC remained relatively stable over the entire test, while the current density at 1 V rms AC kept decreasing over time. For the initial 200 h, the current densities were comparable between these two AC voltages, which were 2-3 times higher than that with cathodic potential only.

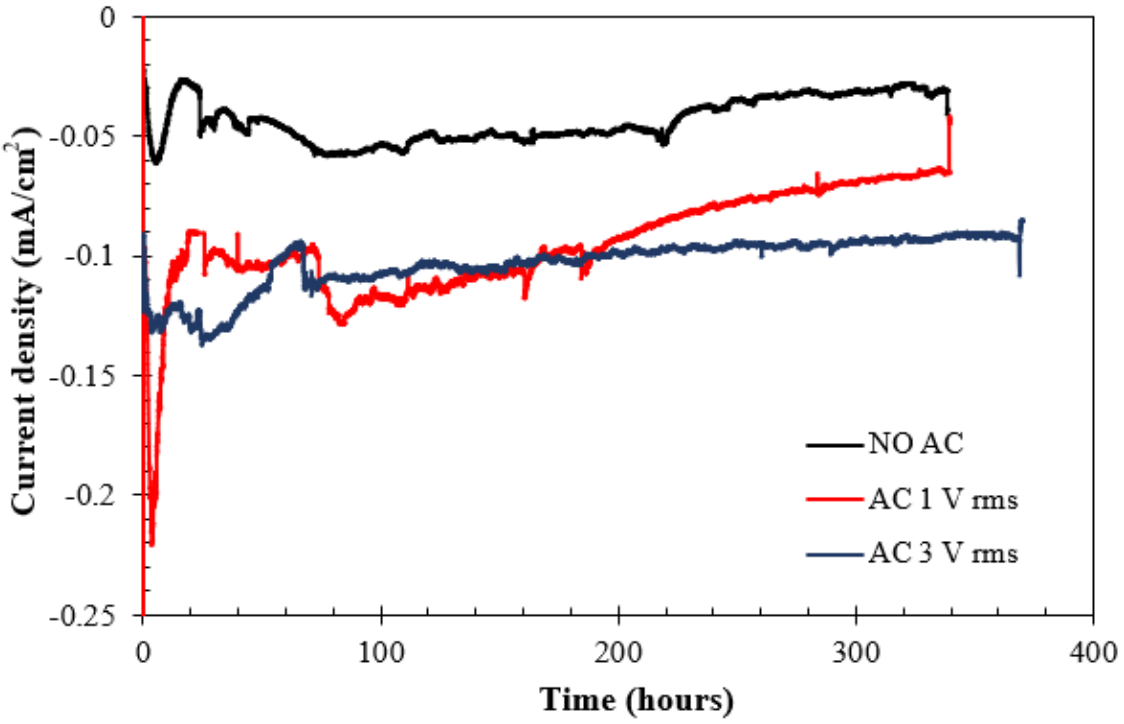

Figure 3.44. Current density vs. time curves at the CP potential of −1.12 V/SCE and different AC voltages (1 and 3 V rms) on carbon steel API X65 SSRT samples in NS4 solution.

A comparison of Figure 3.43 and Figure 3.44 suggests that AC interference can affect the polarity and magnitude of current, depending on the cathodic potential applied. The AC fluctuation at the steel surface affects both anodic and cathodic polarizations. The main anodic reaction is the iron dissolution generated during the positive half-cycle (reaction 3-5), and the cathodic reactions during the cathodic half-cycle, such as ORR at sufficiently positive potential (reaction 3-6) and HER at more negative potential (reaction 3-7).

$$Fe = Fe^{2+} + 2e^{-} \quad (3\text{-}5)$$

$$O_2 + 2H_2O + 4e^{-} = 4OH^{-} \quad (3\text{-}6)$$

$$2H_2O + 2e^{-} = H_2 + 2OH^{-} \quad (3\text{-}7)$$

The equilibrium potential for HER is calculated by

$$E_{H^+/H_2} = -0.241 - 0.059pH \quad \text{(V/SCE)} \quad (3\text{-}8)$$

since the pH of NS4 solution was measured to be 8.13, the hydrogen evolution potential for the system was calculated as −0.722 V/SCE. OCP of the steel was approximately −0.74 V/SCE. All the cathodic potentials studied were below the hydrogen equilibrium potential. Therefore, the evolution of hydrogen on the surface was thermodynamically possible. At lower cathodic potential, higher HER rate is expected, and it increases the probability of hydrogen diffusion into the steel. Researchers have demonstrated how hydrogen can

participate in the crack propagation and affect the SCC susceptibility.[69] This effect is consistent with the brittle morphology obtained in the samples under the CP potential of −1.12 V/SCE, with and without the AC voltages. Furthermore, metal dissolution under AC influence could be favored by the hydroxyl ions produced in the cathodic reactions (reactions 3-6 and 3-7) that alkalize the interface of the steel and increase in the soil conductivity.[70]

Since the electrons on the metal surface are generated by the anodic reaction and consumed by cathodic reaction, at the CP potential of −0.77 V/SCE, the AC superimposition enhances the anodic dissolution of the steel, with increasing anodic current density at higher AC voltages (Figure 3.43). This indicates that the production of electrons is greater than the consumption rate under this condition.[68] Moreover, there was a decrease in the current when the fracture of the sample occurred.

At the more negative cathodic potential of −1.12 V/SCE, AC interference enhanced the cathodic current density and accelerated the cathodic reactions. This favored the hydrogen evolution on the surface and would explain the brittle behavior and the increased SCC susceptibility under these conditions.

Figure 3.45 shows an example of the sinusoidal wave of the AC voltages and currents recorded by the DAQ software under the CP potential of −1.12 V/SCE in NS4 solution. Higher voltage and current oscillations were registered for the sample with 3 V rms AC. Some high peaks were observed in the current fluctuations. This type of interference signal could be related to an electromagnetic interference caused by the surrounding electrical equipment. The maximum positive values of the sine wave were 5 V and 0.6 V for the AC voltage of 3 Vrms and 1 V rms, respectively. The sinusoidal currents also showed a noticeable difference in magnitude.

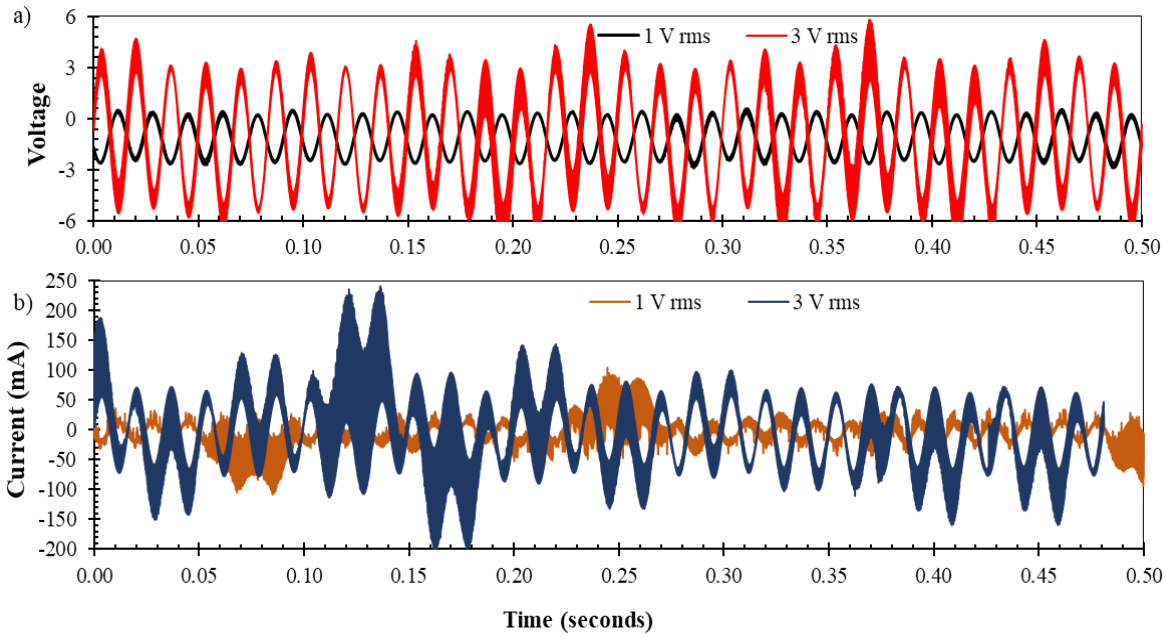

Figure 3.45. (a) Voltage-time and (b) current-time behavior measured by DAQ for API X65 SSRT samples with different AC voltages (1 and 3 V rms), under the CP potential of −1.12 V/SCE in NS4 solution.

In addition, Table 3.11 summarizes the range of AC current densities measured by the multimeter in each test. The results showed high AC current densities at high AC voltages. However, the variation of currents measured by the potentiostat under the AC voltages did not show significant difference. Researchers have suggested that not all the AC interference imposed on the steel contributes to corrosion. Most of the AC interference participates in charging and discharging process in the double layer and is considered non-faradaic current. Only the faradaic current component can affect the cathodic and anodic reactions, including the hydrogen production on the metal surface.[36]

Table 3.11. Range of AC current densities measured.

CP POTENTIAL (V/SCE)	AC VOLTAGES APPLIED (V rms)	AC CURRENTS MEASURED (A)	AC CURRENT DENSITIES (A/m^2)*
−0.77	1	0.024 - 0.015	22-14
	2	0.037 - 0.028	34-25
−1.12	1	0.025 - 0.012	23-11
	3	0.066 - 0.038	61-35

**with a surface area of approximately 11 cm^2.*

4. CONCLUSIONS

Laboratory and Field testing of corrosion rates on cathodically protected steel under the influence of AC was performed with long-term mass loss experiments. From these results we conclude:

• The effect of AC on the corrosion of steel depends on both the magnitude of i_{AC} and on the DC potential (CP level) of the steel. Greater i_{AC} leads to increased corrosion rates. At or below the commonly cited thresholds of AC density (30 A/m^2 and 100 A/m^2), cathodically protected samples show small or negligible increased corrosion rates.

• Greatly increased CRs due to AC have been demonstrated on unprotected steel emphasizing the effectiveness of and need for proper cathodic protection.

• Field testing validates the laboratory mass loss tests. Properly applied CP is very effective in mitigating the effect of AC on corrosion rates.

• Although i_{AC} and i_{DC} are tightly coupled, no indication of an overprotection condition in soil-simulant environments has been shown in this study. This phenomenon is possible if the local chemistry changes decrease the grounding resistance of the electrode so that i_{AC} increases beyond the protective ability of the CP.

The effect of AC voltages and CP potentials on the SCC behavior of the carbon steels (1018 and API X65) was investigated in NS4 solution by slow strain rate test with electrochemical measurements. Under the cathodic potential of −0.77V/SCE, a decrease in the ductility, failure time and area reduction were found at higher AC voltage. A lower susceptibility to cracking was found when 1 V rms AC voltage was applied, suggesting possible beneficial effect. At the CP potential of −1.12 V/SCE, higher cathodic current densities were obtained which enhanced the SCC susceptibility and generated brittle fracture. The effect of AC interference (up to 3 V rms) on the SCC susceptibility was minimal or slightly beneficial. It was found that changes in the electrochemical activity of the steel surface under AC interference depended on the applied CP potential.

1. Hoar, T.P., *J. Electrodepositors Tech. Soc.* 14 (1938): pp. 33–46.
2. Mears, R.B., and R.H. Brown., *Trans. Electrochem. Soc.* 74 (1938): pp. 519–531
3. Davy, H., *Philos. Mag. Ser. 1* 114 (1824): pp. 242–246.
4. Davy, H., *Philos. Mag. Ser. 1* 114 (1824): pp. 151–158.
5. SP0169, N.S., *Houston, TX NACE* (2002): pp. 12–17.
6. McCollum, B., and G.H. Ahlborn, *Am. Inst. Electr. Eng. Trans.* 35 (1916): pp. 301–345.
7. G. Heim ; T. Heim, H.H. ;W. S., *3 R Int.* 32 (1993): p. 246.
8. NACE International Task Group 327, "AC Corrosion State-of-the-Art: Corrosion Rate, Mechanism, and Mitigation Requirements" (2010).
9. Hosokawa, Y., F. Kajiyama, and Y. Nakamura, "New CP Criteria for Elimination of the Risks of AC Corrosion and Overprotection on Cathodically Protected Pipelines," in Corros. 2002. NACE Int. (NACE International, 2002).
10. SP0177, N.S., *Houston, TX NACE* (2007).
11. Stalder, F., "AC Corrosion On Cathodically Protected Pipelines: Guidelines for Risk Assessment and Mitigation Measures," in 5th Int. Congr. CeoCor (Belgium, 2001).
12. *Br. Stand. DD CEN/TS 152802006* (2006).
13. Lauvstad, G.Ø., and G. Paulsen, "CP System Design for Flowlines with Direct Electrical Heating," in Twent. Int. Offshore Polar Eng. Conf. Int. Soc. Offshore Polar Eng. (2010), p. 880653.
14. Boxall, J., T. Hughes, and E. May, "Direct Electrical Heating Of Liquid-Filled Hydrate Blockages," in 7th Int. Conf. Gas Hydrates, (Edinburgh, Scotland, United Kingdom, 2011).
15. Bosch, R.-W., and W.F. Bogaerts, *Corros. Sci.* 40 (1998): pp. 323–336.
16. Chin, D.-T., and S. Venkatesh, *J. Electrochem. Soc.* 126 (1979): p. 1908.
17. Gellings, P.J., *Electrochim. Acta* 7.1 (1962): pp. 19–24.
18. Lalvani, S.B., and X. Lin, *Corros. Sci.* 38 (1996): pp. 1709–1719.
19. Lalvani, S.B., and X.A. Lin, *Corros. Sci.* 36 (1994): pp. 1039–1046.
20. Nielsen, L. V, and P. Cohn, *Proc CeoCor* (2000): pp. 1–20.
21. NACE International. Standard Recommended Practice Mitigation of Alternating Current and Lightning Effects on Metallic Structures and Corrosion Control Systems. NACE Standard RPO177-2014, 2014(21021), 2014.
22. Task Group 327 and NACE International. Publication 35110: AC Corrosion State-of-the-Art : Corrosion Rate , Mechanism , and Mitigation Requirements. (24242):1-60, 2010.
23. R.A. Gummow. A/C Interference Guideline Final Report. Canadian Energy Pipeline Association, 2014.
24. International Organization for Standardization. ISO 18086:2015 Corrosion of metals and alloys. Determination of AC corrosion. Protection criteria. 2015.

25. CENELEC. EN:15280 (European standard) - Evaluation of AC corrosion likelihood of buried pipelines applicable to cathodically protected pipelines. Technical Specification, CEN - European Committee for Standardization, 2013.

26. R.A. Gummow, R.G. (Correng) Wakelin, and S.M (Correng) Segall. AC Corrosion - A New Challenge to Pipeline Integrity. In ASME - 1st International Pipeline Conference, volume 1, pages 1-18, 1996

27. Bertocci, U., *Corrosion* 35 (1979): pp. 211–215.

28. E. Ghanbari, M. Iannuzzi, R.S. Lillard, *Corrosion*, 72 (9),1196-1210, 2016.

29. Xiao, H., and S.B. Lalvani, *J. Electrochem. Soc.* 155 (2008): p. C69.

30. Zhang, R., P.R. Vairavanathan, and S.B. Lalvani, *Corros. Sci.* 50 (2008): pp. 1664–1671.

31. Qiu, W.W., M. Pagano, G. Zhang, and S.B. Lalvani, *Corros. Sci.* 37 (1995): pp. 97–110.

32. Nagy, Z., and D.A. Thomas, *J. Electrochem. Soc.* 133 (1986): pp. 2013–2017.

33. Zeng, K., and D. Zhang, *Prog. Energy Combust. Sci.* 36 (2010): pp. 307–326.

34. B.Y. Fang, A. Atrens, J.Q. Wang, E.H. Han, Z.Y. Zhu, and W. Ke, "Review of stress corrosion cracking of pipeline steels in 'low' and 'high' pH solutions," *J. Mater. Sci.*, vol. 8, pp. 127–132, 2003.

35. L. Xu, X. Su, Z. Yin, Y. Tang, and Y. F. Cheng, "Development of a real-time AC/DC data acquisition technique for studies of AC corrosion of pipelines," *Corros. Sci.*, vol. 61, pp. 215–223, 2012.

36. H. Wan, D. Song, Z. Liu, C. Du, Z. Zeng, X. Yang, X. Li "Effect of alternating current on stress corrosion cracking behavior and mechanism of X80 pipeline steel in near-neutral solution," *J. Nat. Gas Sci. Eng.*, vol. 38, pp. 458–465, 2017.

37. L. Zhiyong, C. Zhongyu, L. Xiaogang, D. Cuiwei, and X. Yunying, "Mechanistic aspect of stress corrosion cracking of X80 pipeline steel under non-stable cathodic polarization," *Electrochem. Commun.*, vol. 48, pp. 127–129, 2014.

38. M. Zhu, C. Du, X. Li, Z. Liu, S. Wang, J. Li, D. Zhang, "Effect of AC current density on stress corrosion cracking behavior of X80 pipeline steel in high pH carbonate/bicarbonate solution," *Electrochim. Acta*, vol. 117, pp. 351–359, 2014.

39. M. Zhu, C. Du, X. Li, Z. Liu, H. Li, and D. Zhang, "Effect of AC on stress corrosion cracking behavior and mechanism of X80 pipeline steel in carbonate/bicarbonate solution," *Corros. Sci.*, vol. 87, pp. 224–232, 2014.

40. M. Zhu, C. Du, X. Li, and Z. Liu, "Stress corrosion cracking of X80 pipeline steel under various alternating current frequencies in high-pH carbonate/bicarbonate solution," *Corrosion*, vol. 70, No. 12, pp. 1181–1188, 2014.

41. M. Zhu, G. Ou, H. Jin, C. Du, X. Li, and Z. Liu, "Study on the crack propagation behavior of X80 pipeline steel under AC application in high pH solution," *J. Mater. Eng. Perform.* (ASM International), vol. 24, pp. 2422–2425, 2015.

42. H. Wan, D. Song, Z. Liu, C. Du, Z. Zeng, and Z. Wang, "Effect of negative half-wave alternating current on stress corrosion cracking behavior and mechanism of X80 pipeline steel in near-neutral solution," *Constr. Build. Mater.,* vol. 154, pp. 580–589, 2017.

43. G. Schmitt, H.-G. Schoeneich, and G. Siegmund, “Influence of AC on hydrogen permeation at steel under cathodic polarization,” in *Paper* No. *5995. NACE Corrosion Conference*, pp. 1–14, *2015*.

44. Elmira Ghanbari. Corrosion behavior of buried pipeline in presence of AC stray current in controlled PhD thesis, The University of Akron, 2015.

45. ASTM International. Standard Practice for Preparing, Cleaning, and Evaluating Corrosion Test Specimens. In G1 - 03. 2017.

46. R N Parkins, W K Blanchard, and B S Delanty. Transgranular stress corrosion cracking of high-pressure pipelines in contact with solutions of near neutral pH. Corrosion, 50(5):394{408, 1994.

47. C. Ditzler, K. Schee, and H.C. Monger (eds). Soil Science Division Sta_. 2017. Soil survey manual. USDA Handbook 18., 2017.

48. Steel Grades, “Datasheet for steel UNS G10180 chemical information and mechanical properties of the structure steel,” http://www.steel-grades.com. 2016.

49. American Petroleum Institute.“Specification for line pipe, ANSI/API specification 5L,” Forty-Fourth Edition, API publishing services, Washington D.C. 2007.

50. R. N. Parkins, W. K. B. Jr, and B. S. Delanty, “Transgranular stress corrosion cracking of high-pressure pipelines in contact with solutions of near neutral pH 8,” Corrosion., vol. 50, No. 5, pp. 394–408, 1994.

51. ASTM International, “G129. Standard practice for slow strain rate testing to evaluate the susceptibility of metallic materials to environmentally assisted cracking,” 2000.

52. E. A. Noor and A. H. Al-Moubaraki, “Influence of Soil Moisture Content on the Corrosion Behavior of X60 Steel in Different Soils,” Arab. J. Sci. Eng., vol. 39, no. 7, pp. 5421–5435, Jul. 2014.

53. M. Aachib, M. Mbonimpa, and M. Aubertin, “Measurement and prediction of the oxygen diffusion coefficient in unsaturated media, with applications to soil covers,” Water. Air. Soil Pollut., vol. 156, no. 1–4, pp. 163–193, 2004.

54. M. B. Valcarce and M. Vazquez, “Carbon steel passivity examined in alkaline solutions: The effect of chloride and nitrite ions,” Electrochim. Acta, vol. 53, no. 15, pp. 5007–5015, Jun. 2008.

55. K. Daub, X. Zhang, L. Wang, Z. Qin, J. J. Noël, and J. C. Wren, “Oxide growth and conversion on carbon steel as a function of temperature over 25 and 80 under ambient pressure,” Electrochim. Acta, vol. 56, no. 19, pp. 6661–6672, Jul. 2011.

56. NACE International, “Standard Practice Control of External Corrosion on Underground or Submerged Metallic Piping Systems,” 2013.

57. CENELEC, “EN:15280 (European standard) - Evaluation of A.C. corrosion likelihood of buried pipelines applicable to cathodically protected pipelines,” Tech. Specif. CEN - Eur. Comm. Stand., 2013.

58. E. Ghanbari and R. S. Lillard, “The Influence of $CaCO_3$ Scale Formation on AC Corrosion Rates of Pipeline Steel Under Cathodic Protection,” 2018.

59. F. Stalder, “Influence of soil composition on the spread resistance and of ac corrosion on cathodically protected coupons,” 5th Int. Congr. Brussels, Belgium CEOCOR, 2000.

60. R. N. Parkins, “Development of strain-rate testing and its implications,” Stress Corrosion Cracking – The Slow Strain-Rate Technique, ASTM STP 665, G. M. Ugiansky and J. H. Payer, Eds., ASTM International, pp. 5–25, 1979.

61. Michael Baker Jr, “Understanding stress corrosion cracking (SCC) in pipelines,” in Stress Corrosion Cracking Study TTO No.8. Final report, pp. 15–28, 2005.

62. J. Capelle, I. Dmytrakh, and G. Pluvinage, “Comparative assessment of electrochemical hydrogen absorption by pipeline steels with different strength,” Corros. Sci., vol. 52, No. 5, pp. 1554–1559, 2010.

63. NACE Standard TM0198-2011. “Slow strain rate test method for screening corrosion- resistant alloys for stress corrosion cracking in sour oilfield service,” NACE International, item No. 21232, 2011.

64. Z. Liu, X. Wang, C. Du, J. Li, and X. Li, “Effect of hydrogen-induced plasticity on the stress corrosion cracking of X70 pipeline steel in simulated soil environments,” Mater. Sci. Eng. A, vol. 658, pp. 348–354, 2016.

65. H. Wan, D. Song, Z. Liu, C. Du, Z. Zeng, and Z. Wang, “Effect of negative halfwave alternating current on stress corrosion cracking behavior and mechanism of X80 pipeline steel in near-neutral solution,” Constr. Build. Mater., vol. 154, pp. 580–589, 2017.

66. Y. Guo, T. Meng, D. Wang, H. Tan, and R. He, “Experimental research on the corrosion of X series pipeline steels under alternating current interference,” Eng.Fail. Anal., vol. 78, pp. 87–98, 2017.

67. Q. Liu, W. Wu, Y. Pan, Z. Liu, X. Zhou, and X. Li, “Electrochemical mechanism of stress corrosion cracking of API X70 pipeline steel under different AC frequencies,”Constr. Build. Mater., vol. 171, pp. 622–633, 2018.

68. L. Xu, X. Su, and Y. Cheng, “Effect of alternating current on cathodic protection on pipelines,” Corros. Sci., vol. 66, pp. 263–268, 2013.

69. W. W. Gerberich, T. Livne, X. F. Chen, and M. Kaczorowski, “Crack growth from internal hydrogen-temperature and microstructure effects in 4340 steel,” Metall.Trans. A, vol. 19, no. 5, pp. 1319–1334, 1988.

70. A. Fu and Y.F. Cheng, “Effect of alternating current on corrosion and effectiveness of cathodic protection of pipelines,” Can. Metall. Q., vol. 51, No. 1, pp. 81–90, 2012.